POLITECNICO DI TORINO

Collegio di Ingegneria Chimica e dei Materiali

Master of Science Course
in Materials Engineering

Master of Science Thesis

Reduced Graphene Oxide for dendrites suppression in lithium metal anodes

Tutor
Andrea LAMBERTI
Supervisor
NA Young-Hye

Candidate
Matteo CAPRIOLI

March 2018

To Gianfranco,
Smiling master of curiosity and discovery

Abstract

The development of zero emission electric vehicles is strongly pushed by the depletion of fossil fuels and the increasing global warming. However, those vehicles need high power density rechargeable batteries, among which lithium-air and lithium-sulfur systems are emerging as promising technologies to improve power and useful range. The key factor for the excellent performances, several times higher than Li-ion batteries, is the use of lithium metal anode that provides encouraging theoretical performances, although technological problems still limits their use, for instance dendrites growth, that can cause a short circuit in the cell.

In order to overcome some of those issues, in this work we used reduced graphene oxide (RGO) both as protective layer and host medium for the lithium metal anode, taking advantage of the suitable properties of this material, such as lithiophilicity and mechanical strength. Multiple goals were prefixed: to compare the RGO aerogels obtained from two different synthesis techniques with a green reducing agent; to design the process and to realize a free-standing membrane; at last to evaluate the electrochemical performances. This study has been developed in collaboration between Politecnico of Torino and IBM – Almaden Research Center.

Aerogels were prepared with a self-assembly method for obtaining a 3D structure, achieved with a facile one-pot hydrothermal treatment (HT-RGO) of a graphene oxide suspension; the reduction was performed thanks to the hydrothermal conditions and the addition of ascorbic acid in the system. Graphene oxide has been also reduced using microwave-assisted hydrothermal process (MW-RGO), which decreases the time required to complete the reaction and allows to follow *in-situ* the aggregation of GO flakes during the formation of the 3D network thanks to the use of a glass vessel. The reduction reaction has been investigated by means of FTIR spectroscopy that shows the removal of hydroxyl groups on the surface. This result is confirmed by XPS and Raman spectra, which exhibit an increase in C/O ratio and D/G peaks ratio respectively, with slightly higher ratios for HT-RGO, so the microwaves allow to complete the reaction in less time but with a lower reduction. FESEM images illustrate an irregular and coarse morphology for MW-RGO, different from the 3D network obtained from hydrothermal, most likely due to the speed of heating caused by the microwave irradiation, that causes a chaotic motion of the flakes, assumption supported by the specific surface value, that results half of HT-RGO.

The membrane was prepared grinding the aerogel with an addition of PTFE and then pressing the mix in a die. The electrochemical properties were tested into symmetric coin cells assembled with the protective layer placed on top of melted lithium; the characterization evidences that the presence of the membrane extended the lifetime of the metal anode, even though induced a wider voltage gap due to a higher internal resistance, and an instability of the cycle. These results encourage further studies to deeply understand the working mechanisms of the RGO membrane and improve the proposed solution.

Acknowledgments

I would first like to deeply thank my thesis advisor Dr. Andrea Lamberti for believing in my skills, allowing me to work again in his team and then giving me the unmissable opportunity to continue and develop my project in collaboration with IBM. I would also like to acknowledge Dr. Paola Rivolo and Dr. Mara Serrapede for their explanations and advises during the work and the valuable comments on this thesis, for which I am very grateful.

I would like to express my great appreciation to Dr. Luisa Bozano, who made possible for me to be part of IBM for five fantastic months thanks to her commitment, and especially to my supervisor Dr. Na Young-Hye, whose office door was always open whenever I ran into trouble or I had questions about my work My thanks are extended to actual and past members of the "Battery500" group, especially Dr. Sogol Teschler, Dr. Phillip Medina IV, Dr. Kim Jangwoo and Dr. Khanh Nguyen, for strongly supporting, advising and encouraging me throughout the whole experience. The assistance provided by Dr. Andy Tek with TGA and XPS characterization techniques provided me very valuable results.

A special thank goes to my friend Lorenzo Vigna, who shared with me this crazy american adventure, for the mutual support and the fun we had together.

I wish to gratefully thank my italian family, for their unfailing support and continuous encouragement throughout my study and for believing in me during this experience, and Esther Quement together with her big californian family, for welcoming us and making us feel part of the family. This accomplishment would not have been possible without both families.

Finally, but not less important, I wish to thank Marina, for her constant support and inexhaustible patience. Thank You.

Sommario

Introduzione

Il consumo dei combustibili fossili e la necessità di ridurre il riscaldamento globale stanno alimentando la domanda di dispositivi per l'immagazzinamento di energia più efficienti e meno impattanti da un punto di vista ambientale, i quali garantiscano sufficiente sicurezza ed affidabilità senza inficiarne l'efficacia. Le prestazioni delle batterie agli ioni di litio hanno subito una impennata, specialmente negli ultimi anni, soddisfacendo sempre più le richieste di strumenti e dispositivi di piccole dimensioni, ma non sono sufficienti per garantire una adeguata alimentazione ai motori per autoveicoli elettrici o sufficiente densità energetica per dispositivi elettrici ad alto rendimento. Per impieghi ad alte prestazioni sono attualmente allo studio tecnologie innovative che aumentano le prestazioni senza ingrandire le dimensioni del dispositivo. Unione Europea e Stati Uniti hanno investito ingenti somme nella ricerca e sviluppo di batterie in grado di garantire una maggiore autonomia ai veicoli elettrici, e tra questi sistemi di nuova generazione, i più promettenti sono le batterie ricaricabili con anodo di litio metallico, come i sistemi litio-zolfo (Li-S) e litio-aria (Li-O_2) (fig. 1.1).

Lo zolfo, come elemento attivo del catodo della batteria, garantisce elevata densità energetica a basso costo ed impatto ambientale, grazie alle sue ridotte dimensioni, l'ampia abbondanza ed accessibilità. La corrente viene generata dalla reazione elettrochimica derivante dalla rottura del legame tra gli atomi di zolfo indotta dagli ioni di litio, che riducono progressivamente la lunghezza della catena solforosa a dei polisolfuri prodotti durante la fase di scarica. La solubilità dei polisolfuri provoca una riduzione delle prestazioni della batteria, che richiede un confinamento di questi nel catodo per garantire elevata reversibilità di reazione, ridotta anche dalla passivazione dell'anodo provocata dall'accumulo dai prodotti di scarica isolanti, che inoltre provocano una ampia variazione dimensionale del catodo. La maggior parte delle caratteristiche richieste ad un materiale catodico per questo tipo di batterie sono soddisfatte dai materiali carboniosi nanostrutturati, che garantiscono una buona affinità con lo zolfo elementare combinata ad una ottima conduttività, porosità e resilienza, ma devono essere funzionalizzati per renderli compatibili con i prodotti di scarica.

L'ossigeno come materiale attivo catodico garantisce ancora maggiori prestazioni rispetto allo zolfo perché, non avendo la necessità di essere immagazzinato all'interno del catodo, fa sì che l'energia specifica teorica del dispositivo sia determinata solo dal materiale anodico, risultando di un ordine di grandezza superiore rispetto a qualsiasi altro dispositivo. Le fasi di carica e scarica si basano sulle reazioni di riduzione ed evoluzione di ossigeno al catodo, con meccanismi e prodotti di reazioni differenti a seconda dell'utilizzo di un elettrolita a base acquosa o uno a base di solvente organico. La capacità pratica e reale della cella dipende dal quantitativo di prodotti di reazione effettivamente immagazzinati nel catodo, che aumenta all'aumentare dell'estensione superficiale interna del catodo ed è favorita da un materiale costituente l'elettrodo con porosità gerarchicamente ordinata, la quale favorisce una distribuzione maggiore e più omogenea dei prodotti di reazione e di eventuali catalizzatori della stessa. I materiali carboniosi nanostrutturati, oltre ad essere provvisti di una adeguata distribuzione di dimensione dei pori, garantiscono inoltre una ottima affinità con i solventi organici, massimizzando il contatto e quindi la capacità utile, sono dotati di una discreta attività catalitica per la riduzione elettrochimica dell'ossigeno, e sono facilmente dopabili o ibridizzabili con materiali catalizzatori per ridurre il voltaggio eccessivo.

Il fattore chiave delle eccellenti prestazioni di questi sistemi di nuova generazione è l'utilizzo di puro litio metallico come anodo (fig. 1.2), il quale, nonostante gli innegabili vantaggi apportati, è caratterizzato da importanti e gravi problemi di sicurezza e affidabilità che hanno spinto verso l'utilizzo di materiali di intercalazione del litio come elettrodi negativi nelle batterie agli ioni di litio, e che vanno risolti per permetterne l'impiego avvantaggiandosi degli enormi benefici introdotti. Lo scopo di questo lavoro di tesi è stato quello di trovare il modo di impiego più idoneo del grafene ossido ridotto (RGO) come materiale protettivo per l'anodo di litio metallico. Il primo obiettivo è stato quello di definire i parametri di processo per la reazione di riduzione idrotermale assistita dalle microonde in presenza di un agente riducente quale la vitamina C, e confrontare il materiale risultante da questo processo con quello prodotto con sintesi idrotermale convenzionale. Il secondo obiettivo era quello di ideare un processo produttivo per realizzare lo strato protettivo e trovare la procedura migliore per introdurlo nel sistema, per poi valutarne le performance elettrochimiche. Questo lavoro è stato svolto in cooperazione tra il dipartimento DISAT del Politecnico di Torino ed il gruppo "Battery500" di IBM presso l'Almaden Research Center, unendo le conoscenze possedute al Politecnico riguardo la sintesi idrotermale con la competenza di IBM riguardo dispositivi di immagazzinamento di energia.

Anodo di litio metallico

Il litio è l'elemento metallico più leggero ed elettropositivo (tab 2.1), è malleabile e può essere facilmente estruso in fogli sottili, i quali si ricoprono rapidamente di un sottile strato di ossido nativo. La ridotta densità, buona conduttività ed elevata equivalenza chimica e potenziale d'elettrodo lo rendono il materiale anodico ideale per batterie ad alte prestazioni tra i materiali metallici presi in considerazione per fabbricare elettrodi negativi metallici, come zinco e sodio, perché garantisce la migliore densità gravimetrica di energia teorica e i più alti voltaggi operativi (tab 2.2). Le attuali batterie Li-Ion sono costituite da due elettrodi che incorporano il litio nella loro struttura cristallina mediante un processo di intercalazione, una reazione durante la quale gli ioni sono inseriti e rimossi reversibilmente nella struttura, comportando alterazioni significative del materiale ospitante, specialmente una variazione volumica che induce una riduzione nella conducibilità elettrica dell'intercalante e uno stress meccanico che può portare a rottura dopo ciclaggio della batteria. L'impiego di del litio metallico comporta una maggiore velocità di diffusione degli ioni Li^+, che non devono più diffondere allo stato solido all'interno del materiale intercalante ma vengono semplicemente disciolti nell'elettrolita durante la fase di scarica, mentre durante la fase di ricarica avviene una deposizione catodica sull'elettrodo. Tuttavia, il lito metallico è caratterizzato da una elevata reattività con molti gas normalmente contenuti nell'aria come ossigeno, acqua ed anidride carbonica, dando vita ad una reazione esotermica vigorosa con formazione di idrogeno che può incendiarsi, pertanto il suo maneggiamento deve essere effettuato in ambienti anidri, inerti e controllati. Il litio è inoltre molto reattivo con gli elettroliti a base organica, i quali degradano formando uno strato isolante sulla superficie dell'elettrodo insolubile nell'elettrodo, il quale inoltre incorpora altri sottoprodotti provenienti da specie differenti presenti nell'elettrolita, che separa la superficie metallica dal liquido, prevenendo ulteriori reazioni. Questo film è chiamato interfase solido/elettrolita (SEI), è un isolante per la conduzione elettronica, ed è caratterizzato da numerose difettosità cristalline come vacanze e bordi di grano che favoriscono la conduttività ionica (fig. 2.1). La sua composizione è eterogenea e varia lungo tutto il suo spessore, dipendendo strettamente dal tipo di elettrolita a contatto con la superficie metallica e dagli additivi e impurità presenti al suo interno. La formazione del SEI è impossibile da evitare, dipende fortemente da corrente e voltaggio nella cella e determina una perdita di capacità utile. Essendo uno strato prettamente ceramico, è caratterizzato da una fragilità intrinseca, che comporta una rottura a seguito delle inevitabili variazioni dimensionali dell'anodo metallico, la quale viene riparata da un processo di auto-rigenerazione. La deposizione del litio avviene al di sotto di questo strato in maniera disomogenea, formando una struttura fibrosa che può fratturarsi, causando una perdita di materiale dalla superficie, il quale viene elettrochimicamente inattivato e che si ammassa sull'anodo diminuendone la superficie utile. L'elettrodeposizione degli ioni di litio avviene preferenzialmente al di sotto dei punti del SEI a maggiore conduzione ionica, determinando la crescita incontrollata e direzionale di dendriti che possono causare un corto-circuito nella cella dopo aver forato il separatore (fig. 2.4), la cui velocità di ingrandimento dipende dalla corrente che attraversa il sistema. Questi problemi rendono impossibile una perfetta ciclabilità dell'anodo metallico, il quale richiede un eccesso di materiale al suo interno per assicurare performance accettabili e discreto tempo di vita utile, compensando l'inefficienza del processo di dissoluzione e deposizione.

Ad oggi, lo stato dell'arte nella risoluzione dei problemi connessi con l'anodo metallico ha intrapreso diverse direzioni, modificando diversi aspetti del sistema. Un primo approccio, affine alle batterie Li-Ion, è quello di realizzare un elettrodo composito, il quale garantisce ottime prestazioni ma limita la geometria del sistema data la fragilità del materiale. La soppressione delle dendriti può essere ottenuta imponendo una pressione sull'anodo dall'esterno oppure depositando uno strato protettivo con un modulo elastico almeno doppio rispetto a quello del litio metallico. La stabilità può essere migliorata apportando delle modifiche all'elettrolita, per formare un SEI più compatto e stabile, in modo da ottenere una soppressione meccanica delle dendriti, introducendo sali di litio ed additivi per controllarne la morfologia. È inoltre possibile sopprimere elettrostaticamente la crescita delle dendriti, introducendo cationi positivi nell'elettrolita liquido che omogeneizzino il flusso ionico sulla superficie. Possono esser effettuate modifiche direttamente all'anodo, introducendo un film artificiale direttamente sulla superficie in modo tale che rimpiazzi il SEI nativo, che può essere chimicamente legato alla superficie metallica o semplicemente appoggiato sopra di essa. Questi film artificiali possono essere strati spessi oppure coating sottili i quali controllano il processo di deposizione del litio e sopprimendo meccanicamente le dendriti. Purtroppo, i SEI artificiali sono solitamente affetti da una ridotta conduttività ionica, per questo motivo sono stati esplorati gli elettroliti a stato solido, che permettono una elevata diffusione degli ioni e allo stesso momento una efficace protezione dell'elettrodo. Questi elettroliti allo stato solido possono essere polimeri, gel polimerici o materiali cristallini inorganici. IBM ha sviluppato una membrana composita spessa un unico strato di particelle, prodotta unendo delle particelle ceramiche litio-conduttive a base di tantalio con una matrice polimerica che garantisce isolamento ionico e che non copre le superfici superiori ed inferiori delle particelle stesse. Questa membrana agisce allo stesso momento sia da separatore che da elettrolita allo stato solido, e permette di unire la flessibilità della matrice con l'abilità di trasporto ionico e il modulo elastico del rinforzo, essendo in grado di sopprimere le dendriti, e contemporaneamente garantire una distribuzione della corrente ionica che fa accrescere le dendriti in direzione delle particelle, enormemente più rigide della matrice. Il processo di produzione è semplice e versatile, non richiede un pretrattamento delle particelle, le quali non devono essere conservate in ambiente controllato, né una funzionalizzazione, tantomeno una polimerizzazione o un indurimento post formatura della membrana (fig. 2.5). Parte del mio periodo presso il centro ricerca IBM è stato finalizzato a rendere il processo riproducibile per manifattura su larga scala, semplificando i passaggi e introducendo strumenti più semplici, per ridurre il tempo necessario e i costi da sostenere, anche utilizzando particelle di piccole dimensioni. La forma dell'elettrodo è un altro parametro modificabile per migliorare le prestazioni e la sicurezza, utilizzando litio in forma di polveri o fibrosa, oppure introducendo il litio in una struttura tridimensionale che non agisca da materiale intercalante ma da guida per l'elettrodeposizione, fornendo una estensione superficiale elevata per deposizione e dissoluzione. Sono stati inoltre proposte architetture tridimensionali litiofiliche, che agiscono anche da collettori di corrente, all'interno delle quali il litio non è introdotto per via elettrochimica ma fuso ed infiltrato per capillarità

Aerogel di grafene ossido ridotto

Il grafene è la forma allotropa bidimensionale del carbonio, nella quale gli atomi hanno una ibridazione sp^2 e sono organizzati secondo uno schema esagonale regolare su un piano flessibile di spessore monoatomico. È dotato di eccezionali caratteristiche fisiche e chimiche che gli conferiscono un enorme potenziale applicativo, specialmente in elettronica ed immagazzinamento di energia. Tra i vari metodi per fabbricarlo, la sintesi top-down tramite riduzione del grafene ossido (GO), forma altamente difettuale del materiale, è promettente per la produzione di massa del materiale, poiché il GO può essere prodotto in grande quantità e successivamente ridotto mediante diversi metodi. Il GO può essere utilizzato come mattone per costruire macrostrutture tridimensionali complesse ma ben definite chiamate aerogel, caratterizzate da difetti come vacanze, legami ricostruiti e gruppi funzionali. Gli elementi costitutivi sono caratterizzati da una flessibilità intrinseca che costituisce un elemento fondamentale dei reticoli interconnessi e porosi, poiché le pareti dei pori, fatte di lamine impilate, sono in grado di piegarsi senza rompersi. Questi network sono dotati di una elevata e facilmente accessibile area superficiale specifica, un ordine di grandezza inferiore rispetto a quella teorica del grafene, oltre che alla significativa porosità interna con dimensioni dei pori anche inferiori ai 2 nm, che dota questi materiali di una densità estremamente ridotta (fig. 3.1). Nonostante la leggerezza, queste strutture sono do autoportanti e posseggono una elevata elasticità, flessibilità e resilienza grazie ai legami fisico-chimici tra le lamine, al contrario dei comuni aerogel, tenuti assieme da deboli forze elettrostatiche, e sono in grado di sopportare pesi svariate volte superiori al loro. Questi network sono inoltre buoni conduttori elettronici grazie alla restaurazione degli orbitali π tipici degli anelli aromatici, che conferiscono anche una rilevante conduttività termica, a seguito di riduzione e alla formazione di contatti tra i vari foglietti di GO. L'RGO è inoltre dotato di proprietà catalitiche superiori agli altri materiali carboniosi riguardo la reazione di riduzione dell'ossigeno, agendo in combinazione con un eventuale catalizzatore presente sulla superficie. Le proprietà elettroniche e catalitiche sono fortemente influenzate dalla concentrazione e distribuzione dei difetti sulla superficie, i quali permettono di fornire al materiale proprietà specifiche ed introducono una proprietà unica e peculiare per questo materiale: la litiofilicità. Questa affinità con il litio metallico distingue l'RGO dagli altri materiali a base carbonio, i quali hanno una scarsissima bagnabilità da parte del litio liquido (fig. 3.2).

Le proprietà uniche di questo materiale nanostrutturato lo hanno reso un componente fondamentale in applicazioni di accumulo e conversione energetica. La morfologia tridimensionale porosa permette alla maggior parte della superficie di essere esposta in maniera utile all'elettrolita, per un facile accesso delle specie reattive ed una loro rapida diffusione. Questi aerogel sono stati impiegati come materiali catodici per differenti tipi di batterie e supercondensatori, grazie alla possibilità di accomodare agevolmente le variazioni volumiche, anche in combinazione con i convenzionali materiali catodici, ma soprattutto per la realizzazione di ibridi cosintetizzati, per sfruttare appieno i vantaggi introdotti da entrambi i materiali. L'RGO rappresenta il miglior compromesso per la realizzazione dei catodi per sistemi Li-S, grazie alla struttura robusta e l'organizzazione gerarchica della porosità, con i piani basali e i gruppi funzionali superficiali che permettono di ancorare, rispettivamente, lo zolfo e i polisolfuri, immobilizzandoli nell'area del catodo. La facilità di funzionalizzazione di questo materiale permette di incrementare le caratteristiche favorevoli alla ritenzione dei reagenti e le proprietà fisico-chimiche, specialmente potendolo direttamente ibridizzare introducendo zolfo nel reticolo con differenti metodi di sintesi. L'RGO soddisfa inoltre tutti i requisiti richiesti al materiale costituente il catodo in una batteria Li-O_2, grazie anche in questo caso alla porosità bimodale, dove i pori di maggiori dimensioni agiscono da canali di rapida diffusione e quelli di piccolo taglio da zone di accumulo dei prodotti di scarica, oltre alla buona conduttività elettronica e alla stabilità chimica e strutturale. La possibilità di funzionalizzare la superficie permette di incrementare la stabilità e la capacità catalitica, già di per sé elevata grazie all'elevata superficie specifica, la quale è buona per la reazione di riduzione dell'ossigeno ma è insufficiente per la successiva reazione di evoluzione, la quale richiede l'introduzione di un catalizzatore, la quale è facilmente ottenuta per cosintesi durante fabbricazione dell'aerogel. Tutte queste soluzioni sono accomunate dalla possibilità di non introdurre né un binder né un agente legante o funzionalizzante tra RGO e catalizzatore.

L'RGO è stato anche testato come additivo in ridotta quantità negli elettrodi per aumentare la conduttività e garantire l'apporto di elettroni al materiale attivo durante reazioni redox, il quale solitamente è dotato di scarsa capacità conduttiva. Questo materiale, al contrario del più convenzionale carbon black, grazie alla sua estensione superficiale permette di incrementare le prestazioni perché permette di avvolgere il materiale di interesse, garantendo una più ampia ed efficiente superficie conduttiva rispetto alle particelle carboniose classiche, che garantiscono un contatto, invece, puntuale. Oltre ad essere un additivo, il grafene ossido ridotto può agire da collettore di corrente leggero e flessibile, riducendo la densità energetica gravimetrica della batteria. Questo stesso materiale è stato utilizzato anche come strato protettivo per collettori di corrente metallici, per evitarne il degrado, ma anche come coating sottile depositato sui separatori delle batterie per ottenere una efficace soppressione della crescita dendritica, grazie all'introduzione di eteroatomi nella sua struttura che generano una carica negativa che comporta una maggiore adesione interfacciale con la superficie dell'anodo, mantenendo il flusso ionico costante.

I materiali carboniosi sono ampiamente utilizzati come materiali di intercalazione del litio perché garantiscono elevate capacità a costi contenuti e con maggiore affidabilità a lungo termine, grazie alla stabilità dimensionale. I carboni litiati vengono formati per reazione elettrochimica tra il materiale ospitante e gli ioni di litio, i quali penetrano nel reticolo del materiale ospitante, dotato di conducibilità sia elettronica che ionica, localizzandosi tra i piani basali della grafite, distanziandoli e modificandone l'impilamento. Questo processo è reversibile, poiché durante la fase di scarica avviene l'estrazione degli ioni dalla struttura. Una leggera ossidazione della grafite migliora le sue prestazioni come materiale intercalante, poiché gli ioni si localizzano in prossimità dei difetti cristallini, dove tendono ad accumularsi. Considerate queste premesse, il grafene ossido ridotto è il candidato più adatto ad essere utilizzato come materiale intercalante, data la sua struttura carboniosa conduttiva e la presenza di difetti intrinseci, i quali agiscono da punti di nucleazione per la deposizione del litio, che è proprio indotta dalla presenza dei difetti, presenti in gran numero sulla estesa superficie interna, che può essere agevolmente e precisamente controllata, così come numero e tipo di difetti e porosità. L'RGO garantisce una capacità teorica di immagazzinamento del materiale attivo pari a più del doppio di quella della grafite grazie al differente prodotto di elettroinserimento e al seguente accumulo sulla superficie di litio metallico, con una distribuzione omogenea e uniforme. La deposizione preferenziale del litio nelle vicinanze dei difetti (fig. 3.3), alla cui concentrazione è direttamente correlata la capacità disponibile, e all'interno delle porosità di piccolo taglio, che limitano le dimensioni massime del deposito, garantiscono una elevata reversibilità del processo di elettrodeposizione e un minore deterioramento dell'anodo, con una perdita contenuta di materiale attivo. Gli atomi di litio hanno una elevata affinità non solo per i difetti di reticolo quali irregolarità e vacanze, ma anche per eteroatomi inseriti tramite dopaggio del materiale e specialmente per gruppi funzionali contenenti ossigeno derivanti dall'ossidazione del GO precursore, che incrementano la bagnabilità del materiale da parte del litio metallico (fig. 3.4). L'RGO garantisce migliori prestazioni del grafene nell'accumulo del litio perché le pareti spesse dei pori vincono la repulsione tra gli ioni positivi, favorendone la deposizione.

Il particolare metodo di intercalazione del grafene ossido ridotto permette l'utilizzo di litio metallico in ogni tipo di batterie, combinando le proprietà del materiale con l'abilità intrinseca di soppressione delle dendriti. Una struttura autoportante composta di solo RGO agisce allo stesso momento da scaffold senza legante per il componente attivo, additivo conduttore e collettore di corrente, senza la necessità di introdurre materiali ausiliari. La flessibilità dell'elettrodo così realizzato ne permette l'impiego in dispositivi flessibili senza il rischio di rotture o perdita di prestazioni. Al posto dell'elettrodeposizione, che richiede l'impiego di una cella sacrificale, è possibile introdurre il litio all'interno del network per capillarità dopo averlo fuso, ottenendo un intrappolamento più omogeneo ed uniforme, contenendo le variazioni dimensionali dell'elettrodo.

Il grafene ossido è il perfetto elemento di partenza per la costruzione di strutture tridimensionali, grazie alla sua architettura bidimensionale dotata di un elevato numero di punti di ancoraggio. Il GO viene prodotto per esfoliazione della grafite mediante agenti fortemente ossidanti che introducono ossigeno nella struttura sotto forma di gruppi funzionali casualmente distribuiti sulla superficie, i quali stabilizzando la dispersione in acqua dello stesso, rendendolo idrofilo, anche se mantiene una importante idrofobicità sul piano basale (fig. 3.5). La riduzione a RGO può essere conseguita per via chimica o termica, che ristabilisce la struttura aromatica, comportando un riordino e impilamento delle lamine prima esfoliate. L'aggregazione degli elementi costituenti bidimensionali dispersi in acqua può dare vita ad idrogel con morfologia ordinata e controllata da ordine a lungo raggio, ottenuti tramite gelazione delle lamine di GO con elevato rapporto di forma. Esistono diversi approcci per formare queste strutture ordinate, ed il più immediato è l'utilizzo di un agente templante sopra il quale far accrescere la struttura mediante aggregazione del GO, in modo simile a come avviene per la fabbricazione di grafene mediante deposizione CVD, che ne ricopierà la morfologia, e dall'interno della quale il modello deve essere successivamente rimosso. La sospensione di GO in un solvente può essere inoltre spruzzata, e con questo metodo è possibile creare strutture cave assemblate attorno alle gocce di aerosol che vengono immesse in un ambiente riducente. Un ulteriore metodo per ottenere una struttura fortemente ridotta è quello di creare uno strato compatto di GO e sottoporlo ad una riduzione che genera specie gassose che fanno espandere la struttura, formando le porosità dovute al rilascio dei gas.

Materiali e metodi

Il metodo di produzione più utilizzato per ottenere strutture 3D interconnesse a partire da GO è l'auto-assemblamento delle lamine in un processo sol-gel, con la riduzione effettuata contemporaneamente alla formazione dell'architettura in maniera controllata. La riduzione delle lamine di grafene ossido ne riduce la repulsione reciproca e favorisce un avvicinamento seguito dalla sovrapposizione casuale e coalescenza delle stesse. Quando l'equilibrio viene rotto si ha la gelazione della struttura, la quale diviene sempre più rigida con il proseguire della riduzione a causa dell'aumento dei legami tra le lamine, le quali incorporano tra loro grandi quantitativi di acqua. Questo tipo di meccanismo è peculiare del grafene ossidato, che forma un network altamente interconnesso grazie alla presenza dei gruppi funzionali altamente reattivi, che formano legami tra i layer. La gelazione può essere attivata in diversi modi, tra cui una variazione di pH, inserimento di agenti leganti o innalzamento della temperatura in ambiente inerte o acquoso. Dopo aggregazione, è necessario rimuovere il solvente dalla struttura. La concentrazione di GO in soluzione ha un ruolo fondamentale per garantire la corretta aggregazione dell'idrogelo, poiché garantisce una sufficiente sovrapposizione degli elementi costituenti e quindi un corretto collegamento. È possibile effettuare una ulteriore riduzione sull'aerogel per diminuirne il contenuto di ossigeno, inducendone una contrazione. Le tecniche di autoassemblaggio permettono di integrare in maniera uniforme nell'architettura dei composti inorganici a partire dai precursori, per formare degli ibridi.

Tra i processi di auto-assemblaggio, la sintesi idrotermale offre la maggiore facilità di funzionalizzazione delle strutture e la possibilità di produrre grandi quantità di materiale. La riduzione del materiale è effettuata in condizioni cosiddette idrotermali, cioè ad alta temperatura (120-180°C) e pressione (1-100MPa) per un tempo compreso tra 1 e 20 ore. Questi parametri hanno un importante effetto sulla velocità e i risultati della reazione, con una temperatura inferiore che richiede maggiore tempo per portare a completamento la riduzione. La deossigenazione si basa sull'utilizzo di acqua sovrariscaldata in condizioni di non equilibrio senza la necessità di inserire ulteriori agenti chimici, pertanto il processo non è impattante sull'ambiente. L'utilizzo di un mezzo acquoso favorisce la diffusione dei reagenti, intensificando gli effetti termici. Quando l'acqua è sottoposta ad un riscaldamento in un sistema chiuso, genera una pressione interna che modifica le proprietà fisico-chimiche dell'acqua stessa, la quale si avvicina alle sue condizioni critiche. Se l'acqua viene riscaldata al di sopra del suo punto di ebollizione aumenta il suo grado di dissociazione, agendo sia da solvente che da reagente, dato che l'idrolisi la rende un acido o base sempre più forte al crescere della temperatura, che favorisce anche la mobilità di molecole e ioni nel mezzo. Il pH della soluzione ha un ruolo fondamentale a definire il meccanismo di riduzione. La sintesi idrotermale deve essere condotta in apposite autoclavi, adatte a sostenere le elevate pressioni prodotte, con all'interno contenitori inerti anche ad alta temperatura.

Il processo idrotermale genera legami sia chimici che fisici, poiché avviene una perdita di massa correlata con la produzione di piccole molecole quali CO_2, acqua e frammenti organici (fig. 3.7), ma c'è allo stesso tempo una interazione tra gli orbitali π reinstaurati nella struttura. Dato che la reazione avviene in un sistema chiuso e sigillato, è difficile poterne seguire l'evoluzione e tutte le considerazioni sul meccanismo sono effettuate a posteriori. Le molecole prodotte derivano dalle reazioni chimiche che intercorrono tra i gruppi funzionali, i quali condensano dopo ripiegamento di un layer oppure collegando le varie lamine di GO. Data la complessità strutturale del grafene ossidato non è possibile definire una formula di struttura in maniera univoca, ma è soltanto possibile ipotizzare quali gruppi funzionali sono presenti all'interno e come questi possano interagire tra loro. La coalescenza produce una architettura con una estensione superficiale estremamente più bassa rispetto agli elementi costitutivi di partenza, ma conferisce una resistenza meccanica elevata e una buona capacità di recupero delle deformazioni, grazie alla flessibilità delle pareti dei pori, che si ripiegano su sé stesse quando il network è sottoposto ad una sollecitazione. All'interno delle porosità è intrappolata dell'acqua residua, anche grazie alla presenza di gruppi funzionali residui, che costituisce più del 95% della massa totale dell'idrogelo, e va eliminata con un passaggio di liofilizzazione, che, se eccessivamente violento, può causare un danneggiamento della struttura. La sintesi idrotermale è ampiamente utilizzata per la preparazione di nanomateriali inorganici a partire da precursori a temperature di reazione simili a quelle impiegate per la riduzione del GO, pertanto questo processo permette di fabbricare agevolmente ibridi unendo nella miscela di reazione i precursori.

L’efficacia della riduzione può essere incrementata aggiungendo nel sistema degli agenti coadiuvanti, senza la necessità di innalzare la temperatura o allungare i tempi di reazione. È possibile impiegare dei catalizzatori, degli pontanti o degli agenti riducenti. La maggior parte dei riducenti impiegati, soprattutto contenenti azoto, agiscono anche da fonti di eteroatomi da inserire nella struttura, che da agenti espandenti, dato che la loro ossidazione produce molecole gassose che contribuiscono a formare la struttura porosa. L’utilizzo di questi reagenti, però, richiede l’introduzione di un passaggio di purificazione dopo sintesi per rimuovere i residui di specie chimiche pericolose o estranee al sistema, che ne potrebbero inficiare le prestazioni. Per evitare la successiva pulizia, è possibile utilizzare agenti riducenti contenenti gli stessi elementi del RGO, carbonio, ossigeno e idrogeno, tra i quali spicca l’acido ascorbico.

L’acido ascorbico, anche detto vitamina C, è un agente riducente naturale non tossico che è uno dei componenti fondamentali della dieta umana. È stato ampiamente utilizzato come riducente in ambito scientifico date le sue caratteristiche, ed è un sostituto ideale dell’idrazina come agente riducente del grafene ossido. In acqua deprotona, innescando un meccanismo di deossigenazione elettrofila, che comporta la condensazione dei gruppi funzionali più labili e la riduzione a RGO, che può avvenire anche a temperatura ambiente. L’aggiunta della vitamina C nella dispersione di GO non richiede alcun aggiustamento o modifica, e il meccanismo di riduzione chimica può cooperare simultaneamente con quello derivante dalla dissociazione dell’acqua in condizioni idrotermali, e permette un maggiore controllo sulle condizioni di riduzione.

Il riscaldamento della miscela reagente può essere anche eseguito mediante una irradiazione di microonde, che possono accelerare il processo e ridurre il tempo necessario alla reazione. La tecnica basata sulle microonde è più rapida, conveniente e versatile della tecnica convenzionale, poiché permette un riscaldamento omogeneo localizzato solo all’interno del mezzo di reazione, minimizzando i sottoprodotti e massimizzando rendimento, controllo e riproducibilità. I reattori a microonde permettono un controllo accurato dei parametri di reazione, i quali possono essere modificati immediatamente grazie al controllo sulla potenza di irradiazione delle microonde. La temperatura del mezzo viene aumentata per riscaldamento dielettrico, che deriva dalla variazione della direzione del momento di dipolo indotta dalla variazione del campo elettromagnetico esterno all’ambiente di reazione. L’energia elettrica è convertita in energia cinetica, e a sua volta in energia termica. La miscela di reazione deve essere contenuta in un materiale trasparente alle microonde ma in grado di sostenere rapidi innalzamenti e mantenimenti ad alta temperatura per lungo tempo. L’acqua ha un assorbimento medio delle microonde ma permette una elevata profondità di penetrazione della radiazione, garantendo un riscaldamento di tutta la massa omogeneo e immediato, molto più rapido del riscaldamento per convezione e conduzione su cui si basa la sintesi idrotermale convenzionale, che vede prima il riscaldamento del contenitore e poi del contenuto. Oltre ai parametri di reazione classici, l’utilizzo prevede l’inserimento della potenza di irradiazione come ulteriore criterio da tenere in considerazione. L’irraggiamento con microonde è ampiamente impiegata per la sintesi sia organica che inorganica a partire da precursori ed è stata utilizzata nell’ambito del RGO per aumentare il grado di riduzione.

Il grafene ossido monolayer utilizzato come materiale di partenza di questo lavoro è stato disperso in 17mL soluzione di acqua deionizzata e vitamina C (1 mg/mL) con una concentrazione di 2 mg/mL, lasciata riposare per 5 ore e successivamente sottoposta ad ultrasonicazione per 30 minuti per promuovere la disaggregazione delle nanosheets. Per ridurre il materiale con sintesi idrotermale convenzionale (HS), la sospensione è stata rapidamente trasferita in un reattore di Teflon da 25mL, collocato a sua volta in una autoclave introdotta velocemente in forno a 100°C per evitare la precipitazione sul fondo del reattore della fase solida. La reazione è stata condotta, con una velocità di riscaldamento di 150°C/h a 180°C per 12 ore. Dopo raffreddamento naturale a temperatura ambiente, l'autoclave è stata aperta e l'acqua rimossa per permettere un agevole recupero dell'idrogelo cilindrico flottante, della stessa forma dell'interno del reattore ma con un volume nettamente inferiore. Per ottenere l'aerogel, il campione è stato inserito in un tubo portacampione e immerso in azoto liquido, quindi introdotto in un liofilizzatore per rimuovere il solvente per sublimazione durante la notte. Per eseguire la riduzione mediante riscaldamento con microonde (MAHS), il procedimento seguito è stato lo stesso della sintesi convenzionale, con la differenza che il volume della soluzione è stato ridotto a 4mL con stessa concentrazione, e questa è stata introdotta velocemente in un contenitore di pyrex, successivamente inserito rapidamente nel reattore a temperatura ambiente. La reazione è stata condotta a 180°C per un'ora ad una pressione di circa 14 bar, con una rampa di riscaldamento di 50°C/min e un raffreddamento forzato con un getto di azoto, dopo il quale l'idrogel, della stessa forma del contenitore di reazione, è stato estratto.

La maggiore differenza tra i due processi, a parte la velocità di riscaldamento e raffreddamento, è la possibilità di controllo e monitoraggio dei parametri di reazione garantita dal reattore a microonde e le limitazioni sui valori massimi raggiungibili dai due sistemi (fig. 4.6). Nella reazione con riscaldamento da microonde temperatura e pressione sono indirettamente misurate e sono indirettamente controllate dalla potenza variabile di irraggiamento. Il sistema riscaldato con le microonde raggiungeva solitamente la pressione limite prima della temperatura target, pertanto il sistema era costretto a diminuire la potenza per garantire un continuo riscaldamento e mantenere allo stesso tempo la pressione sotto il valore di soglia. Temperature e tempi di reazione inferiori sono stati testate per entrambi i processi (per le microonde anche potenze inferiori variabili o costanti) ma in nessun caso è stato raggiunto il self-assembly dell'idrogelo come nelle condizioni sopramenzionate, pur avendo la conferma immediata della avvenuta riduzione, dato il cambio di colore della soluzione da marrone a nero. Nel sistema idrotermale convenzionale non è nota la pressione raggiunta all'interno, mentre nel sistema MW non è stato possibile innalzare la temperatura al di sopra di 180°C poiché il sistema avrebbe ecceduto la pressione massima consentita.

L'aspetto più interessante della reazione mediata dalle microonde è stata la possibilità seguire l'evoluzione in tempo reale della reazione non solo mediante i parametri di reazione ma anche grazie ad una videocamera integrata puntata sul contenitore di reazione, illuminato dal basso da una luce LED per permettere una migliore visibilità. Dal video è stato possibile valutare il meccanismo macroscopico di assemblaggio da parte del GO (fig 4.7). La soluzione, inizialmente omogenea e di colore marrone, al passare del tempo è diventata sempre più chiara, sintomo dell'evolversi della reazione. Dopo circa 20 minuti la soluzione, ormai di colore grigio chiaro, mostrava un elemento di grandi dimensioni galleggiare sul pelo dell'acqua e un ammasso di residui scuri depositati sul fondo, mentre piccoli fiocchi neri si muovevano caoticamente nel mezzo acquoso. Al passare del tempo la soluzione ha perso completamente colore e i piccoli fiocchi in movimento sono cresciuti di dimensione e continuavano ad impattare contro sia l'elemento flottante, risultato poi essere l'idrogelo, che contro i residui sul fondo. A fine reazione, durante la fase di raffreddamento, tutti i flakes sono messi in movimento caotico dal raffreddamento dal basso, mentre l'idrogel rimane galleggiante fino ad una temperatura di circa 100°C, per poi affondare lentamente sul fondo.

Caratterizzazione fisico-chimica

È stata eseguita una caratterizzazione fisico-chimica dei campioni dopo freeze-drying per valutare le differenze tra i risultati dei due processi di sintesi. Il materiale di partenza verrà in seguito definito come “GO”, il materiale ottenuto da sintesi idrotermale come “HT-RGO” e quello da sintesi idrotermale assistita da microonde “MW-RGO”.

L’analisi morfologica, eseguita con un microscopio a scansione elettronica, ha mostrato che HT-RGO è provvisto di un network ben definita e tridimensionale, consistente in una struttura simil-spongiosa con porosità aperte gerarchicamente distribuite e interconnesse, con pori di dimensioni da subnanometriche a diversi micrometri (fig. 4.8). Le pareti dei pori sono caratterizzate da regioni planari increspate e ripiegate, dovute al avvicinamento da direzioni casuali degli elementi costitutivi e al successivo collegamento e impilamento (fig. 4.9). L’architettura corrugata è caratteristica anche del materiale ottenuto per MAHS, il quale ha una struttura più irregolare e grossolana, dovuta alla reazione più drastica e violenta che causa un ammassamento maggiore e più compatto dei layer. Nella HS i flussi termici convettivi sono più regolari grazie alla direzionalità di riscaldamento dall’esterno all’interno, determinando un assemblamento più delicato, mentre le microonde provocano un riscaldamento massivo dell’intero mezzo di reazione, risultando in una agglomerazione più disordinata e caotica. Le osservazioni morfologiche sono confermate dai risultati dell’analisi di adsorbimento-desorbimento superficiale di azoto per la determinazione dell’estensione superficiale specifica. Dalle curve è risultata una superficie specifica per HT-RGO di 510m^2/g, doppia rispetto a quella di MW-RGO, 277 m^2/g, dovuta anche questa verosimilmente alla violenza del riscaldamento durante sintesi. La distribuzione dimensionale volumetrica dei pori mostra una organizzazione dei pori gerarchica non bimodale (fig. 4.11 & fig. 4.12), confermando sostanzialmente le evidenti differenze in termini di microstruttura emerse dalle precedenti osservazioni al SEM. L’impiego di sola acqua supercritica come agente riducente fa sì che il maggior contributo al volume totale di porosità sia dato da pori di dimensione inferiore ai 40Å, mentre l’introduzione di un agente riducente permette di spalmare il contributo su una distribuzione dimensionale più ampia. In HT-RGO i pori al di sotto dei 40Å danno il maggiore contributo anche all’estensione superficiale, mentre la porzione collegata alla stessa dimensione in MW-RGO è sensibilmente inferiore. Questo si riflette nella differenza di comportamento tra i due idrogeli, dato che quello da HS galleggiava, poiché al suo interno erano presenti porosità contenenti solo gas e non liquido, mentre quello ottenuto da MAHS affondava, poiché tutti i pori erano invasi dal mezzo di reazione, con un contributo risibile della microporosità a causa della reazione più rapida. L’analisi strutturale per mezzo di diffrazione a raggi X (fig.4.13) ha mostrato che il campione GO è caratterizzato da un picco molto stretto a circa 12°, tipico del grafene ossido, corrispondente ad una spaziatura media interlayer di 7.33Å attribuibile alla repulsione tra i piani indotta dalla presenza dei gruppi funzionali ossidati sul piano basale, mentre i due campioni contenenti RGO mostrano un picco prominente a circa 24°, indicatore di una corretta riduzione del materiale. La deossigenazione è comunque parziale, ed è dimostrato dalla spaziatura interlayer media di circa 3.70Å, la quale è leggermente superiore a quella della grafite pura (3.36Å), che indica una permanenza di gruppi funzionali residui non eliminati durante la fase idrotermale, che possono eliminati effettuando una successiva riduzione ulteriore. Dallo spettro XRD è stato possibile inoltre dedurre, dalla larghezza del picco caratteristico, che i layer non hanno ordine a lungo raggio lungo la direzione di impilamento, implicando che le pareti dei pori sono formate da un numero di layer di RGO variabile tra 1 e 3.

La stabilità termica è stata studiata con una termogravimetria (fig. 4.14), utile anche a valutare il comportamento del materiale quando riscaldato rapidamente in un ambiente inerte, per simulare lo shock termico che subisce il materiale in glovebox quando posto a contatto con il litio metallico fuso. Il GO mostra una rapida perdita di peso all'aumentare della temperatura, mentre gli RGO mostrano una buona stabilità termica durante tutto il test. Oltre ad una prima veloce perdita di peso a temperature inferiori ai 100°C dovuta all'eliminazione dell'acqua fisisorbita nel materiale, circa il 10% nel GO e meno dell'1% nell'RGO a dimostrare la predominante idrofobicità, il GO subisce due drastiche perdite di massa dovute alla decomposizione prima di gruppi funzionali più labili termicamente, come ossidrili, epossidici e carbossili, e poi l'eliminazione di funzionalità più stabili come carbonili e fenoli. La perdita di massa nei materiali ridotti è invece più lenta e costante, a dimostrazione della eliminazione della maggior parte delle specie ossidate durante riduzione, ad esclusione di quelle più stabili. La perdita di massa alla temperatura di interesse di 250°C è inferiore al 10%. La predominanza del meccanismo chimico sul meccanismo idrotermale è mostrata dalla posizione delle perdite di massa, indicata dalla derivata della curva gravimetrica, che sono nella stessa posizione della TGA relativa ad un RGO ridotto solo chimicamente mediante acido ascorbico. La spettroscopia Raman (fig. 4.15), tecnica principale per lo studio dei materiali carboniosi, mostra che l'indice di difettosità nel reticolo cresce riducendo il materiale, ed è superiore nel HT-RGO rispetto al MW-RGO, a causa della reazione più blanda e lenta, ed è dovuto alla maggiore presenza di legami con atomi di carbonio con ibridazione tetraedrica sp^3, i quali costituiscono delle imperfezioni in un reticolo a maggioranza di atomi con ibridazione planare sp^2. L'ampiezza a mezza altezza del picco G non ha subito una variazione sensibile, indicando che è stato generato dai bordi e non dai difetti strutturali sul piano basale, e il picco relativo ai difetti del MW-RGO è più ampio rispetto a HT-RGO, indicante una maggiore frammentazione dei domini grafitici, che si impilano in maniera più disordinata esponendo meno bordi all'esterno a causa della violenza della reazione. L'assenza dei picchi D' e G' può essere dovuta alla lunghezza d'onda utilizzata per effettuare l'analisi. La distanza media tra i difetti può essere calcolata, ed è risultata essere 12 nm per GO e circa 10 nm per RGO. L'evoluzione dei gruppi funzionali a seguito della riduzione è stata studiata mediante spettroscopia infrarossa (fig. 4.16). Lo spettro relativo al GO mostra picchi relativi all'acqua fisisorbita e ai gruppi funzionali contenenti ossigeno con all'interno atomi di carbonio ibridati sp^2 e sp^3 e gruppi metilici e metilenici. Dopo riduzione, tutti i picchi relativi ai gruppi termolabili sono spariti, e sono rimasti solo i picchi relativi a gruppi funzionali più stabili come gruppi carbonilici ed esterici, indicante una elevata ma incompleta deossigenazione e un cross-link tra i vari flakes, oltre al picco relativo a doppio legame tipico dei gruppi aromatici. La deossigenazione può essere efficacemente provata mediante la definizione del rapporto tra le concentrazioni relative di carbonio ed ossigeno misurate mediante una spettroscopia XPS. L'introduzione della vitamina C nel sistema permette di ottenere un rapporto C/O da entrambe le tecniche confrontabile con le riduzioni chimiche a bassa temperatura e superiore all'utilizzo della sola acqua in condizioni supercritiche. Dallo spettro ad alta risoluzione (fig. 4.18) dopo riduzione si nota la sparizione, in accordo con lo spettro FTIR, dei picchi relativi ai gruppi funzionali più termolabili ma non quella dei picchi più termoresistenti, con una predominanza dei gruppi esterici derivanti dalla condensazione dei gruppi carbossilici. Lo spettro mostra inoltre la presenza di un picco tipicamente associato al grafene con pochi layer impilati, d'accordo con i risultati XRD, anche se caratterizzato da una elevata densità di difetti.

Fabbricazione strato protettivo e caratterizzazione elettrochimica

L'obiettivo pratico di questo lavoro di tesi era la definizione di un processo produttivo semplice, rapido e poco costoso di una membrana self-standing da introdurre su del litio metallico per sopprimerne la crescita dendritica durante ciclaggio. Gli aerogel sono stati ridotti in polvere mediante macinazione in un mortaio, durante la quale è stato aggiunto il 5% wt di PTFE come agente legante. La polvere grossolana così ottenuta è stata quindi introdotta in uno stampo modulare con foro circolare di 12mm, conveniente per un facile recupero della membrana dopo pressatura (fig 5.1), e successivamente sottoposta ad una pressione costante di 5 tonnellate per 30 secondi, in modo da compattare sufficientemente le polveri, le quali senza legante non starebbero assieme. L'analisi SEM delle membrane ha mostrato che la microstruttura è stata completamente distrutta dalla pressatura, e che quindi le membrane risultano identiche da un punto di vista morfologico, ma quelle derivanti da polvere di MW-RGO hanno uno spessore di circa 85μm mentre quelle da HT-RGO circa 65 μm (fig. 5.2), e questa differenza è dovuta alla difficoltà nel pesare accuratamente i quantitativi di polveri immesse dentro lo stampo. Dopo rimozione dallo stampo, le membrane sono state asciugate in vuoto a 70°C per 24 ore, per rimuovere l'umidità residua all'interno ed eventuali molecole volatili in modo da non contaminare l'ambiente all'interno della glovebox o provocare reazioni non desiderate.

La valutazione delle prestazioni elettrochimiche è avvenuta posizionando le membrane su un disco di litio metallico, fuso a 250°C su uno spacer o all'interno di un cap positivo per favorirne l'adesione, indicata dal formarsi di una depressione al centro, inserendo dopo raffreddamento l'insieme all'interno di una batteria CR2032. Lo spessore delle membrane non ha permesso l'inserimento di un altro spacer, determinando una asimmetricità della cella. Come elettrolita sono stati usati 100 μL di $LiPF_6$ 1M in EC/DMC (1:1) con separatore Toray (fig. 5.3).

La stabilità elettrochimica è stata testata con un ciclaggio galvanostatico (fig. 5.4), imponendo una corrente costante di 1 mA/cm^2 e una limitazione di potenziale a $\pm 1V$. La cella di riferimento subisce corto-circuito a circa 95 cicli dopo una rapida crescita del sovrapotenziale a causa dell'ispessimento del SEI, durante la quale il profilo di voltaggio cambia a causa dell'accumulo di litio "morto" che rende più tortuoso il percorso di deposizione degli ioni litio. Le celle contenenti le membrane non hanno subito corto-circuito durante ciclaggio perché c'è stata una effettiva soppressione della crescita dendritica, ma il gap di potenziale è eccessivamente superiore a quello iniziale della cella simmetrica con litio, pur rimanendo costante per un periodo doppio a quello di fallimento del riferimento, a causa dell'impedimento alla conduzione introdotto dall'elevato spessore delle membrane, indicato dal profilo del voltaggio. Dopo una iniziale irregolarità, il ciclo si è stabilizzato per lungo tempo, mostrando un lento accrescimento del sovrapotenziale a causa dell'ispessimento irregolare e continuo del SEI sopra la membrana, il quale non è centrato attorno allo zero e cresce in maniera asimmetrica a causa dell'asimmetricità della cella per quanto riguarda assemblaggio e quantità di materiale nelle membrane. Il MW-RGO forma una membrana più spessa, inducendo un sovrapotenziale eccessivo, mostrando inoltre un necking caratteristico della formazione di dendriti sotto la membrana.

La crescita del SEI durante ciclaggio può essere studiata mediante spettroscopia elettrochimica di impedenza, che fornisce dei plot di Nyquist (fig. 5.6) interpretati tramite un circuito equivalente contenente contributi dell'elettrolita, del SEI e dell'interfaccia con cui può essere modellizzata la cella. La cella di riferimento mostra una elevata resistenza interfacciale prima di ciclaggio a causa della presenza degli ossidi nativi. La resistenza dell'elettrolita cresce a causa del suo consumo e dell'accumulo al suo interno dei prodotti di degradazione, mentre la resistenza totale diminuisce a causa della crescita delle dendriti a seguito di deposizione, che determina un aumento dell'estensione superficiale, fino alla penetrazione del separatore. Le celle contenenti RGO vedono una diminuzione della resistenza dell'elettrolita, il quale in assenza di litio "morto" riesce ad infiltrarsi nella membrana, la quale introduce una resistenza interfacciale enorme se comparata con la cella di riferimento. Entrambi i campioni mostrano un pronunciato contributo della diffusione allo stato solido, oltre ad una resistenza interfacciale crescente correlata alla rapida crescita di uno strato isolante sull'elettrodo e il deterioramento dei contatti tra membrana ed elettrodo. Questi risultati sono comunque correlati allo spessore della membrana, che comunque riescono ad allungare efficacemente il tempo di vita utile della batteria, poiché fino al doppio del tempo dopo cortocircuito del riferimento quella con spessore inferiore non mostra una crescita ritardata del SEI mentre l'altra più spessa non solo vede l'ispessimento di questo, correlato anche all'incremento del sovrapotenziale, ma anche la rapida crescita di dendriti al di sotto di essa, la quale non ha alcun effetto positivo.

Conclusioni e sviluppi futuri

In conclusione, possiamo affermare che grazie alle sue proprietà peculiari, il grafene ossido ridotto è un materiale promettente per garantire un miglioramento efficace nella sicurezza, affidabilità e prestazioni degli anodi di litio metallico.

L'utilizzo di vitamina C nella miscela reagente permette un controllo preciso ed efficace in termini assoluti e relativi sul grado di riduzione in modo semplice e non impattante, senza necessità di modificare temperatura e tempi, assicurando la buona riuscita della reazione, la quale è profondamente variabile utilizzando solo acqua come agente riducente. Gli aerogel ottenuti con i diversi metodi di produzione sono morfologicamente differenti ma chimicamente simili. La sintesi idrotermale convenzionale produce una morfologia più omogenea caratterizzata da micropori e una superficie specifica molto estesa, la quale è risulta dimezzata nel materiale ottenuto da sintesi idrotermale assistita da microonde, caratterizzato da una superficie più grossolana e irregolare, con assenza di microporosità a causa del rapido riscaldamento dell'intero volume di liquido senza una direzione preferenziale, che induce un moto caotico nella dispersione. Dal punto di vista chimico, i due materiali sono caratterizzati da una vasta rimozione dei gruppi funzionali superficiali contenenti ossigeno comparabile per entrambi i metodi, con una differenza di percentuale relativa del carbonio inferiore al 2%, risultando in un cambio di ibridazione, da tetragonale sp^3 degli atomi di carbonio ossidati alla planare sp^2 tipica degli anelli aromatici. Da questo si può dedurre che è possibile velocizzare la reazione di riduzione riducendo il tempo da 12 ore a una sola ora ottenendo praticamente le stesse proprietà chimiche grazie ad una deossigenazione indotta da un rapido riscaldamento con microonde, coadiuvato dalla presenza di un agente riducente, la cui reattività è accentuata dall'alta temperatura.

Le prestazioni elettrochimiche sono state incoraggianti, seppur differenti per i due materiali ed imputabili soprattutto alla differenza di spessore tra gli strati protettivi introdotti, poiché non sussistono importanti morfologiche o chimiche per giustificare un diverso comportamento. Lo spessore delle membrane è eccessivo sia in termini di proprietà elettrochimiche, poiché hanno provocato un incremento irregolare della resistenza interna della cella, ma anche macroscopicamente, poiché ostacolano la corretta chiusura della cella, imponendo una asimmetricità della stessa.

I risultati ottenuti aprono la strada ad ulteriori indagini per approfondire la conoscenza dei meccanismi sui quali si basa il self-assembly degli aerogel di RGO e per migliorare e raffinare la fabbricazione degli strati protettivi. Uno studio sistematico degli effetti della modifica delle variabili e dei parametri di processo, assieme ad un monitoraggio costante e una caratterizzazione *in-situ* della reazione in evoluzione sfruttando il contenitore di reazione trasparente, magari con l'aggiunta di precursori per l'introduzione di eteroatomi e sostanze inorganiche nella struttura, permetterebbe la definizione univoca del meccanismo, percorso e cinetica di reazione.

La riduzione dello spessore delle membrane mediante un processo di calandratura, e il loro impiego come separatori, permetterebbe di ridurre l'instabilità elettrochimica grazie ad una maggiore uniformità dimensionale e superficie più regolare, magari realizzando gli strati protettivi in assenza di un agente legante. Dopo la definizione del migliore processo produttivo e uno studio dell'effetto del passaggio degli ioni di litio attraverso la membrana, l'ultimo passaggio sarebbe la loro implementazione all'interno di una cella completa, utilizzando lo stesso materiale anche per realizzare il catodo, modificando eventualmente concentrazioni e precursori.

Table of Contents

List of Symbols and Acronyms

AA – Ascorbic Acid
BET – Brunauer-Emmett-Teller specific surface analysis
CB – Carbon black
CNT – carbon nanotubes
DFT – density functional theory
FESEM – Field emitting scanning electron microscope
FTIR – Fourier transform infrared Spectroscopy
GO – Graphene Oxide
HS – hydrothermal synthesis
HT-RGO – Hydrothermally synthesized Reduced graphene oxide
LCO – lithium-cobalt oxide
LFP – lithium-iron phosphate
LIB – Lithium ion battery
Li-O_2 – Lithium-air battery
Li-S – lithium sulfur battery
LMB – lithium-metal batteries
LMO – Lithium manganese oxide
LTO – lithium-titanium oxide
MAHS – microwave-assisted hydrothermal synthesis
MW-RGO – microwave-assisted Hydrothermally synthesized Reduced graphene oxide
OER – oxygen evolution reaction
ORR – oxygen reduction reaction
RGO – reduced graphene oxide
RS – Raman Spectroscopy
SEI – Solid Electrolyte Interface
SSA – Specific surface area
SSE – solid-state electrolyte
TGA – thermogravimetric analysis
XPS – X-ray photoelectron spectroscopy
XRD – X-ray diffraction spectroscopy

List of Figures

1. Introduction

1.1. *New generation batteries*

The depletion of fossil fuels and the need to reduce the global warming are pushing the demand for cleaner and more efficient energy storage devices, which need to guarantee overall security and reliability without affect efficacy, both in primary and secondary batteries (Song, M.K. et al., 2011).

Lithium-ion batteries performances, especially in the last few years, have improved significantly, meeting the needs of small dimension electronic devices and electric instruments, but still not sufficient to satisfy the requests for powering electric engines for automotive or provide reliable high energy density power supplies (Grande, L. et al., 2015). Therefore, innovative technologies with improved performances are under study and development to supply the increasing demand of higher power and energy density without increasing dimensions and weight of the energy storage unit. Among these new generations systems, mostly only in R&D phase, the most attractive thanks to their encouraging characteristics and results, are the lithium metal rechargeable batteries, especially lithium-air (Li-O_2), and lithium-sulfur (Li-S) batteries (fig 1.1).

The development of these technologies is essential for industrialized nations and developing countries. European Union started funding, in 2015, in the framework of the program called "Horizon 2020" , the research to realize, by the year 2020, a fully working Li-S battery with a practical specific energy of 500 Wh/kg, while U.S. Department of Energy sponsored the creation of a consortium called "Battery500", is composed by several national laboratories, like Brookhaven and Pacific Northwest, various universities, including Stanford University and University of California, and IBM as advisory board member, with the aim to develop a Li-O_2 battery able to provide 500 miles range to an electric vehicle on a single charge.

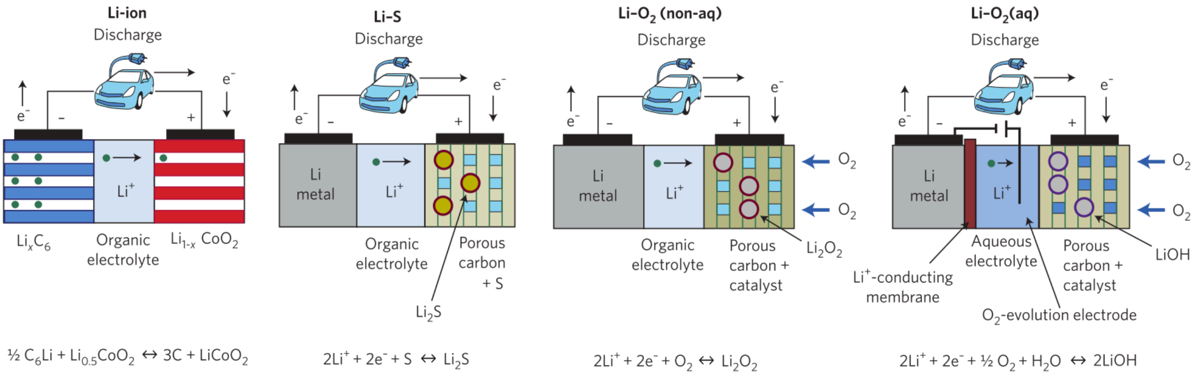

Figure 1.1: Comparison between Li-ion, Li-S and Li-O_2 batteries (*Adapted from Bruce, P.G. et al., 2011*)

1.1.1 Lithium-Sulfur Batteries

The Li-S system is characterized by a high theoretical specific energy density of 2,600 Wh/kg, value due to the specific capacity of sulfur, 1,673 mAh/g. This element is very attractive because of its low cost, wide abundancy and accessibility. Elementary sulfur can be found as a molecular solid, with the constituting molecules arranged or in linear chains or in a ring composed by eight atoms, called cyclo-octasulfur and represented with the symbol cyclo–S_8, which is the most stable form among the others (Xin, S. et al., 2017).

The Li-S battery generates electricity from electrochemical energy during the discharge phase by the disruption of the bonding between two S atoms in the molecule. The opening of the ring and the reduction of the resulting polysulfides Li_2S_n takes place on the positive electrode by the Li^+ ions shuttling towards the cathode, through the electrolyte, after being released from the anode. The various reductions, in order, are (Wild, M. et al., 2015):

$$S_8 \rightarrow Li_2S_8 \rightarrow Li_2S_6 \rightarrow Li_2S_4 \rightarrow Li_2S_3 \rightarrow Li_2S_2 \rightarrow Li_2S$$

The specific power of Li-S cells is much higher than power related to Li-ion batteries because the diffusion of small molecules and ions in a liquid electrolyte is faster than the insertion of Li^+ in the crystalline structure of the cathode.

Polysulfides with n=8,6,4,3 have a significant tendency to dissolve in organic electrolytes and diffuse towards the anode, where they form a passivation layer, causing a loss of active material on the positive side. the shuttling leads to a fast reduction of the capacity of the system before the formation of the lighter species, Li_2S_2 and Li_2S, that are not soluble in organic liquids. To avoid the depletion, a cathodic material can be used to improve the cycle stability, trapping the soluble lithium-sulfur salts and preserving them from moving towards the negative side during discharging. If the reduction of the polysulfides takes place on the metallic anode, the system is internally short-circuited, causing self-discharge when not operating or a decreasing efficiency and capacity every cycle (Xin, S. et al., 2017; Wild, M. et al., 2015)

The hosting cathodic material must withstand the change of volume determine by the substitution of the elementary sulfur with the polysulfides (with a density of 2.06 g/cm^3 for S and 1.66 g/cm^3 for Li_2S) during discharge, the phase transition between the soluble long-chain and insoluble short-chain polysulfides and the departure of deposited passivating species. (Grande, L. et al., 2015)

There is a wide range of materials to be used as cathode for Li-S cells: the first attempts saw the use of metallic lithium as anode, facing a positive electrode made of sulfur powder located on the surface of the current collector. This design, ensuring the highest theoretical capacity to the system, is affected by the insulating nature of the sulfur, making necessary the introduction in the system of a conductive material, that will be passivated anyway by the accumulation of the discharge products by adsorption in the surface. This adsorption will be delayed by the solubility; on the other hand, the conductor, is added in a small quantity (because not electrochemically active) avoiding to affect the performances, just like the binder, aimed to gather all the components (Manthiram, A. et al., 2015).

The cathodic materials are usually characterized by being micro and nanostructured materials with a very high specific surface to increase the electrochemical efficiency hosting as much adsorbed reduction products as possible, delaying as much as possible the complete passivation. A microporous/mesoporous architecture is the most suitable to accommodate sulfur and facilitate the species diffusion: this morphology is typical of the carbon materials, the most frequently used as cathodes in Li-S batteries. A lot of different carbon-based morphologies have been used, like CNT, nanoribbons, graphene and nanospheres (Yin, Y.X.

et al., 2013; Manthiram, A. et al., 2015). The confinement of the sulfur in the porous structure is controlled by capillarity, with a loss of efficacy in the effect with the increase of pores size. Nevertheless, the wider pores are fundamentally useful to facilitate the diffusion of the species, especially in a structure with hierarchically ordered pores (Ji, X, et al., 2009).

The non-polar nature of the carbon it is another characteristic that makes it a perfect host for sulfur, equally non-polar, but it's not suitable for the reaction products, because the polysulfides have a strong polarity, implying a low affinity with an only carbon surface. The bonding strength can be increased introducing low mass heteroatoms, functionalizing the surface or using a carbon material slightly oxidized, which causes a decrease in the conductivity properties (Zheng, G. et al., 2013). On the same line of thought researcher have tried to introduce sulfur directly in the carbon network or functionalizing the surface with polymers containing sulfur and polythiophenes or grafting polar/non-polar copolymers. Have been also tested Li_2S-C composites as cathodes, a discharged cell (Hassoun, J. & Scrosati, B., 2010).

Likewise, inorganic materials have been widely used as cathodic materials, to form a containment barrier around sulfur and preventing the polysulfides diffusion. The main disadvantage is the low electronic conductivity, that requires a conductive adjuvant in the system. Metal oxides has been employed to coat sulfur nanoparticles: Seh and colleagues, in 2013, realized a TiO_2 shell structure to avoid the removal pf soluble polysulfides, having an internal partially void space to accommodate the volume change caused by the sulfur phase transition (She, Z.W. et al., 2013).

The research regarding lithium-sulfur batteries nowadays is particularly focused on the development of a cathodic material able to gather excellent properties of electronic conductivity and chemical affinity with sulfur and sulfides, without affecting the electrochemical performances.

1.1.2 Lithium-Air Batteries

A full working and reliable Li-O_2 battery would be a real game changer on the market thanks to the practically unlimited availability of the cathode active material, which it's not stored inside in the charged state. The theoretical specific energy of a lithium-air cell is 3,500 Wh/kg, even higher than Li-S system and, if the oxygen weight is not considered, the power density rises above 10,000 Wh/kg.

The working principle is based on the reaction on the cathode, also called air electrode, of oxygen reduction (ORR) and evolution (OER) during, respectively, discharging and charging. At present, Li-O_2 batteries are developed mainly on two technologies, with a protic (or aqueous) electrolyte or with an aprotic (organic) electrolyte, characterized by different reactions and issues.

For systems containing aqueous electrolytes, the reaction equation will be:

$$4Li + 2H_2O + O_2 \underset{OER}{\overset{ORR}{\rightleftarrows}} 4LiOH$$

resulting in the formation of lithium hydroxide.

In organic (non-aqueous) electrolytes can take place different reaction with different products: a lithium peroxide:

$$2Li + O_2 \underset{OER}{\overset{ORR}{\rightleftarrows}} Li_2O_2$$

a lithium oxide:

$$4Li + O_2 \underset{OER}{\overset{ORR}{\rightleftarrows}} 2Li_2O$$

or a lithium superoxide, that is a competing reaction to the peroxide:

$$Li + O_2 \underset{OER}{\overset{ORR}{\rightleftarrows}} LiO_2$$

During discharge, Li_2O_2 can further react and turn into Li_2O, while two LiO_2 can react with each other to form oxygen and the peroxide; both reactions depend on the intensity of the current, the useful life of the species and the composition of the electrolyte. The formation of the oxide is essentially irreversible, so is crucial the control of all the parameters to ensure the cell the ability to recharge and maintain a high cycle efficiency, given by the ratio of rates of the two reactions forming Li_2O_2 and Li_2O (Aurbach, D. et al., 2016).

The real capacity of the cell is the amount of reduction products effectively stored in the pores, that will always be a reduced percentage of the total pore volume, which determines the theoretical capacity of the cathode. Regardless of which reactions occur, the discharge products will progressively fill up and accumulate inside the pores which are accessible to oxygen until clogging, that can stops the process beforehand. Li_2O_2 will fill the cathode starting from micropores, so a hierarchically ordered porous structure facilitates the process avoiding the obstruction of the pores and so a more correct exploitation of the available internal surface of the cathode (Wang, J. et al., 2013). Electrodes containing at the same time micro and mesopores, called biporous electrodes, can store amounts of Li_2O_2 larger than materials with only one pore size, because large pores facilitate O_2 diffusion, small pores provide a large quantity of reactive sites accelerate the nucleation, thanks to the huge number of surface defects (Xiao, J. et al, 2011). Moreover, a biporous structure, better if hierarchically ordered, increasing the accessibility and the diffusion of oxygen and lithium ions in the electrode, enhances the rate of reactions and the efficiency of the cell. Furthermore, there is a direct correlation between the discharge capacity and the volume of pores in the mesopores range (2-50 nm) (Zheng, J. et al., 2011).

The incomplete superficial coverage problem afflicts also the catalyst loading on the inner surface of the material. A proper deposition and acceptable distribution of the catalyst can improve considerably the performances. The presence of the catalysts not only reduces the ORR and OER rates, hence reducing the overpotential between the electrodes, but is also essential to give priority to peroxide over the other two species, affecting besides its the crystallization phase (Song, M.K. et al., 2011).

Unlike Li-S batteries, in this technology electrolytes have a more fundamental and critical role. Due to the extreme reactivity between lithium and water, it is not conceivable a direct use of an aqueous electrolyte on the anode surface, unless the electrode is well protected. One solution is to switch to a completely solid electrolyte or use a device with two electrolytes separated to avoid the mixing, one non-aqueous, interfaced to the anode and one aqueous in contact with the air electrode. (Grande, L. et al., 2015). The ORR in a protic solvent is based on a three-phase interaction: Oxygen (gas) combines with electrons from the electrode or the catalyst (solid) and the product, LiOH, is dissolved in the aqueous solution, even if with a limited solubility (Padbury, R. & Zhang, X., 2011). The more triphase regions, where the three reactants coexist, are available, the more peroxide will form, with a higher capacity delivered from the cell. Oxygen solubility depends on the nature and composition of the electrolyte, and, greater the solubility, higher the concentration of the gas available for the reduction reaction, that implies an increased specific capacity of the battery (Shao, Y. et al., 2013).

The complexity and the issues related to the aqueous electrolytes pushed to prefer organic solvents, which wet better the pore wall of the electrode, filling the entire pore volume (Li, Y. et al., 2016). In a non-aqueous electrolyte there is a two-phase interaction, where lithium ions and oxygen are in the liquid phase, with the latter that combines with electrons from the solid carbon/catalyst. Unlike LiOH in aqueous electrolytes, Li_2O and Li_2O_2 are not soluble in organic solvents, forming a thin layer on the electrode internal surface. This reduction products arrangement is advantageous because Li_2O_2 can be easily oxidized and dissociated into the original reagents through the OER, determining the ability to recharge of lithium-oxygen batteries containing a non-aqueous electrolyte.

Air cathode of lithium-air batteries consists of a current collector layer, a catalyst layer and an oxygen diffusion membrane. Carbon materials have an excellent electrical conductivity, can promote oxygen adsorption and, thanks to their large superficial extension, porosity and presence of defect sites on the surface, can have a catalytic activity during discharge due to the reducing nature of carbon. The most commonly used material is activated carbon, but a lot of different new materials, like graphene, CNT, nano-fibers, nano-ribbons have been used, achieving good performances even without the addition of a catalyst (Dai, L. et al., 2015). However, although the excellent ability of delivery electrons during discharge, carbon could react with Li_2O_2 and form Li_2CO_3 which can't be oxidized during charge, affecting the capacity. To avoid the carbonate precipitation non–carbon materials can be used, like precious metals, metal oxides or transition metals, which own a good electrochemical stability, but they would decrease the practical specific energy due their mass (Wang, Z.-L. et al., 2013).

Li-air batteries, in absence of a catalyst, have an energy efficiency lower that Li-ion batteries, due to
the large potential gap between charging and discharging, usually about 2.7 V during discharge and 4.2 V during charge. This high charge voltage affects the cycle life, because causes the decomposition of electrolyte and electrode. Therefore, the development of a stable, high-performing and low-cost bicatalyst, able to lower the required energy for both ORR and OER, is essential. Precious metals, like Au and Pt, have an excellent catalytic activity, but they are too heavy and expensive to be integrated in a cell. Metal oxides, like RuO_2, MnO_2, Co_3O_4, Fe_3O_4, provide a good compromise between cost, mass and performances (Xin, S. et al., 2016).

Laboratory Li-air prototypes are tested using only pure oxygen, that maximizes efficiency and performances, but it is a configuration far from reproduce an effective real use, because ambient air has a less concentration of O_2 and is composed of gaseous species different from oxygen that need to be blocked. The air electrode requires a selective semipermeable membrane to avoid undesired reactions caused by the entrance mainly of humidity, resulting in the formation of LiOH, undesired in organic solvents, and carbon dioxide, which causes the precipitation of Li_2CO_3. The concentration of atmospheric oxygen and its diffusion trough the membrane lower the cell efficiency. Semipermeable membranes are mostly realized with Teflon as main component or as coating on a porous structure. (Wang, J. et al., 2013)

Lithium-oxygen batteries don't need to be necessarily related to gaseous oxygen. Li and colleagues have developed, in 2016, a cathode consisting of nanoscale amorphous lithia confined in nanoporous cobalt oxide, enabling only solid-phase transitions between Li_2O, Li_2O_2 and LiO_2 without any gas evolution. This cathode, completely sealed, condition that makes the system more similar to a lithium-ion battery, excludes the drastic volume change due to the phase transition between O_2 gas and O_{x-} in the condensed phase during charge/discharge (10^{-4} difference in specific volume), reduces overpotential loss, improving cyclability and safety (Zhu, Z. et al., 2016).

There are still a lot of limiting factor affecting lithium-air batteries that hinder their full development, for this reason the research is focused on all the components of the battery: cathode materials and design (Williford, R.E. & Zhang, J.G., 2009), bifunctional ORR/OER catalysts, electrolyte composition and additives, especially solid-state, separator and semipermeable membrane.

State-of-the-art batteries have a real specific capacity lower than the theoretical because of a low chemical efficiency of the reactions, lower diffusion rate of the species and the presence of current collectors and packaging. The actual capacity approaches utmost 700 Wh/kg for Li-S and 1700 Wh/kg for Li-O_2, still higher than the best performing Li-ion batteries, around 300 Wh/kg (fig. 1.2). This fact is due to the lower atomic weight of the cathodic materials and, most of all, because discharge insulating products (Li_2S, Li_2O_2, LiOH) can store more lithium ions per unit mass than commercial Li-ion cathodes. A higher capacity allows the devices to last longer in terms of use, which means, for secondary battery, a less frequently necessity to be recharged, thus an increase in the working life of the device (Bruce et al., 2012).

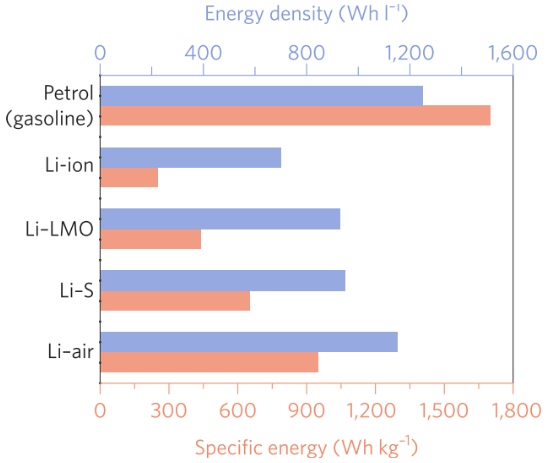

Figure 1.2: Performances comparison between fossil fuel and different kind of state-of-the-art batteries (*Adapted from Lin, D. et al., 2017*)

These new generation batteries, based on different cathode active materials, share the same negative electrode, the lithium metal anode, which is the key factor to ensure excellent performances. However, despite the benefits, this kind of negative electrode is affected by severe problems to address, to provide indispensable safety and reliability to the device.

1.2. Goal and innovation of this work

As will be later discussed, lithium metal anode problems have been coped in different ways, but there is scarcely discussed in the literature the use of reduced graphene oxide aerogels in combination with metallic lithium. The main aim of this work was to find a suitable way to employ for RGO as protective material for the metallic negative electrode. Carbon-based solution for dendrite growth suppression and RGO aerogels applications in batteries, were inspiring and influencing for the development of this work.

The first goal is to define the working parameters for the microwave-assisted reaction with or without ascorbic acid, because there is a lack in the literature about using vitamin C as reducing agent during high pressure-high temperature self-assembly of graphene oxide, so the only starting point is the conventional hydrothermal reaction. The resulting material is then characterized to understand the microwaves effect on its chemistry and the morphology.

The other purpose of this work is to design an easy and fast productive process to realize the free-standing membrane using the material produced, instead of starting from graphene oxide like in the literature, conceiving a feasible procedure to introduce it inside a coin cell, to test its protective activity and to evaluate the possible consequences on the performances.

This work is part of a cooperation between DISAT department of the Politecnico of Torino and the “Battery500” group of IBM- Almaden Research Center. There is a solid knowledge at Politecnico about hydrothermal synthesis of reduced graphene oxide aerogels and its composites, which are the base for a wide range of researches about various topics, including energy storage devices. Research on batteries at IBM, with its established tradition and deep know-how in the energy storage field, is mainly focused on new generation devices, especially lithium-oxygen and lithium sulfur batteries.

1.3. Thesis content

This section is useful to provide the reader a general overlook on how the thesis is structured in order to fully understand the work.

After an introductory chapter to locate the topic in the field of new generation batteries, in chapter 2 the properties of the lithium metal anodes are discussed: which advantages introduces, how improves the cell performances and which problems do afflict it. It will be also summarized the state of the art in terms of anode protection.

In chapter 3 the properties and characteristic features of reduced graphene oxide will be discussed, especially in the form of aerogel, and its application in the battery field. Moreover, RGO aerogel synthesis techniques will be presented, with particular attention to the employed techniques.

In chapter 4 are explained the experimental setups to produce the materials and fabricate the samples to be analyzed with physico-chemical characterization techniques. The results of the analysis are then interpreted and discussed.

In chapter 5 are described the fabrication process of the membrane and the assembly sequence of the test coin-cells, with a further discussion on the results obtained from the electrochemical tests performed on them.

The last chapter is dedicated to a brief recap of the overall work, from which are derived the conclusions, followed by ideas and thoughts for possible studies and future researches.

2. Lithium metal anode

2.1. Properties and advantages

Lithium is an alkali metals, and it is the lightest and most electropositive of all the metallic elements, with about half density of water. It is soft, flexible, malleable and can be readily extruded into thin foils; just cut or newly produced has the same color and shine of bright silver but it is quickly covered by a native oxide layer and, in presence of humidity, it tarnishes quickly. Lithium is an appealing material as secondary (rechargeable) batteries anode thanks to its light weight, good conductivity, high electrode potential and very high electrochemical equivalency (tab 2.1). These last two features are essential requirement to ensure high specific energy (or energy density), making the lithium, theoretically, the ideal electrode material for high-performances batteries, the so called lithium-metal batteries (LMB) (Reddy T. B., 2014).

Table 2.1: Physical properties of Lithium (*Adapted from Reddy, T.B., 2014; Zoski, C., 2011*)

Melting point	180°C
Boiling point	1347°C
Density	0.534 g/cm^3 (25°C)
Specific resistance	9.35×10^6 Ω·cm (25°C)
Electrode potential	–3.045 V (SHE)
Electrochemical equivalency	3862 mAh/g

Several metals have been considered as candidate for metal-anode batteries: zinc is the most stable electropositive element in aqueous electrolytes without undergoing to considerable corrosion, for this reason was the first to gain attention, especially for primary zinc/air batteries for small application requiring low-rate discharge for long periods. Other metals are attractive because of their abundancy and theoretical specific energies, like aluminum, calcium and magnesium, but are affected by a parasitic corrosion that causes instability and safety issues in rechargeable devices. Iron, cadmium and lead have been also studies, because traditional elements in rechargeable batteries, but their low electrochemical properties discourage their use. Lithium is an outstanding electrode material, if compared with the other metals used in metal-anode batteries, among which has the highest theoretical specific capacity, that ensures the best theoretical gravimetric energy density. Li is preferred to other alkali metals because its more easily handled, thanks to its lower reactivity, better ductility, workability and mechanical properties, and its preferred to the other metallic negatives, especially transition metals, because it is lighter and with higher operating voltages (tab 2.2).

The theoretical specific energy can be determined with the metal electrochemical equivalence or on the base of the overall cell reaction, comprehensive only of the active components of the electrodes (Table 2.3). In metal-air systems the oxygen is not stored inside the cell, for this reason the energy density can be calculated only considering the anode capacity alone. The reaction-related energy is calculated on the practical voltage of the cell, lower than the theoretical value, because some metal-oxygen pairs have a very small practical voltage (Al and Mg), making them not suitable for a feasible real application. Despite this assumption on the calculations, the electrochemical values for LMBs are higher than the performances ensured by commercial lithium-ion technologies (Claus, D., 2011).

Table 2.2: Comparison of physical characteristics for Anode Materials (*Adapted from Claus, D., 2011*)

Material	Molar mass, g/mol	Density, g/cm^3	Melting point, °C	Valence change	Standard potential at 25°C, V	Electrochemical equivalence	
						mAh/g	mAh/cm^3
Li	6.94	0.53	180	1	–3.045	3862	2047
Na	23.0	0.97	98	1	–2.714	1166	1131
Mg	24.3	1.74	650	2	–2.356	2205	3837
Al	26.9	2.70	659	3	–1.676	2980	8046
Ca	40.1	1.54	851	2	–2.840	1337	2059
Fe	55.8	7.85	1528	2	–0.440	960	7536
Zn	65.4	7.10	419	2	–0.763	820	5822
Cd	112.0	8.65	321	2	–0.403	480	4100
Pb	207.0	11.30	327	2	–0.125	260	2900

Li-ion batteries (LIBs) are constituted by two electrodes, usually a transition metal oxide as cathode and a carbon material as negative electrode, which incorporate lithium in their crystalline structure through an intercalation process, a reaction where the ions are reversibly removed and inserted in the framework, without inducing significant structural alterations or changes to the host. Electrode materials mainly have a graphite-like structure, determining a layered storage of the ions. Li insertion and extraction may cause a volume change that induces the loss of electric connectivity between the host particles, which increases the internal resistance, and a stress in the electrode, resulting in a mechanical damage. Lithium is commonly contained on the positive side, but the anode can be lithiated to have a battery in the charged state. The theoretical gravimetric specific capacity of metallic lithium is ten times higher than Li_nC_6 ($0 \leq n \leq 1$), the typical Li-ion anode (372 mAh/g), while the volumetric comparison is still favorable for Li metal (2062 mAh/cm^3 compared to 837 mAh/cm^3 for LiC_6), but the lithium low density makes the advantage not so great. This convenience is induced by the absence of an insertion compound, that determines a quicker movement of the lithium ions back and forth from the negative side. As said in the introduction, rate of diffusion in Li-S and Li-O_2 is a fundamental feature to guarantee high performances to the systems (Claus, D., 2011).

Table 2.3: Electrochemical parameters for metal-anode batteries (*Adapted from Claus, D., 2011, Adelhelm, P. et al., 2015*)

Reaction	Metal specific capacity, mAh/g	Theoretical voltage, V	Practical voltage, V	Specific energy based on metal, Wh/kg	Specific energy based on reaction, Wh/kg
Non-aqueous electrolytes					
$Li + ¼\ O_2 \rightarrow ½\ Li_2O$	3862	2.91	2.80	10813	5023
$Li + ½\ O_2 \rightarrow ½\ Li_2O_2$	3862	3.10	3.00	11586	3505
$Li + 1/16\ S_8 \rightarrow ½\ Li_2S$	3862	2.50	2.00	7724	2567
$Na + ¼\ O_2 \rightarrow ½\ Na_2O$	1166	1.95	1.95	2274	1687
$Na + ½\ O_2 \rightarrow ½\ Na_2O_2$	1166	2.33	2.33	2717	1602
$Na + O_2 \rightarrow NaO_2$	1166	2.37	2.27	2643	1105

Table 2.3: Electrochemical parameters for metal-anode batteries (*Adapted from Claus, D., 2011, Adelhelm, P. et al., 2015*) (continued)

Reaction	Metal specific capacity, mAh/g	Theoretical voltage, V	Practical voltage, V	Specific energy based on metal, Wh/kg	Specific energy based on reaction, Wh/kg
Aqueous electrolytes					
Li + ¼ O_2 + ½ H_2O → LiOH	3862	3.45	3.00	11586	3359
Na + ¼ O_2 + ½ H_2O → NaOH	1166	2.77	1.27	1486	1281
Zn + ½ O_2 → ZnO	820	1.65	1.10	902	725
Al + ¾ O_2 + 1½ H_2O → $Al(OH)_3$	2980	2.71	1.30	3874	1340
Mg + ½ O_2 + H_2O → $Mg(OH)_2$	2205	2.93	1.30	2867	1195
Fe + ½ O_2 + H_2O → $Fe(OH)_2$	960	1.30	1.00	960	597
Ca+ ½ O_2 + H_2O → $Ca(OH)_2$	1337	3.12	2.00	2675	1447

The processes on the metallic lithium electrode are simple: under discharge stripping takes place, that is an anodic dissolution with the formation of Li^+ ions from the oxidation of metal atoms, followed, during discharging, by an electrolytic cathodic deposition on the metallic surface, called plating, meaning a faster exchange without the need of a solid-state diffusion to locate the lithium in the interstices imposed by the intercalation. Thanks to its conductivity, lithium can be used not only as active material, but also as electronic conductor, directly placed on the current collector, made of stainless steel or copper, the latter for better performances.

2.2. *Disadvantages and problems*

Despite the exceptional and suitable properties, it has not been realized yet a rechargeable battery based on a metallic anode with acceptable characteristics because they are affected by critical issues.

Lithium, in particular, is less safe than other metal anodes materials, excluding other alkali metals, because extremely reactive with a lot of gases normally present in the air, like humidity, O_2 or CO_2. Lithium reacts vigorously with water:

$$2\,\mathrm{Li} + 2\mathrm{H_2O} \rightarrow 2\,\mathrm{LiOH} + \mathrm{H_2}$$

This reaction is different from the one that is supposed to takes place in protic solvents, but both produce hydroxide that is undesired either in aqueous and anhydrous electrolytes if it’s formed on the surface of the anode, where constitutes and insulating film, requiring the metal protection from the electrolyte and the handling of the battery in dry atmosphere. The heat generated by this reaction may ignite the released hydrogen, causing the lithium also to burn, that is a very hazardous situation to prevent whereas lithium has a low melting point. this is the most important among the factors affecting safety of Li-metal batteries not directly related to the operative life of the device. This reaction is not only due to humidity but it is also related to a parasitic corrosion reaction, or self-discharge, that is rapid and affects the coulombic efficiency, causing a capacity drop because consumes lithium. The gradual degradation of the metal can be aroused by ingress in the cell, or the crossover from the air electrode, of oxygen and carbon dioxide that, like water, cause a depletion of the active material and the formation of a passivation layer, made of insulating species, on the surface of the anode which increases the internal resistance of the cell. These side-reactions make rechargeable metal-anode batteries more problematic to operate in open-air environments.

Both Li metal and lithiated graphite electrodes in non-aqueous solutions are covered by a very similar surface film, which controls their electrochemical behavior. Most organic solvents are unstable in the presence of Li metal and are reduced at the surface because is chemically very active (reduction potential of organic solvent is below 1.0 V vs. Li + /Li electrode), so when it is coupled with an aprotic electrolyte takes place a carbonation, a decomposition of the electrolyte that results in the crystallization of a carbonate on the surface (Aurbach, D. et al., 2002). This insoluble thin film, made of Li_2CO_3 as main product of degradation of the solvents, lithium salts, additives and the impurities present in the electrolyte precipitated on the surface, damages the electrode, decreasing its performances, but it is a protective layer which separates the anode from electrolyte, preventing further reaction. This film is called solid electrolyte interphase (SEI) (fig. 2.1a), according to the model proposed by Peled in 1979. Every alkali and alkaline earth metals are always covered by a surface layer at least 2 nm thick, so there is never a direct and free contact between the metal and the solvent (Peled, E. 1979). SEI is a lithium-ion conductor and electronic insulator film, with a disordered structure characterized by the typical crystal lattice defects, like vacancies, and grain boundaries that promote the ionic conduction. As stated by the compact-stratified-layer (CSL) model, the interphase is made of two stacked layers: the bottom one, on the electrode surface, is the SEI, thin and compact, the second one more porous on top is either still the SEI or a polymer electrolyte interphase (PEI), in which the lithium in the electrolyte is covered by a film composed by products of degradation and reduction-induced polymerization of the solvent. Peled, in 1997, proposed another and more advanced model, called the mosaic model (fig 2.1b), stating that the insulating layer on both lithium and carbonaceous electrodes consists of a mixture of many different reaction products formed simultaneously which precipitate on the surface as a mosaic of microphases, each one with its own resistance, depending on the constituting species. The mosaic morphology determines an additional grain-boundary electronic resistance due to the wide extent of the area of separation between the phases, allowing otherwise Li ion to migrate easily.

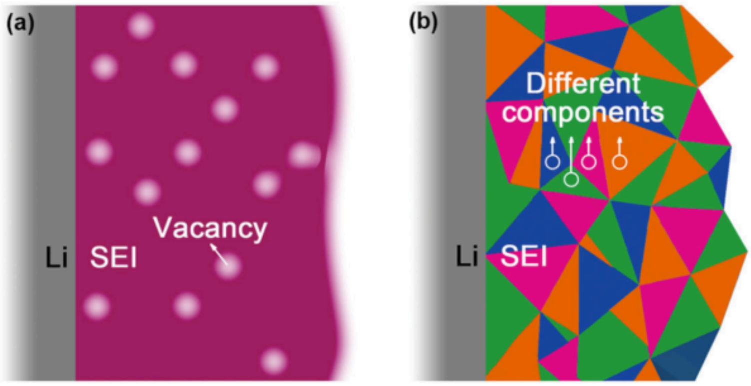

Figure 2.1*:* Schematics of proposed SEI models a) Peled’s model b) Mosaic model *(Adapted from Cheng, X. et al., 2015)*

SEI grows until it is thick enough to block electron transfer, its chemical composition and morphology are complex and heterogeneous, change over the time with a gradual variation from the interface of Li/SEI to the interface of SEI/solution and depend on the specific electrolyte composition and additives. However, the formation of this interphase, depending on electrode real surface area, internal current density and cell voltage, results in irreversible capacity loss with benefits in terms of storage and discharge because of its long-term stability

(Claus, D., 2011). All electrode materials undergo volume change during operation. Given the Li metal hostless nature, the non-use of intercalation results in virtually infinite cycle volumetric variation; this huge volume change requires the SEI layer with high elastic modulus.

During the lithium extraction, the anode surface shape changes continuously breaking the overlying protective layer, under which new fresh metal will be exposed every cycle to the electrolyte to form almost instantaneously more self-remedying film (less than 1ms) (Odziemkowski, M. & Irish, D.E., 1993), with a lithium consumption in a breakdown and repair process of the SEI during cycling. Under charging, the lithium plates on the surface, sometimes assuming a fiber-like shape. When the cell charges, these fibers can be cut and isolated by the surrounding SEI that wraps them. In the next discharge phase these isolated pieces, called dead lithium, will be embedded in the surface during lithium replating, resulting in an electrochemically inactive but chemically active material accumulated during charging that will reduce the electrode capacity and conductivity. The dendritic growth and amassing of dead lithium on the anode leads to a significant increase of the surface area every cycle, inducing an enhanced reactivity which degrades the stability of the system, resulting in an intensified sensitivity of the cell to cycling as it is cycled.

A low current density which induces whiskers-like dendrite structure, that has a higher tendency to be cut, when high discharge currents form thicker dendrites, harder to be broken. Dendrites formation is primary failure mechanism in lithium metal rechargeable batteries, because their growth (fig. 2.2) will eventually result in puncture of the separator that causing short circuit between the two electrodes, leading catastrophic failure of the system because, instead of an ionic conductivity, there is an electronic conductivity, which poses a serious safety hazard due to the extremely high current density. The plating of lithium under can result in three different morphologies: mossy, granular and dendritic. Mossy lithium is formed when the deposition current is small and provides a high cycling efficiency.

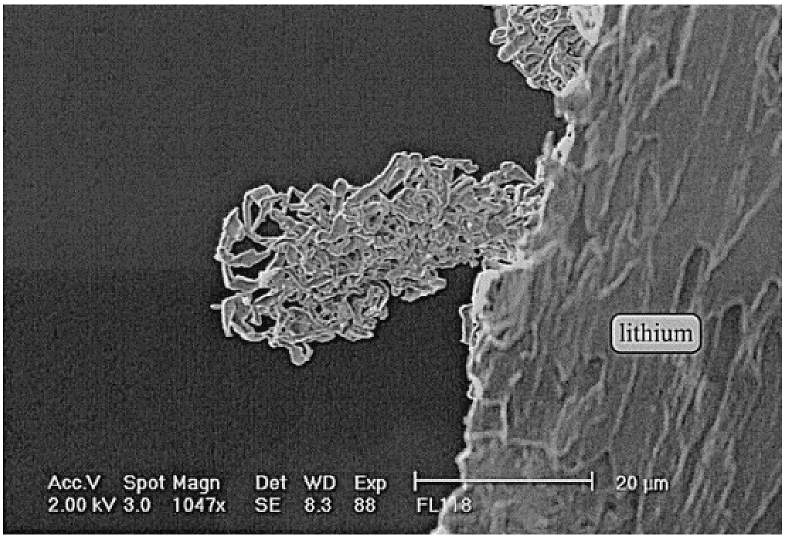

Figure 2.2: SEM image of a lithium dendrite grown on the surface of a lithium anode (*from Orsini, F. et al., 1998*)

In figure 2.3 are illustrated the phenomena happening at the surface of the electrode. When the thickness of the SEI is enough to prevent electronic tunneling or when the voltage is smaller than that for dielectric breakdown, the current stop flowing through the film and lithium starts depositing on the anode under the SEI, getting through without damaging it. The accumulation initiates in the areas where the top layer has a higher lithium-ion conductivity, for example the pits caused by the ions extraction, metal imperfections, grain boundaries and crystalline defects, like kinks and corners. This happens because the SEI has an uneven morphology and inhomogeneous chemical composition. This irregular deposition causes a mechanical stress under the interface that, being stiffer, induces a deformation in the lithium to release the stress. The localized stress will break the rigid and frail top film, letting lithium treelike deposits grow through these broken holes. If the current is small, the stress will not be intense enough to break the film, leading to an amorphous morphology. If the current is high, the deposition continues and on the metallic surface, causing the growth of more dendrites. When there is a huge number of fibers on the surface, the lithium begins to be deposited on the tip of those, which is the area containing most the defects on the dendrite. The deposition on these defects produces a particle-like morphology, because of the current density is lower due to the increase of the surface of the tip. During discharge the reverse process take place, with dissolution that starts at the apex of the dendrite, that can be cut at the bottom, with a higher probability of becoming dead lithium with smaller diameter of the fibers (Yoshimatsu, I., 1988; Arakawa, M. et al., 1993).

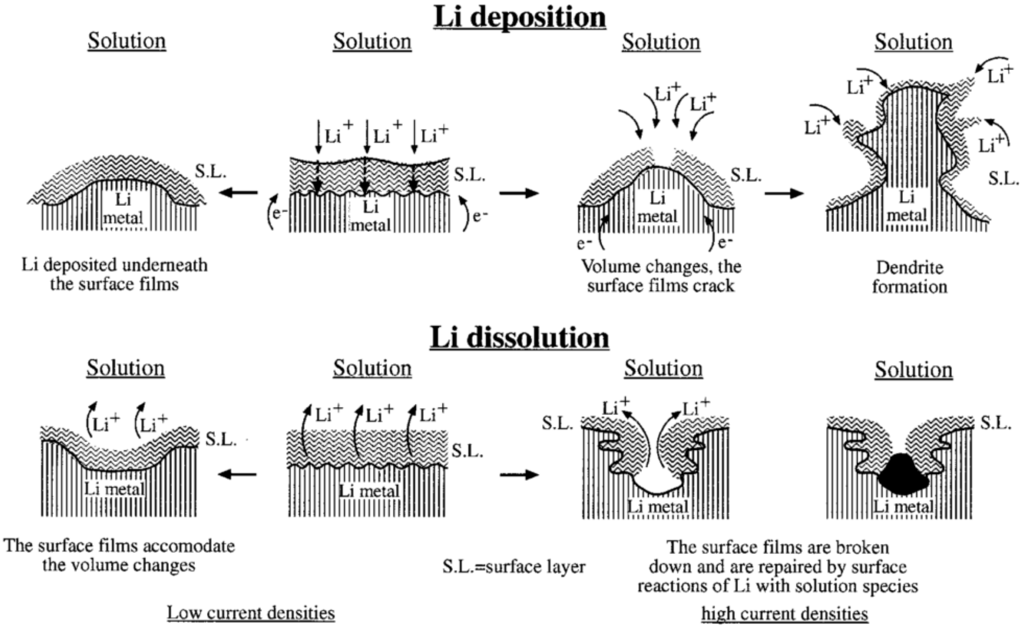

Figure 2.3: Morphological phenomena developed on the anode during lithium dissolution and deposition (*Adapted from Cohen, Y.S. et al., 2000*)

Monroe e Newman in 2003 analytically modeled the dendrite formation in a parallel-electrode PEO/LiTFSI system, showing that that dendrites growth accelerates both as time passes and as it moves across the cell, and it is slowed by lowering the current density, determining an increase in the charge that can be passed before failure, and by an increased potential difference between the dendrite tip and base. The cell fails if run above 75% of the limiting current, that increases if increased the inter-electrode distance. Even if surface energy is a determinant aspect in the dendrite growth kinetics, it has been demonstrated that a stiffer SEI doesn't slow the dendrite propagation, so it isn't possible suppress the growth by modifying the surface forces. (Monroe and Newman, 2003).

The aforementioned problems cause a low cycling efficiency of lithium anodes, which is strongly affected by the morphology of the electrode surface. It is impossible to obtain 100% lithium cycling efficiency, there an excess of metal may be required to ensure to the system reasonable performances and cycle life. The system needs an overabundance on lithium than the stoichiometric amount for the reaction to compensate for the inefficiency of the stripping and plating process. Assuming a simple model for a non-aqueous Li-O_2 cell with a cathode composed only of Li_2O_2, introducing in the system a threefold excess of metal to compensate the loss on cycling, the specific energy is reduced from 3505 Wh/kg to 1800 Wh/kg, while a system containing Li_2O in the cathode has its energy decreased from 5023 Wh/kg to 2200 Wh/kg. On the other hand, the size of the cell and the amount of active material are directly related to the safety: small batteries using less lithium have a lower total energy, are safer than larger ones of the same design and with identical chemistry (Bruce, G. et al., 2011).

Diffusion of oxygen and sulfur through the electrolyte to the electrode surface is a slow process, thus limiting the rate of the coupled reaction. For this reason, in addition to the problems mentioned above (fig 2.4), metal-anodes batteries, especially with air cathodes, have a power limitation compared to state-of-the-art Li-ion batteries. The slow diffusion rate due to the low solubility of the species, the presence of insulating reduction products and thick passivating film growing on both electrodes limit the useful power generated from the cell.

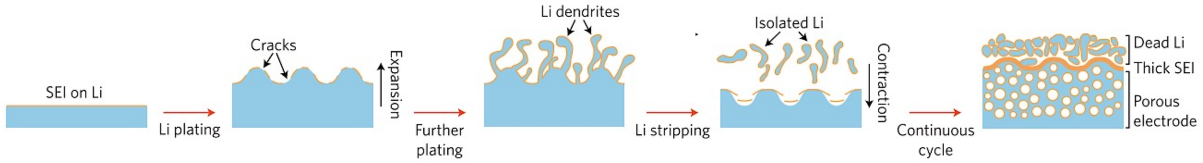

Figure 2.4: Schematic summary of metallic anode issues related to lithium stripping and plating (*Adapted from Lin, D. et al., 2017*)

2.3. State of the art in dendrites suppression

Lithium alloys have been proposed as alternative anode materials: Scrosati's group developed a Li-ion/air hybrid battery with a lithiated silicon-carbon composite anode, exhibiting a very high fully reversible capacity (Hassoun, J. et al., 2012). Those electrodes exhibit good properties in small flat design coin cells, but it is difficult to scale them up to be implemented in to cylindrical cells, because they are brittle and cannot be extruded into thin foils, so is impossible to produce the spirally wound anode require in cylindrical batteries. Lithium metal anode is fundamental in terms of design and performances, so the improvement of its cycling efficiency is essential to achieve in order to be implemented if full working devices. This amelioration can be accomplished with a proper protection of the surface. From Monroe and Newman's results about the effect of the external pressure on the electrodeposition kinetics it can be deducted that there is a positive effect of the stacking pressure on the inhibition of dendrite formation, which produces a longer cycle life in a cell housed tightly. Lithium deposited in a cell under a pressure over its yield strength is physically confined on the anode surface, giving a densely-packed morphology, which reduces the amount of lithium isolated from the substrate (Monroe, C. & Newman, J., 2004).

To enhance the cycle stability, changes can be made either in the electrolyte or on the anode. Every organic solvent has its own effect on the cycle efficiency, stability and capacity retention because they produce different constituents of the SEI (Xu, K. et al., 2014). The more straightforward solution is to form a more stable and solid SEI to mechanically suppress the dendrite growth without affecting its electrochemical properties. Electrolyte decomposition products are the dominant components of SEI, so it can be engineered to meet the need of stabilization by modifying its composition, introducing lithium salts to affect the surface chemistry and purposely form a more robust protecting layer, to prevent further reactions. Li halides are chemically stable and compatible with metal and solvent. For example, a $LiPF_6$ salt, dissolved in DME, has high chemical stability than the commercial LiTFSI, providing better efficiency and cyclability, thanks to the synergic effect of salt and solvent that follows the CSL model. Binary Li salts were also proposed. The formation of dendrites is induced by the Li^+ shortage in the vicinity of the negative electrode, so salt concentration also has a fundamental role in the Li-ion transport, with a higher concentration that increases the Li dissolution/deposition rate but leads in a rapid formation of a compact SEI. Ultrahigh concentration salt electrolytes are particularly effective in Li-S batteries to inhibit lithium polysulfides dissolution stopping the shuttle phenomenon and so avoiding their precipitation on the anode surface (Cheng, X.B. et al., 2015).

The electrolyte composition can be adjusted introducing in the formulation functional additives with higher reduction voltages than solvents and salts aimed to control the SEI composition and morphology. Halides enhance the layer stability and lower the diffusion resistance inducing a decrease in the activation energy of crossing and deposition of the Li ions. The halogens, especially fluorinated species, have an inhibitive effect on polysulfides shuttle without any cathodic confinement, forming a protective layer with sulfur-based molecules on the anode surface that suppress further reactions, but they modify the SEI properties alone too. The stability of the metallic electrode strengthened by a saturation of CO_2 in the solvent, despite its reactivity with lithium ions, which forms with SO_2 a robust protective layer, but this beneficial effect takes place only in a narrow concentration window, so it is a mechanism to not consider in Li-air batteries. $LiNO_3$ was patented as cycle-life extending additive in Li-S batteries, thanks to their synergistic effect with polysulfides (Cheng, X.B. et al., 2015). Introducing halogenated salts containing Cs^+, Rb^+ and Na^+ ions in an organic solvent can fundamentally alter the dendrite formation. These metal cations, with an effective reduction potential below that of Li^+ according to the Nernst equation are employed in a self-healing mechanism, where a positively charged electrostatic shield will form around the initial tip, negatively charged, of a rising dendrite, repelling incoming Li^+ and homogenizing their flux, without being physically attached to the surface. The growth of the protuberance is stopped, eliminating any inhomogeneity on the surface because forces the lithium plating on the areas around, that leaves an even and isotropic dendrite-free smooth deposition without a permanent film on it (Ding, F. et al., 2013).

Variation on the anode can be made in several ways. It is possible to stabilize by interface engineering, for instance introducing on the surface an “artificial” structure to replace or stabilize the native SEI with an *ex-situ* tailored layer with specific properties. For example, exposing Li metal to tetraethoxysilane leads to the formation of a silica film on Li metal, but it was studied also a Li_3N layer exposing the electrode to nitrogen and an ALD coating of Al_2O_3. It is acknowledged that introducing a highly rigid electrolyte, with an elastic modulus, and consequently a shear modulus, about twice that of the Li anode (1GPa), a smooth electrode surface is kept each cycle, achieving a mechanical suppression of the dendrite formation. However, a trade-off exists between modulus and surface adhesion with the anode because high-modulus films have poor adhesion on metal Li, determining high interfacial resistance during cycling. The stiffness of the solid electrolyte avoids the amplification of surface roughness by the lithium plating because produces a pressure that compress the metal (Monroe, C. & Newman, J., 2004; 2005). Cui’s group created a monolayer of nanostructured and interconnected amorphous hollow carbon nanospheres that helps to ensure uniform lithium metal deposition and facilitates the formation of a stable SEI without dendrites formation for more than 150 cycles up to a current density of 1 mA/cm^2. The amorphous carbon is chemically stable in the reducing environment, it is flexible but at the same time mechanically strong, can control the flow of Li ions without increasing the impedance, and is weakly bound to the metal current collector, moving freely up and down to adjust the availability of empty space while the deposition takes place underneath, guaranteeing high lithiation capacity. Cui's group also proposed a two-dimensional atomic crystal interfacial layer made of hexagonal boron nitride or graphene, where the lithium is between this layer and the substrate only after electrochemical deposition, during which ions are able to penetrate through the point and line defects, providing a smooth surface. The layers afford chemical inertness as well as mechanical strength, ultrahigh Young's modulus and flexibility. Both nanospheres and 2D layers need to be grown on a Cu substrate, that need to be etched or used as substrate for the plating, making them not reproducible on a large scale (Zheng, G. et al., 2014; Yan, K. et al., 2014). Other kind of artificial interfacial protections have been investigated like LISICON, copolymers, nanoarchitectured hollowed silica nanospheres (Lang, J. et al., 2017).

Artificial SEIs, despite their advantages, are limited by low ionic conductivity, for this reason have been explored a lot of different solid-state electrolytes (SSE), such as polymers, especially functionalized or crosslinked PEO (no interfacial reaction between PEO and fresh Li, solvating properties for Li ion because of complexation by its ether groups), PEO copolymers, lithiated or silanized polymers, gel polymer electrolytes, but also inorganic crystalline materials, like sulfides, oxides, nitrides, phosphates, perovskites, garnets, ceramics containing Ge and glass-ceramics, or organic-inorganic hybrid or composites. SSE allow enhanced process-ability, which is imperative in the production of industrial scale practical LMBs, with the possibility to be embedded in small and micro-scale devices (Xu, W. et al., 2014).

IBM developed a one-particle thick composite membrane (OPTM) made of a Li-ion-conducting ceramic (LICC, Al, Ti and Ta based instead of Ge, fundamental element in most widely used LAGP ceramics) single layer of particles embedded are circumferentially bound by a Li-ion insulating organic polymer (cyclo olefin) such that the top and bottom surfaces of the particles are not covered by the matrix (fig. 2.5). This thin membrane, acting both as separator and SSE, has a high ion-transport ability and allows to join the flexibility of the polymer to the conductivity and the shear modulus of the brittle ceramic, being capable of suppressing dendritic growth by mechanical stress, because the ionic current distribution in the membrane will favor dendrite growth exclusively toward the LICC particles which are able to resist dendrite penetration, while there is no driving force for through the polymer matrix because it is a Li-ion insulator. The fabrication procedure is simple and versatile, does not require extensive particle pretreatment for particle functionalization or postdeposition polymerization or cross- linking. Actually, IBM is working to make the process amenable for large-scale manufacturing, further simplifying steps and tools to save time and making the practice much more cost effective, using smaller particles (<50 μm) (Aetukuri, N.B. et al., 2015).

Electrode design is another parameter that can be changed to obtain an effective cyclability, modifying the current distribution, making it more homogenous. Several structures have been proposed, like Li powder, even coated with halogenated lithium, heterogeneous lithium framework with ceramics or carbon materials, multilayered lithium intercalated with graphene, fibrous Li-salt 3D matrixes. An increased electrode effective surface area reduces the anode current density, leading to a prolonged dendrite initiation time and a decreasing in the growth rate (Lang, J. et al., 2017).

The anode can be patterned with a modified current collector with an engineered surface or a 3D structure, through which is possible minimize the volume change by using chemically stable and mechanically strong scaffolds to guide Li plating and performing a protection of the surface. On planar substrates, the growth can take place easily and directionally because the nuclei locally enhance the ions flux, with the dendrites that start to dissolve, during charge, from the roots receiving electrons at their base, easily fractured and detached from the substrate to form dead Li. In contrast, a pre-existing conductive framework will accommodate well the deposited Li because of the numerous protuberances act as charge centers and nucleation site, while charging a more isotropic dissolution is induced. These structures provide a larger surface area compared to flat surfaces and the opportunity to recycle dead lithium combined to a good flexibility to sustain the volume fluctuations during cyclic Li stripping/plating. Researchers proposed as current collectors free-standing graphene foams, submicrometric Cu skeleton structure, lithiated glass fibers, 3D oxidized polyacrylonitrile (PAN) nanofiber network, porous carbon and braided CNTs. It’s possible to perform a thermal infusion of lithium in a nanostructure instead of an electrochemical deposition of Li metal, but unfortunately most materials, like polyimides networks, have a poor wettability with molten lithium, so the framework can be covered with a material with a strong affinity with metallic lithium. Si or ZnO coating can react with molten Li and the reaction can drive the liquid metal to wet the surface scaffold to completely fill it. (Lin, D. et al., 2017).

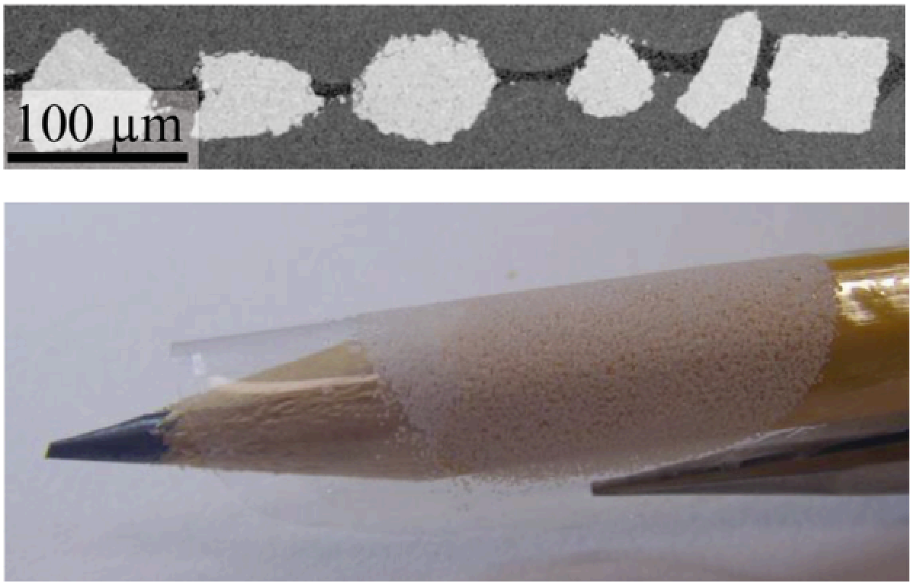

Figure 2.5: Cross-section SEM microscopy image and optical photograph of a typical membrane to show appearance, dimension and flexibility (*Adapted from Aetukuri, N.B. et al., 2015*)

3. Reduced Graphene Oxide Aerogel

3.1. *Properties*

Graphene is two-dimensional allotrope of carbon, in which the atoms are densely packed in a regular sp^2-bonded hexagonal pattern arranged on a single-atom thickness flexible layer. Since its discover in 2004, scientists have been deeply interested in its exceptional physical and chemical properties because of the huge potential in various technological fields, especially electronics and energy storage. Among the different fabrication methods proposed, the top-down synthesis involving the reduction of graphene oxide, which represents a highly defective state of graphene, is promising for the mass production of graphene-based materials, since GO can be synthesized in large quantities and easily reduced by different methods. Oxidized graphene sheets, can be used as building blocks into complex but well-defined three-dimensional macrostructures called aerogels, characterized by defects like vacancies, bond reconstruction and functional groups. The inherent flexibility of graphene is a crucial property for constructing those interconnected porous networks, because the leaflets can bend without rupture to constitute curved structures, where the pore walls are made of stacked sheets connected by physical crosslinks due to the overlapping of π orbitals (Xu, Y. et al., 2010). These frameworks have a high specific surface area, not as extended as graphene theoretical specific surface, 2630 m^2/g, because the effective extension depends on the stacking of the graphene sheets, but is still very high (100-600 m^2/g) and easily accessible. This superficial extension depends on its solid surface and not the inner porosity, which is significant (97-99%) and characterized by pore sizes in the range from less than 2 nanometers, through micropores and mesopores, to several micrometers, sometimes hierarchically ordered (Hu, G. et al., 2016) and occasionally with a bimodal size distribution (Wang, Z.L. et al., 2012). Thanks to these specific attributes, RGO aerogel are extremely lightweight, with density between 2 and 10 mg/cm^3 (fig 3.1). lower than the densities of 3D graphene structures obtained with other techniques (Hu, H. et al., 2013, Zhao, Y. et al., 2012).

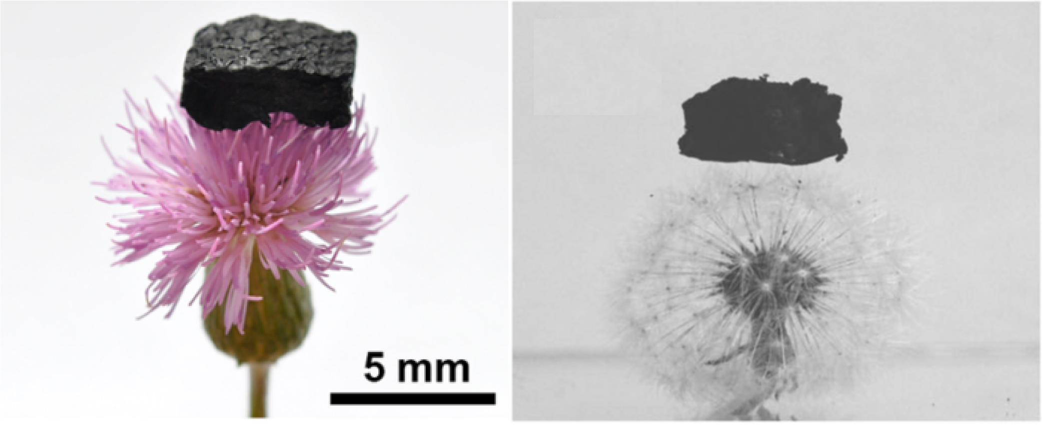

Figure 3.1: RGO aerogels standing on flowers to show their lightness (*Adapted from Cheng X. et al., 2015; Zhao Y. et al., 2012*)

Despite their very low density, these ultralight aerogels are self-standing and self-supported, possess high elasticity, being able to completely recover from strain after more than 90% compression (more effective return with a higher reduction degree), while many carbon-based solids with high porosity (e.g., activated carbons) are brittle and easily collapse under compression, and show excellent resilience and flexibility, thanks to the strong bindings formed by the π-π orbitals stacking sites (Hu, H. et al., 2013). Those aerogels have an elastic and plastic behavior under compression: in the elastic region, the solid pore walls undergo an elastic bending, with the closure of the porosity without rupture of the structure, while in the yield region, the pores gradually collapse when stress exceeds the yield strength. Mechanical property tests indicate that RGO aerogels, without any enhancements, additive or specific modification, are much more mechanically stronger than carbon nanotube aerogels, can support more than 10000 times their own weight, nearly twice of the amount supported by other carbon-based aerogels (Zhang, X. et al., 2011, Sui, Z. et al., 2012), thanks to exceptional mechanical properties of the constituting building blocks. AFM nanoindentation on defect-free graphene yielded a 2D elastic modulus of ~1 TPa, that drops around 0.23 TPa for GO. Planar elastic modulus of reduced GO varies between ~0.82 and ~0.32 TPa, so there is a strong influence of defects on the intrinsic stiffness, graphene sheets with imperfections are more rugged and structurally robust than what was thought (Zandiatashbar, A. et al., 2014).

RGO aerogels are electronic conductors thanks to the restoration of π orbitals conjugated systems, typical of the graphene aromatic ring, from GO upon reduction. The electrical conduction is due to multiple contacts among the agglomerated nanoplatelets, but the subsistence of residual oxygenated groups affect this property, represented by a conductivity between 0.1 and 100 S/m (value strongly dependent on the atomic ratio between carbon and oxygen) which is at least three order of magnitude lower than the basal plane of the graphite (10^5 S/cm), (Xu X. et al., 2010). The presence of sp^2 carbon atoms in the lattice confers also a high thermal conductivity to the framework, that can be both either phononic and electronic. While thermal and electrical transport in graphene is very sensitive to disruptions in the sp2-bonding network, its mechanical properties are less affected by defects and imperfections (Zandiatashbar, A. et al., 2014).

Reduced graphene oxide stands out among the carbon materials thanks to its catalytic property for the oxygen reduction reaction. Pristine carbon materials usually show low catalytic activity for the ORR in non-aqueous solvents, so they act only as catalyst substrate, while nanostructured RGO aerogels serve not only as support, but acts also as good ORR catalyst thanks to many edges, lattice defect sites and functional groups located on the surface that can facilitate some chemical transformations (Wang, Z. et al., 2014). Reduced graphene oxide shows also a good catalysis activity for electrocatalytic splitting of water and oxygen and hydrogen evolution reactions (HER) (Hu, C. and Dai, L., 2016). The presence of functional groups provides opportunities for tailoring the chemical properties of the aerogels. Furthermore, the control of the elements within the functional groups and their distribution on the surface can greatly modify and modulate the electronic structures of graphene sheets, influencing also the physical properties.

Another unique attribute of this material, that makes it different from other C-based materials, is the lithiophilicity, the strong affinity of lithium to RGO. Those aerogels have excellent wettability with molten lithium, that indicates a strong binding between Li and the materials' surface. The electrodeposition of Li ion on graphene involves the participation of lithium metal, so a higher binding energy due to the presence of lithiophilic deposition sites produces an increased capacity, together with the nanostructured framework. Other carbon materials show relatively large contact angle (fig. 3.2), indicating relatively poor Li surface wettability, so the affinity need to be provided through a coating made on purpose.

The easy and large scale production method, the light weight, the extended and accessible inner surface, the pore sizes and distribution, the good mechanical strength, flexibility, compressibility, controlled inter-sheet connectivity, biocompatibility, good electrochemical and thermal stability and the distinctive features of catalytic activity and lithium affinity impart to this non-agglomerated networks interesting and important properties which are attractive for a wide range of applications, from absorption for both gas and liquids to electrochemical and biological sensors, from structural materials for electrocatalytic conversion to conductive elements in flexible electronic, from field-effect devices to high-performance electrochemical energy storage and conversion.

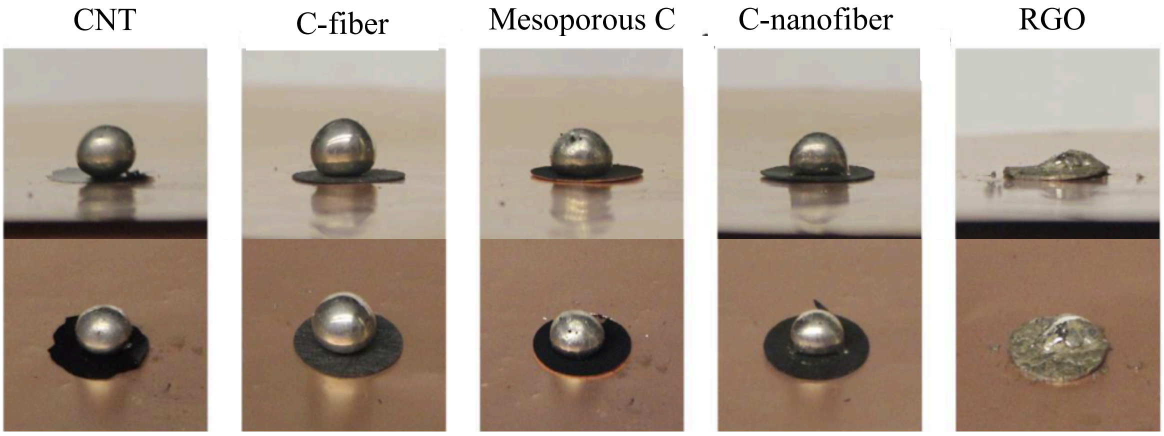

Figure 3.2: Surface wetting of molten Li on different carbon materials (*Adapted from Lin, D. et al., 2017*)

3.2. RGO aerogel for batteries

Micro and mesoporous graphene aerogels are key components in nanomaterial-based energy storage/conversion applications, in devices such as supercapacitors, solar and fuel cells but especially batteries, where it is used mainly as cathode in all kind of systems, especially to exploit their electrical conductivity with chemical stability, high surface area with a low cost. The unique 3D morphology allows most of the graphene sheets to be expose to electrolyte, providing with the pores open and large channels for the facile access of electrolyte and rapid diffusion for unobstructed transportation of the species. The active materials can be well embedded and uniformly distributed for an efficient loading, to take advantage of the intimate electrical contact with the useful conductive surface to receive electrons for the redox reactions. Those reactions induce volume expansion and contraction, due to the different densities of pristine materials and products, that can be easily accommodated by the flexible but strong structure.

Hybrid aerogels have been proposed as cathode materials not only for lithium-ion batteries, but also for sodium-ion batteries (SIBs), potassium-ion batteries (PIBs) and aluminum-ion batteries (AIBs). Because of the challenges of directly using graphene as electrode, RGO-based hybrids are promising substitutes that have attracted much attention. LCO, LTO, LMO and LFP, are the most common cathode materials for LIBs and have been extensively studied, but these materials have a low electrical conductivity, and thus, poor cyclic stability. The incorporation of these materials in a 3D conducting matrix, where these components will act as spacers to reduce the stacking of the leaflets to maintain a highly extended and more accessible inner surface and favor a more efficient ion diffusion channel system, can provide a better utilization of both the network and active species, can improve their conductivity, and consequently, the device performances. The RGO platelet intrinsic flexibility and strength can not only restrain the volume variations, but also prevent the disruption induced by the changes in these brittle materials.

Other transition metal oxides and metal sulfides and phosphides, like Fe_2O_3, Co_3O_4, SnO_2, $NiCo_2O_4$, TiO_2 have been used together with the RGO aerogels. The hybrid can be assembled synthesizing simultaneously the inter-connected isotropic conductive framework and the metal oxide, fully utilize the advantages of both graphene and active materials. The interfacial contacts between these components are important to the electrochemical performance. The inorganic part is homogeneously anchored on conducting RGO through oxygen bridges mainly originated from the pinning of hydroxyl/epoxy groups from graphene on the metallic atom of the ceramic, which facilitates fast electron hopping from conductive to insulating. During the fabrication of the hybrid, the aerogel can play the role of shaping the microstructure of the inorganic phase, its size and morphology, with the GO that can be used both as hard or soft template for the assembly, determining the secondary structure.

In most of the hybrids, the graphene content is normally higher than 10-20 wt%. This large amount of conductive carbon, that is not an active component, does not help to improve the energy density of the devices, but on the contrary, the specific volumetric capacity will be lowered.

RGO properties provide the right compromise to fabricate a cathode for a practical application of Li-S batteries, because provides a hierarchical, highly electron (between the building-blocks) and ion (inside the pores) conductive network, robust mechanical support and sufficient space for a high sulfur loading. Sulfur has a low electrical conductivity and a large volume change, and the cell is affected by the shuttle effect of the polysulfides during cycling. The residual oxygen functional groups of RGO sheets can enhance the adsorption of sulfur and polysulfide anions, contributing greatly to the stability of the S cathodes. Sheets structural flexibility allow to coat or wrap the surface of the S, encapsulating and immobilizing it in core–shell structure inside the carbon matrix, which increases its electrical conductivity, restraining and trapping, at the same time, the Li_2S_x in the cathode, where the pores act as reservoirs and confinement, acting as physical barrier film to retard the diffusion, hindering the shuttling. The presence of a large number of oxygenated functional groups on the GO with a high chemical activity improves the cyclic stability, because they can react with other reactive sulfur-based compounds and produce an *in-situ* hybridation with sulfur, RGO aerogels are less porous compared with porous carbon, which does not facilitate the confinement, but the incorporation of nanostructured sulfur could provide more accessible area for better utilization of both, because small size sulfur particles greatly improves the charge and ion transfer kinetics. The electrochemical performances of S/RGO cathodes depend strongly on the size of the sulfur particles, with small particles strongly embedded in the scaffold that provide improved capacity.

The functionalization of the graphene is highly effective to increase the binding energy of the surface to lithium polysulfides. A S-doped or/and N-doped graphene-wrapped sulfur cathode delivers a high specific discharge capacity at high rates which can be ascribed to the well-restored aromatic lattice and the stronger binding of the discharge products, which can be accommodated in large amounts the 3D scaffold, with the carbon surface. The functionalization also improves the conductivity of the sulfur composites, enhancing the electrochemical properties. Polymer modified hybrid graphene–sulfur composites have been studied, for example linking on the surface PEG to increase the affinity with S and its derivatives.

RGO is often used directly in combination with sulfur for one-pot synthesized composites, with the S distributed on the surface and between the interlayers of RGO, through an *in-situ* sulfur reduction of GO, performed at 600°C under vacuum. The reduction of graphene oxide can be performed also via one-pot hydrothermal synthesis, followed by pure sulfur impregnation via melt-diffusion method by heating the sample in vacuum, or a further treatment of the aerogel with KOH, to chemically activate the surface, generating high density of nanopores, to provide microreactors to constrain the dissolution of the active sulfur species, in close contact with the framework, or a coating with a Li_2S solution, to fabricate the cell in the discharged state. The hydrothermal treatment was also used to perform an *in-situ* growth of sulfur based on the reaction of Na_2SO_3 with GO at high temperature. A thermal reduction in inert environment was also performed on a mixed GO/S aerogel obtained by freeze-drying. Another RGO-S *in-situ* composite was instead chemically reduced in an oil/water bi-phase system, where the oil drops of the emulsion act as reactor of the crystallization of the stored sulfur on the surface of the GO sheets contained in the aqueous phase; afterwards, the reduction was carried out with hydrazine. Thiosulfate was likewise use to reduce GO sheets, producing a S-doped framework with higher affinity for the molecular sulfur. Reduction and *in-situ* sulfur particles formation can be performed at the same time bubbling H_2S into a GO aqueous suspension. The degree of reduction can be easily tuned by the amount of H_2S used, which can induce a reduction- induced assembly to obtain the 3D RGO–S hybrid (Yu, M. et al., 2015). Biporous electrodes containing both micro- and macropores are capable of embed and accommodate higher amounts of sulfur than homoporous ones, also facilitating the species diffusion, thanks to the controlled pore size distribution. This morphology can be obtained by a hydrothermal treatment of a GO dispersion, during which can also take place the *in-situ* crystallization of sulfur.

RGO aerogels satisfy all the requirements for a suitable air electrode in metal-air batteries, thanks to the hierarchical bimodal porosity, morphology of in which numerous large tunnels facilitate a continuous oxygen flow inside, while small pores provide tri-phase areas for the oxygen reduction, high specific surface area, good electronic and ionic conductivity, fast oxygen diffusion and chemical and structural stability (Williford, R. and Zhang, J.G., 2009; Xiao J. et al., 2011). The aerogel acts, as current collector to provide sufficient charge transfer for the electrochemical reactions, as repository to house the discharge products and 3D scaffold to host the catalyst for the reaction with the air in the cathode, which diffusion is controlled by the pore size distribution, volume and connection. Structural defects and edges on graphene platelets provide extra active sites for the ORR. The amount, distribution and type of defects are determined by the preparation process which can also be easily tuned.

The open surface of RGO can also be easily functionalized to improve its stability and catalytic activity. Another great advantage is the high surface area and conductivity of graphene that improves the effectiveness of catalyst particles loaded on it. Heteroatom (N, B, O, P, S, Cl, Se, Br, I) doping and functional groups enable to tune their electronic structures and tailor the electrochemical properties, enhancing the catalytic activity of the carbon materials, because increases the degree of lattice defectiveness and edge plane sites in the carbon network, where the reduction products prefer to nucleate and growth. The high electronic conductivity of the graphene sheets contributed to the low overpotential, while the defects caused by sp3-bonded carbon atoms in the graphene served as active sites. Doped and non-doped RGO aerogels have a good catalytic ability for the ORRs because of the presence of functional groups as defects, they are not adequate for the OER (Wang, Z. et al., 2014; Hu, C. & Dai, L., 2016). For this reason, many catalysts have been investigated to promote both reactions, such as metal oxides, metal nitrides, and precious metals, embedded on the C-based conductive layer. Their introduction can take place on the graphene surface by an *in-situ* growth during GO flakes assembly process, that result in strong covalent bonding or the formation of an oxygen bridge between the particles and the surface, leading to a promoted electron transfer process. Thanks to the extensive specific area and the three-dimensional arrangement, the interaction between catalyst and discharge products is emphasized, with an improved effectiveness of the catalyst load. The overall capacity is dependent on the quantity of the discharge product that can be stored on or within the porous electrode structure, that is proportional to the surface area and the porosity.

Xiao et al. synthesized a that self-assembled 3D hierarchically porous electrodes with functionalized graphene sheets that contain lattice defects and oxygen-containing functional groups, with the ability to accommodate the by-products of catalysis and enhance the pathway of air (Xiao, J. et al., 2011). A binder-free porous graphene electrode was prepared through templated assembly in a nickel foam (Wang et al., 2012). *In-situ* growth of catalysts, like Au, Ru, Co_3O_4, MnO_2, RuO_2 and TiO_2, was realized during assembly of the network, while a cell in the discharged state was fabricated introducing as a thin coating on the inner surface of a pre-formed framework Li_2O_2 (Dong, Y. et al., 2017).

Carbon materials are widely used also as additive in electrodes in small amounts to improve the performances and cyclability, increasing the electrical conductivity and providing connections between active material, usually low conductive, allowing current to flow in the electrode. RGO is an effective conductive additive, that improves the efficiency of conventional cathode active material by a different contact mode compared with conventional conducting additives. Graphene sheets can construct a flexible conducting network through a ‘‘plane-to-point’’ mode due to its flexible planar architecture, and thus, with a much lower mass fraction, fully-exfoliated graphene can bridge the active material particles more effectively with the highest contact efficiency, compared to commercial carbon-based conductive additives with a ‘‘point-to-point’’ conducting mode (Lv, W. et al., 2016). Increasing amount of conductive carbon decreases the electrode electrical resistivity until it reaches the percolation threshold of the interconnected conductive paths formed by these additives, and graphene allows to reach the threshold with a weight percentage one order of magnitude lower than carbon black particles thanks to a well-organized hierarchical conductive network, that decreases the additive content and improves the volumetric energy density, because there is a higher surface utilization and contact efficiency than other types of conductive carbon. The mass advantage is weakened by the lower conductivity than CB and CNT and the tendency of RGO to not be uniformly dispersed, but aggregated forming inseparable agglomerates (Han, S. et al., 2014).

Graphene aerogels can be also used as thinner, lighter, flexible and metal-free current collector, to reduce the gravimetric and volumetric energy densities of a whole battery, introducing a 3D network suitable to provide the active material the electron to undergo the redox reactions with a rough and crinkled surface that promotes the adhesion of the active layer. RGO can be also used as protective coating of the metallic current collector to inhibit the corrosion due to the electrolyte through electrostatic repulsion of the anions, avoiding the rise of the internal resistance due to the degradation products film and decreasing the interfacial resistance between current collector and active material, facilitating the electron transport thanks to the ample contact surface (Mahmood, N. et al., 2014).

N/S-codoped RGO was used as ultrathin coating deposited on a polyethylene separator to achieve an effective suppression of dendritic growth on the anode. The aerogel was obtained by hydrothermal reduction adding thiourea in the suspension, then vacuum-dried and dispersed in ethanol to be applied on the separator. This coating is very thin if compared to other ceramic coatings applied on separators for the same for the same purpose, but unlike these, is flexible and resilient. The lone pair electrons in the heteroatom dopants (N and S) led to the generation of negative charge, resulting in enhanced interfacial interactions between the coated separator and the lithium electrode, maintaining a uniform ionic flux on the metal surface and releasing the surface tension of lithium metal and suppressed the initiation of dendrite growth on lithium metal. The ultrathin layer also imparted thermal stability to the PE separator, thus preventing thermal shrinkage of the separator at elevated temperature and enhancing battery safety, providing improved dimensional stability of the polymer at elevated temperatures (Shin, W. et al., 2015).

Among the anode lithium insertion materials, lithiated carbons (Li_xC_n) are cheap and abundant, exhibit higher lithium storage capacities and more negative redox potentials versus the cathode than metal oxides or chalcogenides and show long-term cycling performance superior to Li alloys due to their better dimensional stability, introducing safety improvements into rechargeable lithium cells. The redox potential vs Li/Li^+ of lithiated carbon is close to 0V, which means that their reactivity is similar to that of metallic lithium, assisted by the Li_xC_n average particle size (10 µm), that lead to a large surface area which increases during cycling of the battery. (Claus, D. 2011)

The electrochemical formation of lithiated carbons is performed by an insertion reaction of lithium ions into a solid carbon host, according to the reaction:

$$Li_xC_n \underset{charge}{\overset{discharge}{\rightleftarrows}} xLi^+ + xe^- + C_n$$

During charge phase, the electrochemical reduction of the carbon takes place, and lithium cations from the electrolyte penetrate into the structure to form a lithiated carbon, while the electrons are accepted by the carbon lattice. The prerequisite for the formation of lithiated carbons is a host material that exhibits both electronic and ionic conductance. This insertion process is called “intercalation”, because if occurs into graphite, a layer of guest ions slides between the sheets of the layered matrix, while the host broadly retains its structural integrity, and is reversible, because during discharge there is an extraction of Li ions from the structure. The lithium motion is between two layers or through the basal plane at defect sites only. At ambient pressure, a maximum lithium content of one Li guest atom per six carbon host atoms can be reached for highly crystalline graphite. The intercalation increases the interlayer distance and produces a shift in the stacking order of graphite layers, from ABAB to AAAA, in this way two nearby LiC_6 layers directly face each other. Higher densities are obtained from graphitic carbon prepared under high pressure and temperature.

A mild oxidation of graphite improves the performances in Li/LiC_6 cells. Improvement are attributed to the formation of nanochannels in the vicinity of defects and impurities and to a SEI chemically bonded to carboxylic and oxide groups present on the surface, that induces a better wetting of the graphite by the electrolyte. The oxidation of the basal plane introduces defects on the graphite sheet, like oxidized groups, nanovoids and edge sites that accommodate extra lithium than the pristine graphite (Claus, D. 2011).

Li capacity of pristine graphene is limited by lithium clustering and phase separation and is lower than the capacity for Li intercalation in graphite. the high adsorption energy and barriers for Li diffusion make it ineffective as anode material. Reduced graphene oxide is the most suitable intercalation material for lithium among graphene-based carbon materials, thanks to its morphology and intrinsic defective content. In an anode, RGO aerogel is not only a conductive additive and a structural framework, but is also an active component of the electrode, contributing to the total capacity of the cell. The 2D based three-dimensional electronic conductive structure, the porous morphology, the disordered and defective surface and characterized by oxidized functional groups, that improves the electrolyte wettability and the wider inter-sheet distance between the leaflets are beneficial to rapid surface Li^+ absorption and rapid ions diffusion and electron transport, and thus make the materials containing heteroatoms superior to pristine carbonaceous materials, especially graphite. The plating of lithium ions on RGO is a defect-induced dendrite-free plating of lithium metal. The aerogel large surface area provides abundant surface defects and edges as active sites for lithium deposition. Its 3D frameworks, strong, conductive and chemically stable, with a laminar texture can effectively tolerate volume changes during cycling. The lithium affinity is promoted by the oxidized species on the surface, with a lower electrode polarization that boosts the electrochemical performances. The possibility to control the structure and properties of the three-dimensional graphene oxide sponges enables their practical use as protections for lithium metal anodes, which is caged within the pores, suppressing any dendritic growth.

It is well known that pristine graphene possesses a high theoretical lithium storage capacity of 744 mAh/g if Li ions are attached to both sides of the plane, with a low resistance to lithium diffusion. The electrochemical performance of graphene prepared by reduction of GO for direct use as the anode show a much higher capacity when compared with graphitic anodes. Graphite intercalation product LiC_6 provides a capacity of 372 mAh/g, while RGO-based anodes have a capacity ranging from 500 mAh/g to 1000 mAh/g thanks to the presence of metallic Li, which is competitive with other high-performance non-carbonaceous anodes such as silicon (4,200 mAh/g), germanium (1,600 mAh/g) and tin oxide (1,500 mAh/g).

RGO aerogel allow to pre-store lithium into the electrode providing an efficient loading, uniform distribution and an intimate electrical contact between metal and framework surface, which is a fundamental aspect to consider while designing Li metal anodes. Koraktar and colleagues studied the plating of lithium metal within free-standing porous thermally reduced graphene oxide networks. defects in the graphene lattice act as seed points for nanoscale nucleation of electrodeposited lithium metal within the porous structure, with an insertion mechanism different from electroinsertion in graphite, suggested by the absence of the standard intercalated state in graphitic anodes LiC_6 in the lithiation products, but consist in a predominance of Li_3C_8 and lithium metal within the porous graphene structure. The presence of a lithium intercalated state with a high lithium-to-carbon ratio and the bare metal explains the better performances than graphite. The metal strongly participates in the charge/discharge reaction of the porous graphene anode, and is completely absent in the fully delithiated sample. Compared with the intercalation of graphite, the electrochemical reaction of Li with graphene is a surface-mediated process and not a chemical reaction, where the carbonyl groups on the functionalized graphene electrode act as a reduction sites for lithium ions.

Stone–Wales defects, generated by pure reconstruction of a graphene lattice into non-hexagonal forms, are less likely to form in thermally reduced GO due to a high formation energy required for the incorporation of such irregularities, the existence of vacancies is more probable. Vacancies are can be distinguished in two types: single and multiple vacancy. A single vacancy is less stable because of the presence of dangling bonds derived from a missing lattice atom, while a multiple vacancy formed by two missing atoms, called a divacancy (DV) is much more likely to exist because thermodynamically favorable over single vacancies, and thus DV defects are highly prevalent in GO sheets reduced by the thermal methods, upshot which is consistent with simulation results. There is a high concentration of irregularities in defective graphene sheets, causing a decrease in the conductivity of the network, that can assist Li ion diffusion through the basal plane, which is particularly easy through divacancies, but is not the same for monovacancies and Stone–Wales defects, due to the energy barrier. 25% DV defect is the maximum limit for the presence of such a defect beyond which there will be dangling bonds of carbon atoms (Mukherjee, A. et al., 2014).

The nature of lithium adsorption on DV defects is different from the intercalation on graphite basal planes and also from defect-free graphene. With a simulation through DFT, were considered two sites for lithium adsorption, one on the top of a carbon atom and the site in the center of a hexagon, as shown in fig 3.3a. Lithium adsorption is not possible in pristine graphene and hence lithium atoms can only occupy the empty interlayer space between the planes. The packing density of Li atoms in graphite LiC_6 is dictated by the Li-to-Li and Li-to-C_6 van der Waals interactions. If a DV defect is introduced in the lattice (fig. 3.3b) removing a C–C dimer, the lithiation potential is the highest (0.7415 eV) at the center of defect while dropping to about half (0.3658 eV) at the location farthest from the defect, indicating that the defective zone is the most favorable site for lithium adsorption (Mukherjee, A. et al., 2014).

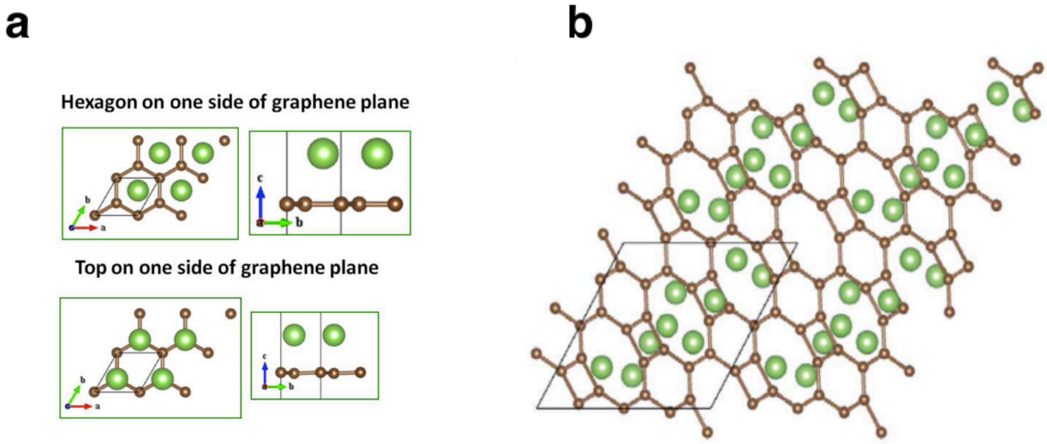

Figure 3.3: Lithium adsorption on a) defect-free graphene and on b) graphene with 25% DV defects (*Adapted from Mukherjee, A. et al., 2014*)

Li_3C_8 clusters near divacancies in the lattice, and such localized formation in the vicinity of defects act as seed points for the subsequent plating of lithium metal, resulting in a dendrite-free deposition, because the metal is confined within pores that are few tens of nanometers in size. the exterior surface area of the RGO aerogel is very small when compared with the total surface area contained within the bulk of the porous electrode, so the 3D structure serves as a sponge that absorbs the majority of the Li metal into the interior of the electrode structure. The lithiation in the spongy network is highly reversible: during plating the pores tend to be filled up by the metal, ending up being closes, constraining the lithium in the pore dimension. Upon charge, the lithium metal is released and the pores open up once again without leaving almost any residue in the delithiated electrode, resulting in a reversibly cycling that does tend to deteriorate very slowly the electrode–electrolyte interface with a minor loss of active lithium (Mukherjee, A. et al., 2014).

There is a strong correlation between the defects concentration and the specific capacities of the RGO aerogels. The higher the state of defectiveness, the higher the measured maximum charge storage capacities of the electrodes. Testing for over 1,000 charge/discharge cycles indicates excellent reversibility and coulombic efficiencies above 99%, with no indication of any significant dendritic growth, since the lithium metal is caged within the pores, facilitating extended cycling of the electrode. Graphene flakes flexibility can help improve the cyclic stability of electrode materials by forming a buffer structure, especially for anode materials with large volume variations, thanks to folds and wrinkles in the crumpled graphene contribute to form nano-cavities for lithium storage that can accommodate its volume change.

The presence of point defects isn’t the only favorable aspect for the better performances, but there is a strong contribution by the three-dimensional arrangement, because, compared to the irregularly aggregated graphene-based materials, provides large SSA and a curved uneven morphology that yields more lithium storage active sites, ordered pores which can shorten the pathways for rapid Li ion diffusion and increase the surface utilization, continuous electron-transport pathways as well as excellent mechanical strength. The carbons with rich porous structure have a higher capacity because they provide more active sites and spaces for Li adsorption and reaction. Compared to other C-based materials, RGO aerogels have much larger surface area and does not have a disordered pores structure, but during the initial nucleation stage of metal deposition, lithium nuclei size heavily depends on the current density, confirming the effectiveness of reducing the local current density by introducing a high-surface-area Li plating matrix. The graphene surfaces are in direct contact with the liquid electrolyte and are capable of rapidly and reversibly capturing Li ions through surface adsorption and a surface redox reaction (Pei, A. et al., 2017).

Together with lattice defects such as irregularities and vacancies, heteroatom doping could effectively tune the surface chemical properties and electronic band structure, and therefore improve the performance of the electrode. The presence of an unrelated atom can induce strains in the network or local polarizations that can improve the compatibility with lithium atoms. For example, the presence of a nitrogen atom provides a pair of π-electrons, making the sheet surface an electron-rich donor, with delocalized π-conjugation that naturally act as Lewis base sites to strongly adsorb Lewis acidic Li ions in electrolytes through acid–base interactions, guiding the metallic Li nuclei to uniformly distribute on the anode surface (Zhang, R. et al., 2017). The insertion process which involves metallic lithium is facilitated by the presence of oxidized functional groups on the surface of the RGO aerogels, which are lithiophilic matrixes. The possibility of being wet by molten lithium indicates a strong binding energy between Li atoms and the surface of the matrix, thanks to a good metallic Li affinity. Cui’s group first principles calculations based density-functional theory (DFT) calculation revealed that RGO surface groups such as carbonyl, alkoxy and epoxy groups exhibit much stronger binding energy to Li than the bare graphene aromatic ring (fig. 3.4). The strong binding can greatly increase the surface lithiophilicity, that together with the nanoscale interlayer spacing here enabled a powerful driving force for fast and efficient metallic lithium intake (Lin et al., 2017).

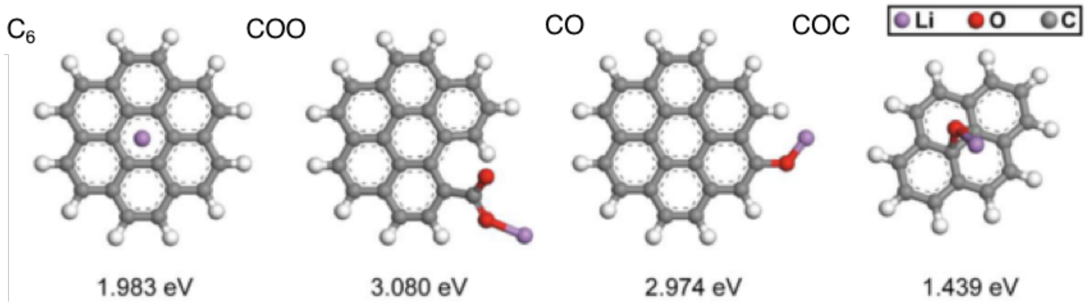

Figure 3.4: First-principles calculations on binding energy of lithium with different functional groups on the surface of reduced graphene oxide (*Adapted from Lin, D. et al., 2017*)

Thanks to its unique intercalation method, RGO enables the use of metallic lithium in all kind of Li-based batteries, combining both materials properties with the advantage of the intrinsic dendrite suppression. Cheng et al., proposed, as anode in Li-S batteries, to coat a CU foil with a slurry made of hydrothermally reduced GO aerogel and PVDF in NMP (Cheng, X. et al., 2015). A free-standing RGO aerogel can be used as electrode metal-free and binder-free, is made of only material that acts at the same time as scaffold for the active component, conductive additive and current collector, does not need any auxiliary materials (metallic current collectors, conductive carbon black and polymer binder), thus improving the gravimetric energy density of the whole cell, in which it can be used both as cathode or anode. Liu and colleagues proposed a binder-free bielectrode for Li-ion batteries, made of a free-standing and flexible paper with folded structured graphene made pressing the RGO aerogel obtained from freeze-drying a GO aqueous dispersion and then thermally reducing it in air at 200°C. The folded structure is complex and has different properties and functionalities from 2D planar structures, because can provide more lithium insertion active sites, such as edge-type sites and nanopores, guaranteeing a reversible capacity of 568 mAh/g after 100 cycles (Liu, F. et al., 2012). The self-standing electrode can be also prepared with graphene oxide already reduced in inert environment at various temperatures to control the reduction degree, dispersed in water with the aid on surfactant and then vacuum filtrated. (Han, S. et al., 2014). Koraktar's group prepared the electrode vacuum filtrating a GO flakes dispersion to realize a flat, free-standing paper which was further reduced through rapid heating in Ar flow to induce deoxygenation (Mukherjee, A. et al., 2014). The three-dimensional RGO structure can be used to produce a dual conductive network Si–C and Li alloy-C hybrids to further improve the electrochemical cyclability and rate performance (Zhao, J. et al., 2017).

Free standing paper-like anodes are also useful in the development of flexible integrated electrodes for wearable energy storage devices, that can be repeatedly bent without structural failure or performance loss. An aqueous dispersion of RGO can be used to prepare a graphene ink, easy to deposit it on flexible substrates to prepare a flexible electrode, free of binder and current collector materials. There are other forms of flexible electrode that can be constructed from graphene. For instance, a unique 3D graphene-on-graphene structure can be made with a 3D interconnected graphene conductive framework, which porosity is favorable for Li$^+$ diffusion, homogeneously connected by a few-layer graphene film, that acts as non-metallic current collector which can effectively collect/transport the charge carriers (Lv, W. et al., 2016).

Pure graphene is difficult to as the anode for practical applications because the amount of lithium absorbed on single layer sheet seems to be greatly reduced due to repulsive forces between Li$^+$ on both sides of the graphene, hindering the formation of the intercalation phases. Pore walls in RGO, formed by more than two stacked sheets, are convenient to reduce the repulsion between adsorbed ions, improving the useful capacity, that can be improved by functionalization and heteroatoms doping. The capacity is not the only issue and other factors also need to be considered for practical applications: the main drawback of using reduced graphene oxide as the anode is its low coulombic efficiency and poor cycling stability, especially because the formation of SEI in pores and on defects. Furthermore, during electroplating small Li clusters may be formed on the graphene surface and these can potentially nucleate dendrites (Lv, W. et al., 2016).

Since there is the presence of metallic lithium, instead of electrochemical insertion, which is inefficient and difficult to realize in industrial applications, Cui and colleagues proposed direct introduction of Li metal inside the structure by thermal infusion, leveraging the lithiophilicity of the material. They realized a GO paper-like free-standing membrane through vacuum filtration, which was then reduced by Li-assisted spark reaction when put in contact with molten lithium, which causes gas generation that results in a significant volume expansion, generating uniform nanogaps. Just like water is absorbed into a hydrophilic porous structure, liquid lithium can be infused into a matrix by simply touching the edge, thanks to the low distance between the layers and their lithiophilic surface, which has a strong binding with the metal. The capillary force that lifts molten lithium in the nanoscale interlayer spacing is a powerful driving force for fast Li intake inside the RGO, that functions as stable host scaffold for liquefied Li entrapment. This prelithiated layered composite anode of Li/reduced graphene oxide restrained the relative volume change of Li anode by dividing dense Li in smaller domains into the nanogaps between the sheets, resulting in much more stable, stress-controlled and dendrite-free cycling. This solution provides higher reversibility because does not involve any reaction between ions and carbon, so it doesn’t form a new specie, but the RGO is directly hosting metallic lithium. This sparked RGO aerogel offers mechanical flexibility and an extensive active surface, greatly reducing the effective current density and homogenizing the ion flux, resulting in a safer cell. Compared with the electrodeposition approach, pre-storing Li via thermal infusion has several distinguished advantages: no sacrificing cells are needed, which is practical for scalable production; the highly reactive molten Li removes unstable species at low potential of Li^+/Li, preventing continuous Li consumption in electrochemical cycling; and a uniform Li distribution can be easily obtained by thermal infusion, whereas electroplating usually brings about uneven Li deposition (Lin, D. et al., 2017).

3.3. Synthesis approaches

Graphene oxide is the perfect building-block to build three-dimensional structures, because in its planar architecture gathers the good mechanical properties deriving from the original graphene with the easy bonding ability induced by the presence of functional groups.

Graphene oxide (sometimes referred as graphite oxide) is the most common precursor for the synthesis of graphene materials prepared at a larger scale. This intermediate can be obtained by liquid-phase exfoliation of highly oriented pyrolytic graphite (HOPG) powder. GO is usually synthesized through the intercalation and oxidation of graphite using oxidants including concentrated sulfuric acid, nitric acid and potassium permanganate based on Brodie method, Staudenmaier method or modified Hummers method. The latter method, widely used, sets up the mixing of the reactants to form a strongly oxidizing specie that, when heated to around 55°C and placed in contact with organic compounds such as graphite, causes a series of micro detonations to functionalize the carbon surface. The exfoliation efficiency and the amount of functional groups introduced, consisting of hydroxyl (C–OH), carboxyl (O=C–OH), carbonyl (C=O), and epoxy (C–O–C) groups randomly distributed on the surface (fig. 3.5), strongly depend upon the permanganate concentration. The high density of oxygen functionalities, can stabilize the dispersion of the GO nanosheets in water, with which form strong hydrogen bonds thanks to the high hydrophilicity introduced by the oxidation. The strong interactions of graphene oxide in water play an important role, because high solubility and hydrophilic allow to be well dispersed at high concentrations. However, the basal plane would retain some of its hydrophobicity, rendering GO amphiphilic. The intercalation with water can cause lattice expansion, increasing the distance between the graphite planes from 0.335 nm to 0.6–1.2 nm, establishing monolayer flakes. Then, after strong mixing or weak sonication, the van der Waal's binding forces are easily overcome to form thin mono or few layer graphene oxide materials, separating the nanoplatelets (Dreyer, D.R. et al., 2009).

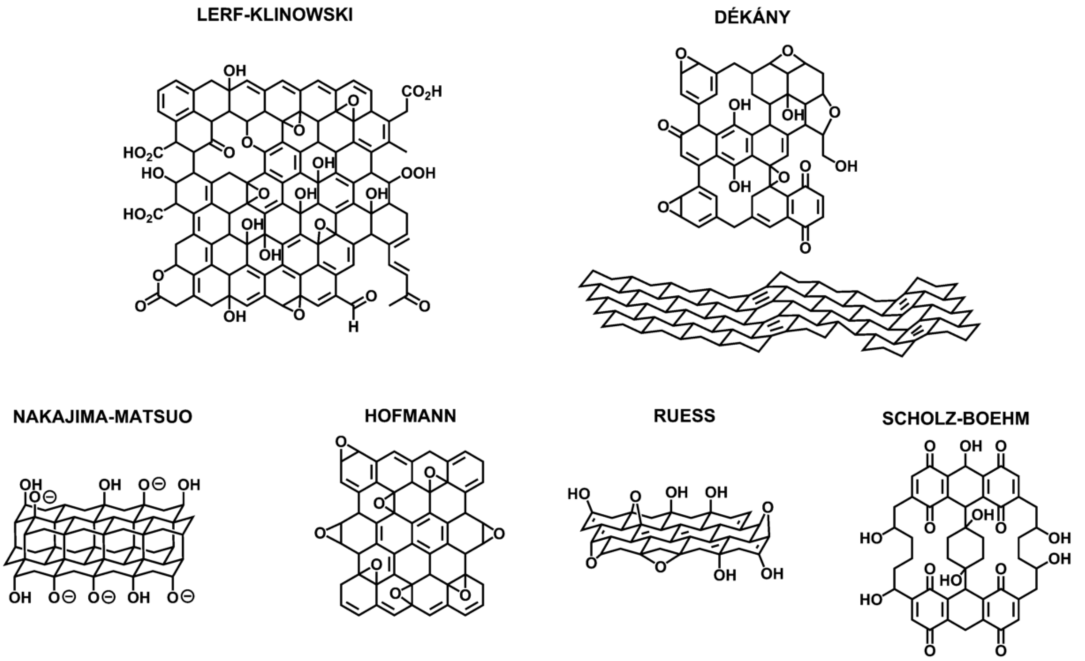
LERF-KLINOWSKI
DÉKÁNY
NAKAJIMA-MATSUO
HOFMANN
RUESS
SCHOLZ-BOEHM

Figure 3.5: Proposed structural models for graphene oxide (*from Dreyer, D.R., et al., 2014)*

Thermal or chemical reduction of graphite oxide is one of the conventional procedures to prepare graphene in large quantities, to restore the aromatic structure. Reduction of GO leads to reinstatement of sp^2 regions by removal of the functional groups, but the elimination of oxygen is incomplete, leaving some heterogeneities introduced during synthesis, with the material still exhibiting significant spatial irregularity, that leads to a restacking of reduced GO sheets during assembly. the reduction of GO to graphene is necessary to recover the conjugated network and electrical conductivity, however, it has been found that the combination of sheet defects, poor dispersion, restacking and multilayer thickness can prevent the full realization of graphenes' electronic and high surface area properties. Despite the disadvantages, graphene oxide reduction allows large scale production, is substantially easy, and low cost, compensating for the complex, expensive, hazardous and time requiring graphite oxidation (Alam, S. et al., 2016).

RGO individual layers are amphiphilic like the precursor, in contrast to graphite. GO can be dispersed in several different solvents with the aid of ultrasonication: acetone, ethanol and DMSO show short-term stability and precipitated completely in a matter of hours, while DMF, THF and NMP exhibit long-term stability comparable to that observed for the dispersion of the same material in water. In these solvents graphite oxide can be exfoliated into individual graphene oxide sheets or at most sheets composed of a few layers, forming long-term stability dispersion after sufficient sonication. (Paredes, J.I., et al., 2008). A homogeneous well-disperse colloidal suspension in solvents without surfactants or other stabilizers is intrinsically useful and fundamental for the 3D network formation process. However, RGO does not have the same solubility in all the same solvents as GO: in acetone, DMF and THF there is no homogeneous colloidal suspension, while the dispersion in ethanol, DMSO and NMP is stable. In water the suspension is provided by an electrostatic stabilization between negatively charged groups at the edges of the sheets. (Park, S. et al., 2009) Different solvent also result in a different volume change of the aggregation products (Hu, H. et al 2013).

The aggregation of these nanoleaflets in water gives birth to an interconnected 3D hydrogel with controlled morphology and structure through synthesis methods necessary to achieve long range order and conductivity between the individual graphene sheets, to overcome the challenges of poor dispersion and restacking, important for maintaining graphene's properties in bulk and to enhance graphene utilization for practical applications. All the techniques utilize two-dimensional graphene sheets to compose solid hierarchal three-dimensional networks of graphene, like sponges, foams, templates, and aerogels, all structures that exhibits high surface area and accessible pore volume as well as high strength and conductivity at extremely low density. All these top-down methods consist in a direct gelling of high aspect ratio GO sheets due to interactions of during reduction, forming a solid network which interacts through physical or chemical bonds to trap many times their weight in water, where hydrophilic groups can create strong surface tension, that prevents the liquid from flowing and disrupting the bonds. Each method consists in different temperatures, additives, reduction approach and tools, but all share a similar growth philosophy at high temperature, followed by post-treatment to remove the sacrificial support or to grow any composite materials inside, as well as a drying process for the elimination of the solvent from the hydrogel (Chabot, V. et al., 2014).

The first intuitive procedure is the template growth method, can provide a convenient way to control the distribution and arrangement of the constituting elements, which arrangement is defined by a pre-existing and preformed pattern, controlling long range order for fabricating highly ordered macroporous graphene architectures with tunable open porous morphologies. The pore size and the number of graphene layers could be effectively controlled by the size of the templates and the GO suspension concentration or growth conditions. Frameworks obtained with this technique possess a higher specific surface area (as high as 850 m^2/g) than those produced in other ways (normally 100–700 m^2/g), with a density as low as 0.18 mg/cm. The template, usually removed after construction of the framework, can provide a robust free-standing shape-defining application platform or support for guided material growth. The pattern can be made of various materials, like Ni foams or nanoparticles, zinc or aluminum oxide, spheres either made of silica or polystyrene. Usually this technique is used with CVD graphene, making it a bottom-up process, grown at ~1000°C on a metal catalyst which selects a specific morphology, to produce few layers very similar to pristine mechanically exfoliated graphene on a small scale, but contaminated by metal atoms due to diffusion. Instead of gases, the template is permeated by the suspension, and the structure is produced by chemical or physical deposition onto its surface, with the volatile solvent removed by endothermic evaporation, which leads to the condensation and packing of the GO film on the pattern, followed by pyrolysis. It is possible perform *in-situ* reduction of doping agents or precursors to fabricate composites and/or doped RGO. Compared with the conventional CVD process, which produces a limited amount of graphene, large amounts of RGO can be produced using the template-assisted method, even if the scalability of such material to large volume using these templating and high temperature processes is limited (Chabot, V. et al., 2014).

A rapid solvent loss can induce a strong capillary force that pushes together and deforms GO sheets, that assume the form of a hollow crumpled structure. The fast solvent removal can be performed by spray or aerosolization of the suspension, with an evaporation from the droplets that compresses and aggregates the graphene oxide, shaping it in a wrinkled ball of the same dimension and aspect of the original droplet. Although the crumpling process can take place at room temperature, the precursor can simultaneously be thermally reduced to RGO if the collapsing is carried out at an elevated temperature, after which the material can be easily redispersed in solvent thanks to the compressive strength of the sheets, that makes them resistant to the aggregation without breakings. Composites can be fabricated spraying mixtures of GO and pre-synthesized nanoparticles, which will be well embedded in the matrix wrinkles, or their precursors, for crystallization and growth localized on both inner and outer carbon surface if the aerosolization takes place in a furnace (Jiang, L. & Fan, Z., 2014).

Another solution for the generation of free-standing graphene sponges is starting from flat paper-like tightly stacked layers GO films and perform a reduction to induce dehydrogenation and deoxygenation to form the porosity, which can sometimes be unpredictable and uncontrollable, because may result in a varied thickness due to the shrinking lattice space and the expansion caused by rapid gas formation, with a loss of film flexibility and embrittlement. The reduction can be performed through thermal shock induced by rapid heating in inert environment (Mukherjee, A. et al., 2014), chemically using hydrazine in small quantities to maintain intrinsic flexibility and mechanical integrity (Niu, Z. et al., 2012) or exfoliation of the film using a low power laser to slowly leaven and efficiently reduce the graphene oxide, controlling gas release during the process, achieving ultrahigh SSA, 1500 m^2/g (El-Kady, M.F. et al., 2012).

Self-assembly of GO sheets is the most common and used bottom-up process to obtain 3D graphene interconnected structures, directly produced with a cost-effective sol-gel process through freeze-drying of a GO randomly dispersed suspension to form a spongy hydrogel, which can collapse if reintroduced in a humid environment or immersed in water, causing the dispersion of the flakes. Therefore, chemical reduction is not a feasible solution, but need to be performed by thermal heating in dry environment, without a rapid heating to avoid a thermal shock that can lead to a fast gas releasing that can break the frail structure, or with strongly reducing vapors. A better solution is to reduce the oxidized components while assembling. In a stable sonicated water suspension, single GO sheets are well dispersed by the electrostatic repulsions derived by the polarization from the functional groups, which counteracts the van der Waals' attractions between the basal planes. At the beginning of the reduction process, if the concentration is high enough, the platelet shifts from a hydrophilic state to a more localized hydrophobic regime due to their restored conjugated domains and diminished oxygenated functionalities, which causes a weakening of the hydrogen bonding with water and an increase in the thermodynamic stability. Decrement in the solvation strength and mutual restriction of mobility result in an increased attraction between the slightly reduced planes, that tend to aggregate. Once the force balance is broken, the gelation starts, and GO interconnect with each other to form a 3D architecture, driven by π–π stacking interactions of graphene sheets, confirmed by the decreased interlayer spacing. Furthermore, the change in hydrophilic character during GO reduction, stated by the increase of C/O ratio, can allow for increased strength and control of pore size, maintaining high area at increased density, because the van der Waals' forces became stronger and the self-assembled RGO hydrogel became more rigid and dense. The residual hydrophilic oxidized groups, due to the incomplete reduction, can encapsulate water in the process of self-assembly, which is fundamental in the successful construction of the hydrogel, which takes on the shape of the containment vessel. Self-assembled structure fabricated without the use of any sacrificial template during precursor synthesis and without the need of carbonization after the drying. Among the carbon nanostructured materials, functionalized graphene is the only one able to self-assembly in mechanical resistant structures. (Mao, S., et al., 2015; Chabot, V. et al., 2014).

The obtained highly cross-linked networks usually have a higher conductivity than the precursors because the reduction promotes the assembly of graphene sheets, removing interlayer water molecules and functional groups containing heteroatoms. The cross-linking of the flakes is due to divalent and trivalent coordination between the oxygen functionalities on the surface, that can form hydrogen bonding between them or condense with the elimination of a water molecule (fig. 3.6), with the formation of single σ bonds due to carbon atoms with sp^3 hybridation. The formation of bonds between the versatile nanoscale building-block strengthen inter-sheet interactions, reduces swelling, enhances thermal stability and provides more even distribution of stress. The self-assembling of 2D graphene into 3D macrostructures is driven by random stacking interactions of delocalized electrons in π orbitals restored by reduction, due to the partial overlapping that leads to a coalescence of the flexible pieces, in contrast with other self-assembled hydrogels, made of small molecules held together by weak electrostatic interactions (Xu Y. et al., 2010).

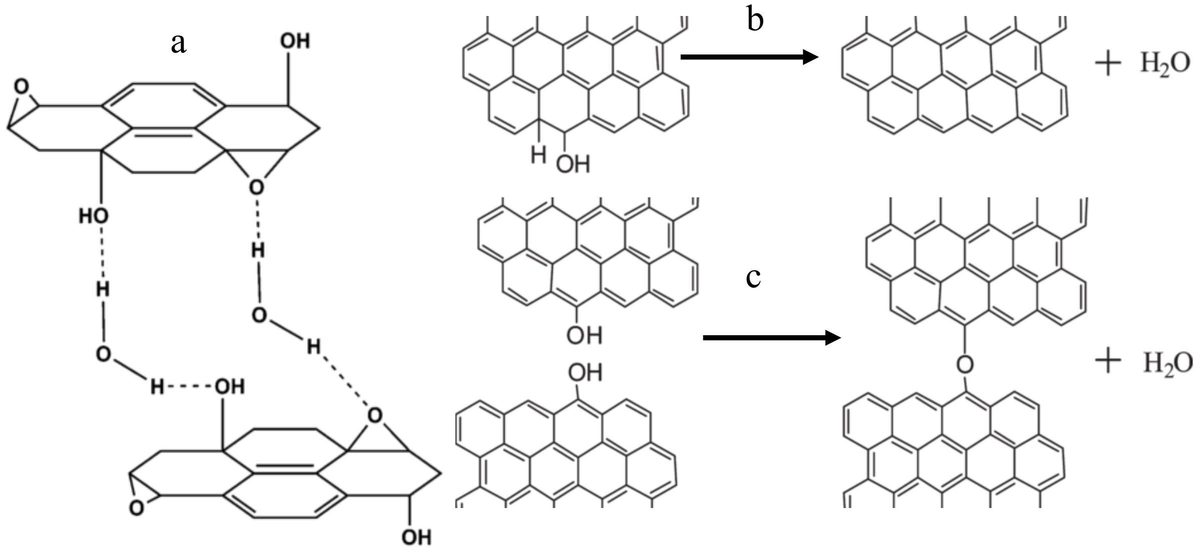

Figure 3.6: Schemes representing a) inter-sheet hydrogen bonding b) intra-sheet dehydrogenation c) inter-sheet dehydrogenation (*Adapted from Dreyer, D.R. et al., 2009 and in Zhou, Y. et al., 2009*)

The gelation of a GO suspension can be activated in several ways, by chemical reactions, changing the pH of the solution, adding cross-linkers or by physical treatments like the abovementioned freeze-drying, controlled filtration/centrifugation/baking, light induction, electrochemical deposition and the most and widely used thermal and hydrothermal treatments, or the combination of some of them. After assembly, carried out with any technique, the structure need to be dried to prepare the aerogel, by freezing or supercritical CO_2 drying. Each technique has a different efficiency in oxygen removal, for example, chemical reaction achieves higher reduction degrees than hydrothermal, but, as said before, is an aggressive mechanism, which causes a rapid gas release that can be counterproductive for the self-assembly, while hydrothermally reduced three-dimensional architectures have extensive pore structure that allows a more controlled gas release. Thermally obtained hydrogels are mechanically stronger than conventional self-assembled hydrogels due to the graphene physically linked skeleton, and similar to the thermal reduction in a vacuum or an inert gas environment, the high pressure and temperature in a hydrothermal process can remove the oxygenated functional groups by breaking the bonds between the carbon and oxygen groups. These methods allow to easily fabricate RGO composites starting from GO and precursors in aqueous solution, to perform an *in-situ* decoration of nanostructured hybrids, suitable thanks to the large accessible inner surface and pores system, with metal oxides and sulfides, like MoO_2, MoS_2, MnO_2, TiO_2, Co_3O_4, Fe_2O_3, SnO_2, NiCoO (Giardi, R. et al., 2015; Gigot, A. et al., 2016, Zong, M. et al., 2014, Zhao, M. et al., 2016) or a S, N, P or B-doping of the surface (Shin, W. et al., 2015; Zhou, G. et al., 2016).

Connections can be also built up by cross-linkers introduced in the dispersion, provided of long chains like polymers or CNT (Sui Z. et al., 2012) to enlarge the pore dimensions and reduce the sheets interaction, or small molecules, especially containing amino groups like pyrrole, pyridine or ethilendiammine (Zhao Y. et al., 2012; Hu H. et al., 2013) that can strongly attract the negatively charged GO sheets, improving mechanical properties, to allow the sponges to survive drying more easily and to tune the pores size and distribution.

There is a strong concentration effect on the assembly: if it is sufficiently high, there is enough overlapping of the flexible sheets to assemble and enough binding sites to form a compact 3D porous network with pore sizes ranging from submicrometer to several micrometers; on the other hand, if the concentration is low, the architecture will be loose packed and characterized by macroporosity and lower mechanical and electrical properties, due to the reduced number of inter-sheet connections. The size of the GO flakes also give an important contribution on the assembly efficiency and mechanism, because of the number of useful cross-linking sites. These leaflets have a high aspect ratio that can inhibit the rotational motion within a gel, increasing the number of contact points between sheets. The nanoplatelets are characterized by a large lateral dimension that promotes the hydrophobic effect of the basal plane, which can be hindered by highly oxidative carbonaceous debris complexed to oxygen functionalized graphene sheets (1/3 of the mass), produced regardless of the oxidation or technique used, to remove to reveal the true monolayer nature and improve the quality of sheet interaction (Thomas, H.R. et al., 2013).

After the mild reduction that triggers the self-assembly of the hydrogel, a further reduction can be performed to adjust and tune the amount of oxygen functionalities to increase the conductivity and mechanical strength, which induces a volume shrinkage due to the enhanced the cross-linking (Hu H. et al., 2013). The additional reduction can be performed on the hydrogel, through and electrochemical reduction (Shao Y. et al., 2010), or on the dried aerogel, by means of a thermal annealing over 1000°C under argon atmosphere or flushing H_2 (Zhao Y. et al., 2012), a solvent free microwave irradiation for few minutes (Hu H. et al., 2013), or low temperature methods, like flushing inside hydrazine vapors or immersing it in solutions containing hydrazine, sodium borohydride, hydroquinone, hydroiodic acid (Shi G. et al., 2011, Dreyer, D.R., et al., 2014). The main problem with the latter treatment, which has less impact on the microscopic pore structure, is that can generate large quantities of gas capable of breaking apart the aerogel, together with a high toxicity of the reducing agents, that makes it mandatory a long dialysis in ultrapure water to remove the residuals.

3.3.1. Hydrothermal Synthesis

Among the solution-processed routes to produce self-assembled structures, hydrothermal treatment offers the greatest ease for functionalization and bulk-scale processing. Hydrothermal synthesis is characterized by chemical reactions performed in a sealed and heated aqueous solution above boiling point of water at appropriate temperature (100–1000°C) and pressure (1–100 MPa): both have important effects on the speed and result of a hydrothermal reaction. If the solvent is an organic liquid, the reaction is called solvothermal (Xu R. et al., 2011). The reduction of the GO suspension in water and the consequent self-assembly is carried out at a temperature that ranges between 120°C and 180°C for a period which varies from 1 to 20 hours. Usually, lower the temperature, the time required for the completion of the reaction is longer. It is a simple route to obtain graphene in only one step with a very simple setup, requiring only an autoclave and an oven, which makes it easily scalable for industrial applications. Inside the closed system, water at relative high temperature and internal pressure promotes the recovery of π-conjugation after dehydration, with the degree of reduction, expression of the extent of conversion, controlled by temperature, pressure and time (Zhou Y. et al., 2009; Tang Z. et al., 2010; Xu Y. et al., 2010).

The conversion is water-based because only utilizes superheated water, so it is intrinsically pure because it utilizes water without the necessity of introducing heteroatoms or impurities like most of the chemical treatments. Reaction medium is the most important constituent of system, because water is an environmentally safe material and cheaper than other solvents and thus remains the most widely used solvent in high-temperature high-pressure synthesis. The hydrothermal system accelerates the reactions rates involving ions and complex molecules, if compared to solid-state reactions, thanks to the easier and quicker diffusion in liquids, it significantly changes the redox potential of the reactants and induces an intensification due to the more effective thermal conduction (Akiya, N. & Savage, P.E., 2002).

When hydrothermal conditions are applied to water, the liquid is heated in a closed system, that determines an increase in the applied pressure. The physicochemical properties of the solvent are highly dependent on the intensive variables of temperature and pressure, and undergo to a significant change: for example, density, surface tension, and viscosity of water will be lower, while vapor pressure and ionic conduction rise. The chemical and physical properties can be tuned controlling the engineering of temperature and pressure. When water is above its close or above to its critical point temperature (374.1°C) and pressure (22 MPa) is defined "superheated", "supercritical" or "near-critical", in practice this definition is extended to water under pressure above 0.1013 MPa (1 atm) and heated above its boiling point in a closed and sealed system. At standard conditions (25°C and 1 atm) liquid water has a density of 0.997 g/cm^3 and water vapor has a density of 2x10^{-5} g/cm^3, but, increasing the temperature, the density of the liquid diminishes and that of the vapor rises. Supercritical water is a clean, powerful, and stable solvent for organic species even though its molecules show a similar polarity to the ambient water. The correlation between and temperature of water depend on the degree of fill of the reaction vessel, with higher pressures reached with a more filled volume. When water is heated above its boiling point, the ionic reaction rate increases, in according with Arrhenius equation, because the dissociation (ionization) constant of water is directly and exponentially correlated with the rising temperature. Under HT-HP conditions, ionic or hydrolysis reactions are promoted and accelerated because water tend to be more dissociated into H_3O^+ and OH^-, becoming both a stronger acid and a stronger base as the temperature increases. The formation of hydronium cation and hydroxide anion causes a decrease in the dielectric constant of the solvent, which has a critical role in dehydration phenomena happening during hydrothermal reactions. The increase of dissociation constant and the coinciding lowering of the dielectric constant suggest a structural evolution, because at the supercritical state the hydrogen bonding formed between water molecules breaks. This transformation leads to significant promotion of the mobility of molecules and ions in water, which under hydrothermal condition is much higher than under normal condition, and is due to a viscosity decrease and a diffusion coefficient increase (Brunner, G., 2009). Superheated water exhibits properties like polar organic solvents, the so-called pseudo-organic solvent, assuming an increased affinity and solubility for organic compounds, like GO and reduction by-products, whose isolation and separation will be facilitated once the water is cooled (Kappe, C.O. et al., 2009).

Water need to be contained in specially tightly sealed containers or high-pressure autoclaves to reach the hydrothermal conditions, and this is the only equipment required, together with an oven or a furnace, to perform the reaction. The autoclave needs high mechanical strength to bear and resist high pressure and temperature experiments for long duration, good sealing performances to realize the required temperature and pressure conditions and outstanding capability of containing highly corrosive reagents acid, alkali, and oxidant resistance. Usually, to satisfy all the requirements for mild hydrothermal reductions, the vessel is composed by an external stainless steel thick jacket, with an internal inert liner make of Pyrex or Teflon, which maintain their inertness even at high temperatures. These are externally heated and internally pressurized autoclave, which generate an autogeneous pressure depending on the degree of filling, the type fluid and the external temperature, but there are also externally heated and externally pressurized autoclaves and internally heated and externally pressurized autoclaves (Xu R. et al., 2011).

Water brought to hydrothermal conditions acts both as solvent and reactant, consequently accelerating the reaction because induces a change in chemical and physical properties of reactants and products. The non-ideal and non-equilibrium states are key features of the HT-HP reaction system. Supercritical water can play the role of reducing agent in hydrothermal conditions and offers a green chemistry alternative to organic solvents. Superheated water promotes acid-catalyzed reactions of organic compounds because of a higher H_3O^+ cations concentration under supercritical conditions, inducing and ionic bond cleavages due to proton-transfer reactions in which water interacts with reactants via hydrogen bonding (Zhou Y. et al., 2009). The hydrothermal reaction has a strong dependence on the pH value of the dispersion. A basic pH yields a stable RGO solution, while an acid solution results in an intense aggregation of the graphene sheets, which cannot be easily dispersed. In a solution containing as solvent only ultrapure water at high temperature, the pH will be around 3, with the water that acts as a source of H_3O^+ for the protonation of OH, performing a H^+-catalyzed dehydration. This is a reversible reduction process, because not all oxygen functional groups are removed from the functionalized graphene at the end of the reaction, and the sheets will contain residual negatively charged defects.

The nature of the bonding between the sheets has not been completely defined yet, if the cross-links that form the hydrogel are chemical or physical connections, because reduction products are hard to characterize and quantify as in other methods such as photochemical and thermal reduction, because the process occurs inside an autoclave and is thus harder to follow. GO reduction produces a loss of almost half of the original mass, related to the difference in oxygen content measured by C/O ratio by means of XPS or EDS. The reduction pathways that take place during hydrothermal treatment have been widely studied by Hu and colleagues. They studied the products formation during reduction of Lerf−Klinowski model of GO through titration with ammonia. When organic materials are exposed to the superheated water, the most common reaction is the cleavage of the linkage between carbon and the heteroatom oxygen, which is accelerated by the hydrothermal conditions. This bond is common to several oxidized functional groups, whose structure and chemistry evolves on different routes as shown in fig. 3.7. The reduction produces molecules like CO_2, H_2O, CO, and small organic fragments. The analysis and quantification of these compounds allow to study and determine the path followed during the reaction. However, these byproducts can affect the chemistry of the forming self-assemble RGO hydrogel if they are not removed from the reacting system but also the structure, because it is an evolution of gases that can alter morphology, organization and stacking of the architecture (Hu K. et al., 2016).

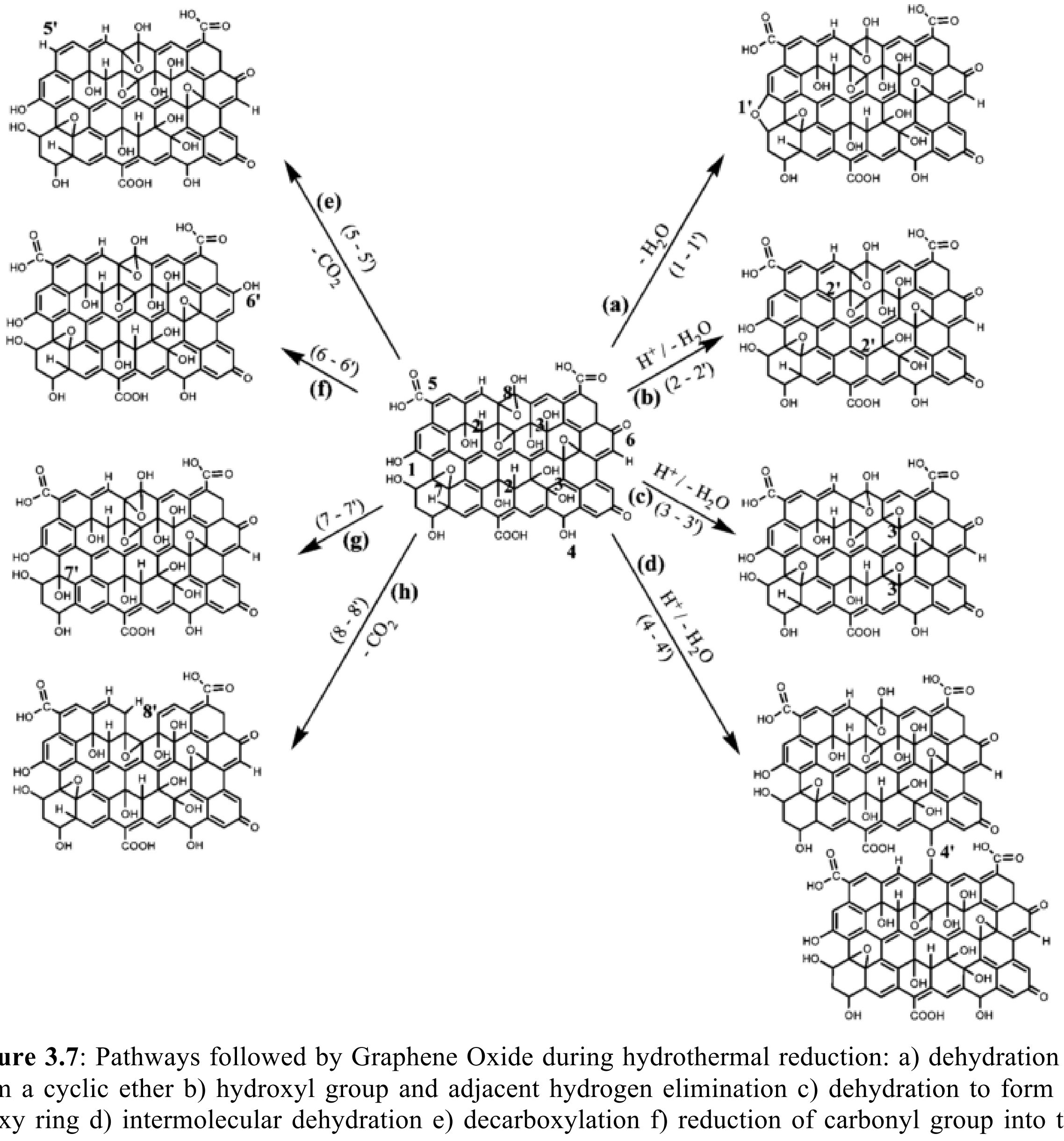

Figure 3.7: Pathways followed by Graphene Oxide during hydrothermal reduction: a) dehydration to form a cyclic ether b) hydroxyl group and adjacent hydrogen elimination c) dehydration to form an epoxy ring d) intermolecular dehydration e) decarboxylation f) reduction of carbonyl group into the hydroxyl group g)epoxy ring opening due to adjacent hydrogen h) decarboxylation by consuming carbon from the GO skeleton (*from Mungse, H. et al., 2014*)

Deoxygenation of GO causes a loss in the mass which is around half of the original weight, which implies that main fraction of the reduction products is in the form of CO_2. The evolution of this dominant specie is preceded by the transformation of all the functional groups into carboxylic acids, whose will then decarboxylated to form CO_2. Direct decomposition of carboxyl groups located on the edges occurs at temperatures lower than 100°C, however, only a few carboxylic acids exist at the edges of GO, and they cannot fully account for the large quantity of gas produced. An epoxide group can rearrange in a carboxylic acid through an acid-catalyzed ring opening, due either to the HP-HT induced water auto-dissociation or to the presence of a closeby hydrogen atom on an α-carbon, followed by an interaction with a nearby ketone, to form a carboxyl group and a conjugated π-bond. The formation of a COOH group can take place via disproportionation of a C−C bond between a hydroxyl and carbonyl due to a nucleophilic attack of n hydroxide, and the new formed group will be decarboxylated under further hydroxide nucleophilic attack, leaving a double bond. An important fraction of the mass reduction is due to the water loss, in the form either of physisorbed water and as dehydration of hydroxyl groups due or to hydrogen ions from supercritical water that extract the OH from the group, or to the presence of a closeby hydrogen atom on a carbon. The water elimination, that can be inter or intra-molecular, inter or intra-sheet, can generate carbon single and double bonds, ether and epoxide linkages, depending on the surrounding of the reacting species. Aside from small molecules, bigger byproducts as organic volatile fragments, containing oxygen moieties, are released during gelation after nucleophilic or electrophilic attack to labile functional groups followed by an oleofinic bond cleavage. The detachment and desorption of the abovementioned debris adsorbed on the surface, derived from GO synthesis, is another source of organic fragments. H_2O, CO can be evolved from decomposition beyond 100 °C of functional groups such as hydroxyls and carbonyls without conversion in carboxyl, but molecules produced in this way are a small fraction of the total mass of byproducts. These reactions, if occur on functional groups located on the plane, can produce holes useful to the elimination of the gaseous species (Hu K. et al., 2016).

The hydrothermal process promotes the one-step restoration of conjugated π–π structure upon reduction after dehydration due to the repairing the aromatic structures during the three-dimensional architecture formation. Obtained reduced graphene oxide hydrogels exhibits a negligible volume shrinkage after assembly, in contrast with the initial GO dispersion volume, differently from hydrogels prepared via other methods. This is mainly due to the catalyzed intermolecular dehydration occurred between the reacting functional groups on the edges or basal planes of the bi-dimensional sheets, that will come together not on the same geometrical plan. The flakes can also be bended and undergo to an intra-molecular reaction. The combination, agglomeration and coalescing due to the strong physical and/or chemical interactions, forming covalent, non-covalent and electrostatic bonds, can result in a dramatically decreased surface area. However, graphene's excellent mechanical properties provide the framework enough mechanical strength to support a weight of a hundred grams with little deformation, while conventional aerogels are usually very weak and thermally unstable due to the fragile supramolecular interactions between their building blocks. These hydrogels can also be cut with a knife. Characterized by a storage modulus between 50 and 500 kPa, which is one order of magnitude higher than its loss modulus, these frameworks have a predominant elastic response when deformed. The hydrogels are characterized by a compressive elastic modulus between 30 and 300 kPa and a compressive yield stress between 3 and 30 kPa, behaving, under compression, as an elastic-plastic foam, phenomenon ascribed to partial break of the interior network due to fractured pore walls and expanded pores (Zhou Y. et al., 2009; Xu Y. et al., 2010).

The residual hydrophilic oxidized groups, due to the incomplete reduction, can entrap water in the structure during self-assembly, which is fundamental, together the hydrophobicity and the cross-links formation, in the successful construction of the hydrogel, which takes on the shape of the containment vessel, usually a cylinder. For the assembly to succeed, the concentration of GO in the dispersion and time need to be sufficiently high, to allow the proper and numerous cross-linking through partial overlapping of the flexible graphene sheets to occur quickly. However, when C_{GO} is low, the bonding would be difficult to occur timely because of the low contacting opportunity between the graphene sheets, leading to a formation of a RGO powder and not a three-dimensional interconnected structure., which cannot form at concentrations lower than 2 mg/mL, that is the concentration that produces the lowest density. There is no shrinkage in the hydrogel compared to the original dispersion volume if the concentration is higher than 3 mg/mL, which leads to an increased density (Hu, H. et al., 2013). Hydrothermal self-assembly fabrication process allows to obtain the lowest densities (2mg/cm^3) among all the preparation methods for 3D graphene structures, like CVD (5 mg/cm^3), template CVD (10 mg/cm^3), sol-gel (15 mg/cm^3), chemical reduction (40 mg/cm^3), room temperature self-assembly (80-100 mg/cm^3) (Zhao, Y. et al., 2012).

The water content ranges between 96%wt and 99%wt, so the hydrogel contains less than 4%wt of graphene sheets: to obtain the aerogel, the water need to be evacuated. During thermal drying, the capillary action caused by the evaporation of water can collapse the pore structure. To avoid the breakdown, lyophilization can be performed, during which the liquid is replaced by gas and removed from the inside, causing a slight volume shrinkage. Limiting the stress on the framework, preserving the interactions between the 2D sheets in the composed hydrogel. Two techniques are the most widely used to obtain a high surface area macroscale sponge: freeze drying and supercritical CO_2 drying. The first technique limit the strain by going around water's triple point boundary, lowering the temperature of water to induce crystallization, to remove the solid phase via low pressure, but the sublimation can break fragile structures made of few graphene layers. Water can be exchanged with acetone, that is washed away with liquid CO_2 supercritical fluid which exhibits its critical point at only 7MPa and 31°C, which compared to the critical point of water is more suitable to avoid as much as possible damages to the porous structures, that can happen with the critical point drying technique, that forming a supercritical fluid at elevated temperature and pressure avoiding any phase boundary. CO_2 is released slowly as gas when the temperature is raised above the critical point, leaving the dry sample with minimal distortion of the gelled structure. Freeze-drying and supercritical CO_2 drying produce differences in the morphology and density of the aerogel, with the CO_2 inducing a higher density, determined by a lower pores total volume (Zhang, X. et al., 2011).

Hydrothermal treatment is widely employed for synthesis and preparation of complex inorganic nanomaterials, like transition metal oxides for functional applications, so it’s the most appropriate process to fabricate RGO composites, dispersing the inorganic on a conductive carbon substrate to form a hybrid in only one step process without requiring any further reaction, allowing the introduction of metal oxides inside the structure to provide properties or improve performances (Xu, R. et al., 2011, Gigot, A. et al., 2016).

The convenient one-step hydrothermal process is simple, scalable, and environmental safe, because the conversion is based on a harmless and cost-effective solvent as water without use of organic solvent. The reduction degree is controlled by time and temperature, so to increase the conversion ratio it is required a longer reaction time or higher temperature. To improve the reduction, noble-metal nanocrystals can be introduced in the system to catalyze the deoxygenation and the following assembly (Tang, Z. et al., 2010), or it can be performed a metal ions-assisted hydrothermal method (Xu, C. et al., 2015). The conversion extent can be tuned with a further chemical reduction or, to not lose the advantage of the single step process, performing a combined hydrothermal-chemical reduction, introducing a reducing agent in the system. As previously discussed above, some crosslinking agents such as EDA can also mildly reduce GO and induce reduction self-assembly at moderate solution temperatures around 95°C, producing robust graphene sponges without shrinkage (Hu H. et al., 2013). Ammonia can be also used to reduce the solution, inducing a basic pH that promotes the RGO dispersion in water (Hu K. et al., 2016). Doping graphene with substituent heteroatoms can effectively modulate the electronic characteristics, surface and local chemical features of graphene. Pyrrole is a swelling agent to prevent the GO self-stacking behavior during assembly, leads to a large inner surface and provides furthermore a N doping (Zhao, Y. et al., 2012). Nitrogen doping is also performed using urea, which is, at the same time, an expansion agent and reducer (Wakeland, et al., 2010) just like dicyandiamide (Zhou, G. et al., 2016). The framework can be S-doped introducing thiosulfate as reducing agent (Yu, M. et al., 2015) or N,Scodoped adding thiourea, which is a doping, expansion and reducing agent (Shin, W. et al., 2015). Boric acid can be employed as boron dopant for the reduced graphene oxide (Zhou, G. et al., 2016). The use of these doping agents, despite introducing heteroatoms to improve the performances, requires a dialysis in deionized water to remove the residuals that can affect the behavior. Most of these agents are also polluting and risky, so to avoid the employment of dangerous chemical species, external catalysts or to avoid the introduction of non-carbon impurities into the treated GO, can be used environmental friendly reducing agents, like sodium ascorbate, which although requires a further dialysis to remove Na (Sheng, K. et al., 2011). To avoid this further cleaning step, natural reducer, only composed of carbon, oxygen and hydrogen can be employed in hydrothermal treatment, like cyclodestrine, which is not thermally stable, chitosan, that requires an acid pH adjustment and provides only nanoporosity, and glucose, that needs a basic pH but forms a 3D interconnected structure and high specific surface (Zhu, C. et al., 2010; Zhang, J. et al., 2010; Ji, C. et al., 2013).

Among the natural C-O-H based reducers. ascorbic acid (AA) also known as Vitamin C, is an edible mild reducing agent with non-toxic properties, fundamental component of a healthy diet in humans as a natural antioxidant because essential for many metabolic functions, and widely employed as a food additive and as a primary “green” reductant in the laboratory, but never in a hydrothermal process. The reduction capability, whose efficiency matches the results obtained by hydrazine, can be used to reduce GO in an aqueous solution even at room temperature (Fernández-Merino, M.J. et al., 2010). The presence of vitamin c in the dispersion enhances the assembly ability, and besides that, the oxidized AA products can act as a capping reagent to stabilize the sheets in solution. Ascorbic acid undergoes a deprotonation in water forming dehydroascorbic acid, which can be further converted into oxalic acid. This converted product can form hydrogen bonds with the residual peripheral carboxylic groups on the reduced GO surface edges, disrupting the stacking between the sheets, preventing agglomeration (Zhang, J. et al., 2010).

Reduction with vitamin C can be made not only in water, but also in some common organic solvents, such as DMF and NMP. vitamin C represents an ideal, natural, green and safe substitute, which does introduce no risks to the human health or to the environment, for hydrazine in the large-scale production of water-produced graphene (Fernández-Merino, M.J. et al., 2010). The reduction with AA is usually performed at a temperature below 100°C for long time (4-16h) without stirring, and results in an absence of gaseous products during the formation of the hydrogel precursor (Zhang, X. et al., 2012). The acid molecule releases in water two protons that can protonate the carboxyl groups on the basal plane due to their affinity with oxygen, weakening the repulsive force between sheets and water, making the

GO become less stable solution. During hydrogelation, most of the thermally labile oxygen functional groups are chemically removed by vitamin C, restoring most of the conjugated bonds through dehydration. The reduction that involves a gradual hydride transfer from the 5-membered ring of the molecule to either the epoxy or hydroxyl groups of yielding water molecules upon heating as opposed to gases produced by other reduction methods. AA reduction is an effective method to obtain RGO aerogels with density between 0.03 and 0.08 g/m^3, a SSA between 200 and 500 m^2/g and a conductivity ranging from 60 to 800 S/m, which is comparable with results obtained with hydrazine reduction and more than two orders of magnitude greater than those reported for macroscopic physically cross-linked three-dimensional graphene networks prepared without any reducing agent. The reduction capability of AA can be improved increasing its concentration in solution, or adding HCl to purposely lower the pH value for speeding up the reaction, shortening the gelation time of the dispersion (Dua, V. et al., 2010; Fernández-Merino, M.J. et al., 2010; Zhang, J. et al., 2010; Zhang, X. et al., 2011).

Vitamin C does not need any pH adjustment in the already acid GO solution (Dimiev, A. et al., 2012), like other natural reducing agents, because determines itself the pH on the base of its concentration, that also controls the conversion degree of the RGO. The protons introduced by the ascorbic acid can work simultaneously with the H_3O^+ derived from the self-ionized supercritical water, so the combination of two green and harmless reduction processes like AA chemical deoxygenation and hydrothermal treatment can be convenient in terms of results, efficiency and morphology control, due to the excellent performances of both techniques.

In conclusion, from a practical point of view, this method is limited by equipment and is time-consuming and requires relatively high temperature, even if allow to produce big batches of material. The sealed autoclave need to be heated up to 180°C to produce internal autogenous high pressure that induces the self-assembly, which will be more efficient with longer time of reactions. There is no direct control on the temperature, so the system can be considered static, because will slowly change due to the heating mechanism (convection in the furnace air), so there cannot be a timely change in intrinsic parameters, so there is no immediate control on the degree of reduction, that can be increased only performing the heating for longer time. Internal temperature and pressure can be measure with an autoclave with a pressure gauge and a thermometer, but this will strongly increase the container dimensions, and thus the required dimensions of the furnace, introducing an effect on the heat distribution.

The slow process is also due to the inhomogeneous heating of the inner vessel volume: the external jacket will be quickly heated on the outer part, that will heat up the thermally insulating PTFE liner inside, which, in turn, will heat up the dispersion contained inside. The heating and cooling ramps will be slow, due to the lower thermal conduction of the composed autoclave, which will also make impossible a real-time imaging or in-situ characterization of the reaction due to the non-transparency of stainless steel and PTFE.

3.3.2. Microwave-Assisted Hydrothermal Synthesis

The hydrothermal treatment can be performed, instead of the conventional thermal mechanism, with a microwave irradiation as heating source of the liquid medium to reach HP-HT conditions, in order to accelerate the reaction and, therefore, reduce the processing time. All the considerations made in the previous paragraph about conventional hydrothermal treatment are still valid, except for the reaction container, the required instruments and the parameters control.

Microwave radiation is localized in the in the frequency range 0.3 to 300 GHz on the electromagnetic spectrum, corresponding to wavelengths from 1 mm to1 m, but all domestic ovens and all dedicated microwave reactors for chemical synthesis operate at a frequency of 2.45 GHz (corresponding to a wavelength of 12.25 cm). The major advantages in using this inexpensive, quick, versatile MW technique is a rate enhancement of the reaction due to the more effective and localized heating mechanism and parameters tuning, that can decrease the required time from several hours to few minutes or even seconds, leading to a minimization of unwanted side reactions, resulting in an increased yield of reaction and an improved purity due to less formed byproducts. The homogeneous microwave field and exact temperature control guarantee great reproducibility, with comparable results for every experimental run, and allow to expand the reaction conditions, accessing to transformations that would not otherwise be easily attainable and achievable with conventional techniques (Cao W., 2012).

The first MW-assisted reactions employed simple, modified domestic microwave ovens without any parameter control, the use of these instruments was not only dangerous but also sometimes led to irreproducible results. Dedicated microwave reactors have been developed, combining rapid in-core heating with sealed-vessel (autoclave) conditions and real-time *in-situ* monitoring and accurate measurements of process parameters, thanks to precise temperature sensors and sensitive pressure gauges, to satisfy the need for precise reaction control, which allows to reach elevated pressure easily than conventional heating methods. Reactors usually control the reaction evolution through a continuous power regulation, with a magnetic or mechanical (magnetic induced) stirring of the mixture and a uniform post-reaction cooling. The reactor consists of a power source, called magnetron, a line for the transmission of the MW radiation, the waveguide, into the resonant cavity, which surrounds the reaction vessel. The geometry and dimension of the cavity determine the number of existing modes, distinguishing between single-mode or multi-mode reactors, with the main difference in the reaction scale, with the single-mode suitable for small scales, while the multi-mode is recommended for big volumes at low power density, and is the typical mode of domestic MW ovens. In multi-mode, microwaves are reflected from the walls of the cavity, thus interacting with the sample in a chaotic manner, while in single–mode circular cavities is generated a homogeneous energy field of high power intensity that enables excellent reproducibility, with the sample located at the maximum energy point (Kappe, O. et al., 2009).

Microwave irradiation induces a dielectric heating in a polar solvent from the bulk towards the external walls, whose effect is dependent on the ability to absorb microwave energy and convert it into heat through a dipolar polarization mechanism. The dipole moment that will align to the applied oscillating electric field, and the MW frequency enables the movement of the molecular dipole, giving the time to align in the field but not to accommodate and realign to the alternating field timely, so the oscillation will result in a molecular friction and dielectric loss that will generate heat. MW electrical energy is transferred to the medium and converted into kinetic and thermal energy, then into heat. The ability of the polar solvent to convert electromagnetic energy into heat at a given frequency and temperature is defined by the parameter tanδ, expressed as the ratio between the dielectric loss, the efficiency of conversion into heat, and dielectric constant, the polarizability of molecules: a reaction medium with high tanδ will have efficient absorption and, thus, rapid heating. However, the penetration depth is inversely proportional to tanδ and, with increasing temperature, the dielectric loss of and then the absorption, decreases while the penetration depth increases. The tanδ is also a parameter to choose the most suitable non-polar microwave transparent (low absorbing) material to fabricate the reaction vessel, like Pyrex or Teflon, which exhibit limited interactions with microwaves (tan d < 0.01), which means that the material is heated up only by conduction of the solvent inside without producing any MW efficiency loss, and have a penetration depth of the order of meters (Kappe, O. et al., 2009).

De-ionized pure water, the typical hydrothermal reaction medium, is a polar liquid with medium microwave absorbance penetration depth of the order of a few centimeters at room temperature, so is a suitable compromise between not excellent absorption and a heating involving almost the whole internal vessel volume. MWs can be used to perform reactions in aqueous solutions below 100°C, but is also possible achieve the superheated status in a closed sealed vessel, to suitably modify physical and chemical properties of water thanks to HT-HP conditions. The microwave irradiation heats up easily water from 25°C to 100°C, while is more difficult heat water to 200°C in a sealed vessel, because near-critical and supercritical water is transparent to MWs, because the tanδ is lowered due the drastic decrease in the dielectric constant with temperature increase. This problem can be solved adding microwave absorbing inorganic salts or metal catalyst substrates (Cao, W., 2012).

Thermal heating by convection and microwave dielectric heating and are completely different mechanisms. Conventional hydrothermal synthesis is carried out by slow and inefficient conductive heating from an external heat source. The energy is transferred into the system through convection, and the heating efficiency depends on the thermal conductivity of the constituting materials of the autoclave, resulting in a temperature of the reaction vessel higher than the temperature of the reaction mixture inside, with a probable and unwanted temperature gradient, causing local overheating of the sample that can lead to inhomogeneities, decomposition and non-reproducibility. MWs provide an efficient internal core heating by directly exciting the molecules of solvents, reagents and catalysts, causing friction and dielectric loss, raising the temperature of the whole volume simultaneously through a bulk heating. Another important difference between HS and MAHS is the order of heating, with the conventional thermal process that heats up the vessel walls first and then the solution closer to these, since the MW vessel are made out of microwave nearly transparent materials, the radiation passes through the walls and an inverted temperature gradient as compared to conventional thermal heating results, with the vessel heated last by the solution, with a uniform temperature variation throughout the sample bulk (Kappe et al., 2009).

The microwave–assisted reaction enhancement and boost is due to a combination of different contributions. The thermal effects contribution is due to the achievement of high reaction temperatures and superheated water thanks to MW-dipole interactions. Temperature jumps of 200°C can be performed within few seconds, and a similar temperature profile is impossible to reproduce in a hydrothermal or simply thermal system. At the end of the irradiation, another steep jump of temperature is performed due to the rapid nitrogen jet cooling of the mixture to a temperature around 50°C, to remove the vessel from the cavity in a short time, unlike the conventional heating, where there is no forced cooling phase. Rapid heating and cooling typical of small scale microwave-assisted hydrothermal synthesis, and they can lead to different reaction products, sometimes leading to less by-products compared to the traditional hydrothermal processes. Another contribution is due to specific microwave effects, that induce an acceleration in the thermally-related chemical conversion, due to the electromagnetic field and not reproducible with conventional heating. One of these effects is the superheating of the solvent above its atmospheric boiling point, due to the involvement of the whole solvent volume in the heating process, after which the excessive thermal energy will be lost only at the liquid-gas interface, in contrast to a thermally heated solvent where nucleation of bubbles occurs at defects on the inners vessel surface. This efficient internal heat transfer to the whole bulk induces an inverted temperature gradient and results in a minimization of the hot wall effect because not heated by the MWs, which leads to a diminished catalyst deactivation, due to higher temperature of the vessel in conventional thermal heating, leading to a better conversion in microwave-assisted synthesis. Non-thermal microwave effects are the last contribution to the reaction kinetic enhancement., with an acceleration of chemical conversions in a microwave field that are not thermal or specific microwave effects (Kappe et al., 2009).

To the conventional thermal reaction conditions of temperature and time, the use of microwaves introduces the irradiation output power as third variable. The power is the most important parameter, because can optimize T and t of the reaction thanks to several ramping holding steps without intermediate cooling, with a possibility of translating conventional conditions into microwave conditions according to the Arrhenius equation. Temperature is indirectly controlled tuning the power of the microwaves, that also controls both ramp time and hold time, which are fundamental for the success of the reaction. The recommended power values are 50 W for high absorbing, 125 W for medium absorbing and 200 W for poor absorbing solvents. The temperature is measured by a calibrated external infrared (IR) sensor, integrated into the bottom of the cavity, that detects from a fixed distance the outside surface temperature of the reaction vessel, assumed to roughly the temperature of the reaction mixture contained inside, even if the reactor wall is typically the coldest spot of the system due to the inverted temperature gradient. External temperature sensor cannot be used in conjunction with simultaneous cooling of the vessel because the internal temperature of the mixture will be higher, also because the temperature detection is delayed of a few seconds. However, the external compressed gas cooling prevents excessive overheating by continuously removing latent heat. The MW-assisted hydrothermal reaction need to be performed in a closed sealed vessel to reach the autogenic elevated internal pressure, due to superheating of the solvent, above the atmospheric pressure to create the hydrothermal conditions, which results in a reduced reaction times and improved yields. The pressure is strictly dependent, as in conventional autoclaves, to the filling volume of the vessel, with the maximum determined to leave enough headspace for pressure build-up, to avoid the abortion of the experiment due to exceeding the pressure limits, usually 20 bar, which can be partially released by a ventilation system (Kappe, O. et al., 2009).

The reaction monitoring in a closed sealed system is hard to perform during the run, especially the analysis of the gaseous products evolved, because is only possible after interrupting the reaction, cooling and opening the vessel if there are no outlets in the sealing system. If the reaction is carried out in a Pyrex vessel, is possible to interface an instrument to perform an *in-situ* characterization, like a Raman spectroscopy to follow the reaction evolution. Similarly, is also possible a visual follow up the reaction through a built-in camera for in situ reaction monitoring (Bowman, M.D., et al., 2008).

Microwave-assisted hydrothermal reaction has been used to fabricate mainly inorganic functional compounds, like small metal clusters for catalytic activity, phase-controlled TiO2, 1D, 2D and 3D ZnO structures and its salts, MnO_2, whose phases can be interchanged increasing the reaction time, Mn_3O_4, Fe2O3, SnO2, Co3O4, MoO_2, MoO3, MoS_2 (Xiang, Q. et al., 2011; Lv, T. et al., 2011, Cao, W., 2012; Li, L. et al., 2012; Liu, C.-L. et al., 2012; Li, J.L. et al., 2014; Qin, Wang Y. 2014; W. et al., 2015)

Microwave irradiation has been used to increase the reduction degree, after conventional hydrothermal process, with a further treatment in vacuum (Hu, H. et al., 2013) or in an inert atmosphere containing H_2 as reducing agent (Park, S.-H. et al., 2011). The reduction induced self-assembly of 3D RGO aerogels through microwave-assisted hydrothermal synthesis is usually carried out at higher temperature than HS and for lower times, exploiting the ability to reach the temperature quickly, thanks to dielectric heating, with a simultaneous increase in internal pressure. The rapid absorption of microwave radiation by GO in polar solvents with a subsequent increase in temperature and pressure inside the sealed reaction vessel facilitate the conversion to RGO, exploiting supercritical water which act as reducing agents under the hydrothermal condition (Murugan A. et al., 2010). A lot of paper use household microwave ovens to perform the reduction, without performing a direct and refined control on the reaction parameter adding reducing agents like dimethylacetamide to try to tune the extent of conversion (Chen, W., et al., 2010), performing a multi-step reduction, introducing in between the stages molecules and monomers to graft on the surface(Long J. et al., 2011) or direct irradiation of GO powder for 1 min in Ar environment (Vermisoglou, E.C. et al., 2015) of a mixture of GO/graphite to control the reduction degree (Hu H., et al., 2012). The addition of nitric and sulfuric acid in the solution mix allows to perform a S/N cooping using reactions with functional groups on the GO sheets (Choi, B.G. et al., 2010). Among the synthesis performed with microwave reactors, the most common reaction to form a RGO aerogel or its hybrids is carried out at a temperature between 150°C and 180°C for 10-60 min, usually followed by a thermal drying in vacuum at 60°C (Xiang, Q. et al., 2011; Lv, T. et al., 2011). In addition to metal oxides hybrids, it can be fabricated a composite with noble metals (Wang, Y. et al., 2014) or perform a N-doping adding, as in the conventional hydrothermal treatment, urea as reducing/expansion agent (Yang J. et al., 2014).

4. Materials synthesis and characterization

4.1. *Material synthesis*

The starting material, single layer graphene oxide powder, prepared by modified Hummers' method, was purchased from CheapTubes Inc, USA. The lateral dimension of the flakes is around 300-800 ± 0.2 nm, while the thickness, measured by Atomic Force Microscope, ranges between 0.7 and 1.2 ± 0.2 nm (fig. 4.1). The declared purity of the purchased pristine material is 99wt%, with an elemental composition, depending on the amount of permanganate used, is C: 35-42%, O: 45-55%, H: 3-5% (from cheaptubes.com). Dry graphene oxide powder is received in the form of woolly and soft irregular flakes (fig 4.2a).

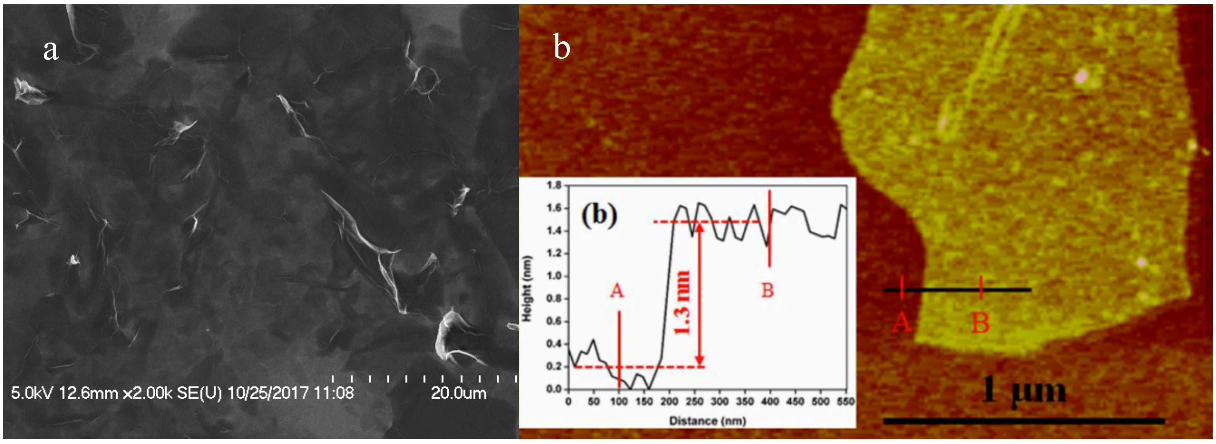

Figure 4.1: a) Scanning Emission Microscope image and b) Atomic Force Microscope micrograph of GO flakes on silicon (*AFM image from Cheng, Y. et al., 2017*)

The RGO aerogels are obtained by means of a double step procedure, consisting in a hydrothermal reduction (conventional or microwave assisted) followed by the elimination of the solvent through freeze-drying process (lyophilization). Both reductions have been carried out using only water as solvent and reducing agent with the addition of ascorbic acid (purchased from Sigma Aldrich) in the suspension to tune and control the reduction degree (Ji, C.C. et al., 2013). Both reagents were used without further purification.

For conventional hydrothermal treatment, the GO powder was dispersed in de-ionized (DI) water (Merck Millipore Milli-Q). For a succesful self-assembly of an aerogel with the lowest density, the dispersion had a GO concentration of 2 mg/mL, to allow the proper and numerous cross-linking through partial overlapping of the flexible graphene sheets to occur quickly (Hu H. et al., 2013). In a typical procedure, in 17 mL of DI water are dispersed 34 mg of graphene oxide powder and 17 mg of ascorbic acid. The amount of AA has been determined on the basis of previously obtained BET specific surface area results later discussed. The mixture was put in a 20mL vial, shaken thoroughly with circular movements for 1 minute and then left to rest for 5 hours to allow the proper wetting of the GO agglomerated flakes, to initially promote the disaggregation of the clusters (fig. 4.2b). After rest, the aqueous dispersion was ultrasonicated for 30 min, to continue the disaggregation, obtaining a homogeneous brown dispersion (fig. 4.3c), immediately transferred in a PTFE cylindrical 20 mL vessel, contained in stainless steel autoclave (fig 4.4a and b, Parr 4749 General Purpose Vessel). The sonication time is enough to destroy the agglomerates and reach a satisfying hydrophilic GO disaggregation without excessively heating the mixture, to avoid the early start of the reduction reaction, that can take place also at room temperature (Zhang, J. et al., 2010). The volume of the solution grant enough free space for the autogenous pressure to rise (filling 74%), generating the HT-HP hydrothermal conditions.

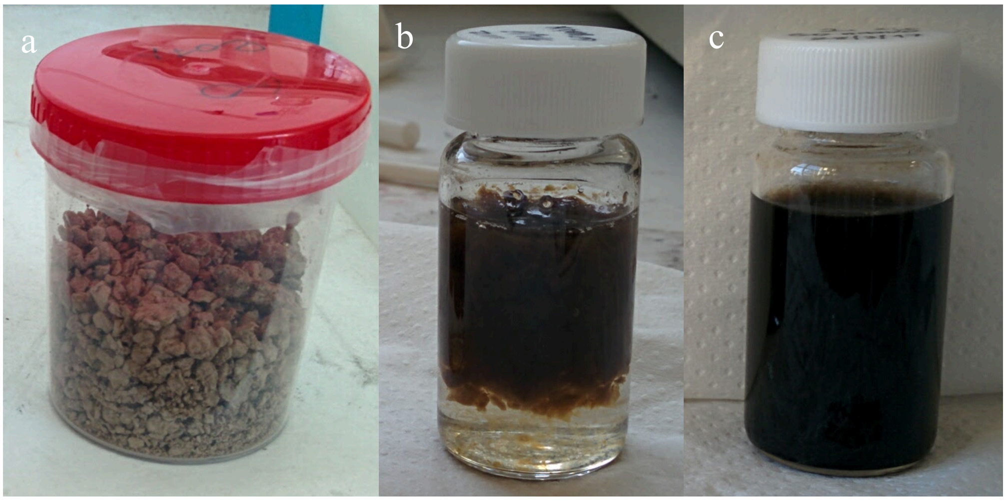

Figure 4.2: a) Pristine as-received dry graphene oxide powder b) GO dispersion after shaking c) GO dispersion after sonication

The teflon-lined autoclave contining the sonicated suspension was later quickly transferred into a muffle oven (Nabertherm burnout muffle furnace L 3/12, fig 4.4c) mantained at a temperature of 180°C to carry our the reduction reaction for 12 hours (Gigot, A. et al., 2016). The insertion of the autoclave in the furnace was done during heating ramp of the oven (150°C/h) at an intermediate temperature of ~100°C to not subtract part of the hold time at the reaction temperature if introduced at 180°C. It was also done to not loose the advantage induced by the sonication with precipitation and agglomeration of the flakes if transferred inside at room temperature, because it makes impossible the reaction to complete properly, resulting in a non-properly assembled hydrogel.

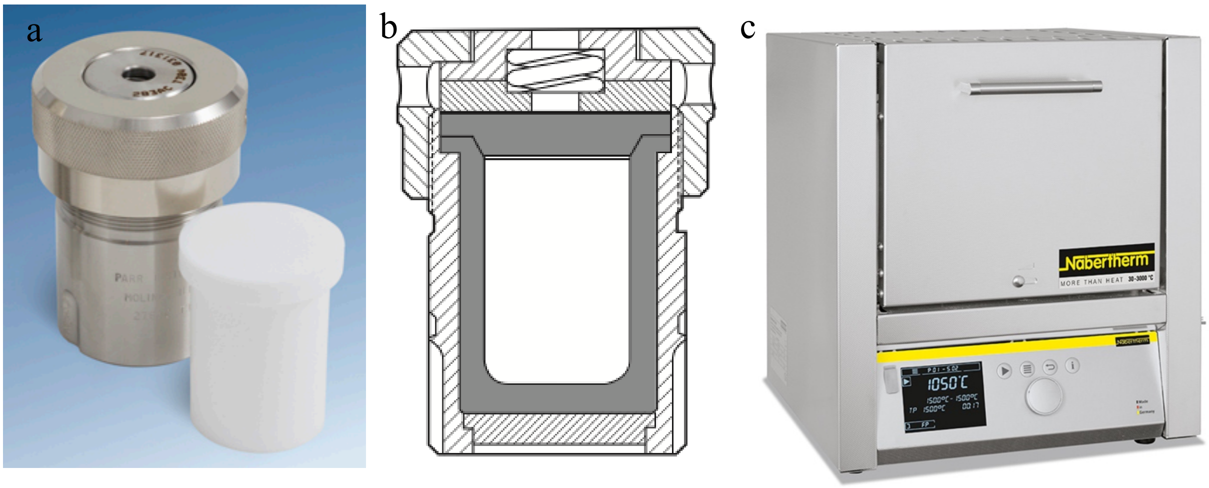

Figure 4.3: a) stainless steel autoclave with PTFE internal liner b) cross section of the assembled, closed and sealed system c) muffle furnace (*from ww.parr.com and www.nabertherm.com*)

After natural cooling to room temperature, the autoclave was opened and the remaining "clean" water around the floating hydrogel (indicator of complete reaction and good reduction) was removed with a pipette. The black cylindrical hydrogel, conforms with the vessel shrinked inner shape, (fig 4.4) was then transferred slowly and gently from the PTFE vessel inside a Falcon 50mL conical centrifuge tube turning the vessel upside down on the tube to avoid the need of touching it with a pair of tweezers to take it out. The obtained reduced graphene oxide could be esily redispersed by ultrasonification if immersed again in water. The obtained sample was frozen at −196 °C immersing the tube, with the lid on, in liquid nitrogen, without previous purification through washing with distilled water to remove low molecular weight components like vitamin C oxidized products. To obtain the aerogel to characterize and use, the frozen hydrogel was then freeze-dried overnight at −55 °C under vacuum (10^{-3} mbar with 5 Pascal LIO−5P DIGITAL lyophilizer) to remove the solvent water from internal pores by sublimation.

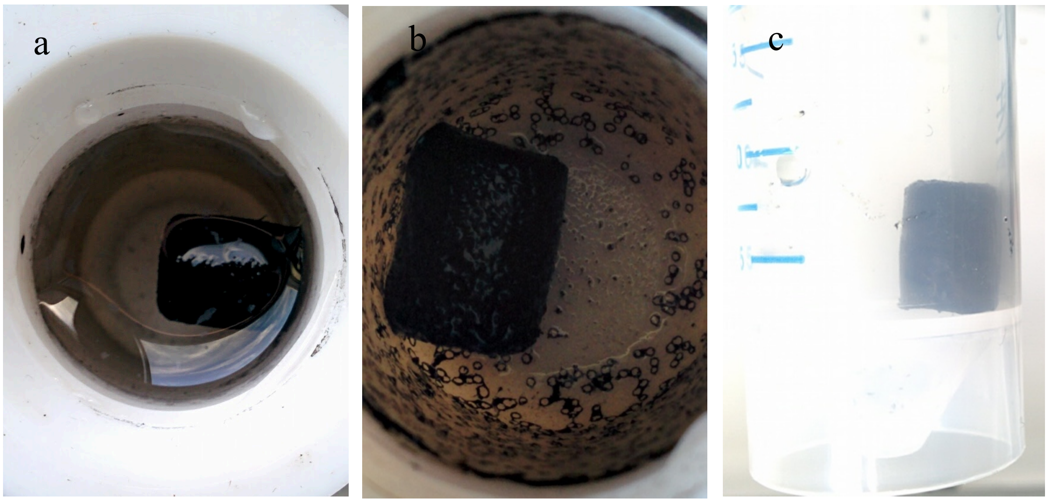

Figure 4.4: Hydrogel obtained by conventional hydrothermal treatment a) after reaction b) after water removal c) after transfer in the tube

Microwave-assisted hydrothermal synthesis shared with the conventional process the dispersion preparation and concentrations, sonication time and the freeze-drying of the hydrogel, which was performed overnight with a LabConco 4.5L Freeze-Dry lyophilizer, (not equipped with a cooling system). The difference is in the heating system, which also determines the employed mixture volume. The MA-HS was performed with a CEM Discover S-class MW reactor with 10 ml Pyrex reaction vessels (fig. 4.5a and b), whose volume is filled at 50% by 4 mL of dispersion. A larger filling is impossible with small glass vials because of the smaller diameter of the vial compared to the PTFE liner, the faster heating process (50°C/min) and the closed but not completely sealed condition that makes the pressure rise rapidly. The closed and sealed system can be obtained employing PTFE autoclaves and internal liners. After sonication, the mixture is promptly transferred into the vessel, onto which is put the snap-on cap, and immediately introduced inside the reactor cavity to start the reaction without letting the GO precipitate. After completion, the vessels is cooled down, extracted from the cavity and opened, water is removed and the prolate spheroidal hydrogel, shape that recalls the inner volume of the vials, is taken out in the same way as the conventional hydrothermal process (fig. 4.5c and d).

As said in the last paragraph of the previous chapter, microwave-assisted reaction has several advantages and few disadvantages compared with thermal hydrothermal process. The main drawbacks of the instrument used are the small batches of material produced every run and the limited pressure attainable mainly related to the specific device used, because the single-mode reactor is intended to be used mainly for small-scale synthesis for research purpose, and cannot be run more than one synthesis every 3 hours due to heating problems of the instrument caused by the long reaction time. The main benefits are the whole mixture volume heating, thanks to the circular cavity which enables a fast ramp and an homogeneous temperature. The configuration and design allows the sample to receive the optimum amount of energy regardless of the reaction volume. With a household microwave oven it is not possible to monitor the reaction key parameters, and they are also unsafe because they cannot neither control or limit the maximum dispensed power and are not design and built to to withstand a possible vessel failure. A scientific microwave device is safer because provide the possibility to determine and a very accurate monitoring of power, temperature and pressure, posing a maximum limit to them, and its cavity is built to bare vessel failures and overheatings. In particular, CEM discover S-class MW reactor is maximized to continuously deliver an output power between 0 and 300 W, with a temperature limit of 300°C and a pressure peak in the sealed vessel of 300 psi (20,69 bar). All the parameters can be controlled and monitored by a software run on a PC interfaced with the instrument. The temperature is measured by IR sensor positioned below the vessel at the bottom of the cavity, which allows an accurate control of the evolving reaction using minimum amounts of solution. The instrument incorporates a fully automated pressure control system, called IntelliVent™, which does not directly measure the internal pressure, but uses a load cell, which senses changes in the external deflection of the septa on top of the sealed vessel applied by snap-on cap for an indirect measurement of the pressure. This management system possesses the additional feature to allow a controlled venting to reduce the pressure in the vial if exceeds 20 bar and subsequently automatically reseal the vessel to maintain optimum safe conditions, thanks to the cap design. The limitation in the reached pressure may be obviated by using a sealed teflon autoclave, which has the intrinsic disadvantage to not allow a prompt pressure control and evaluation.

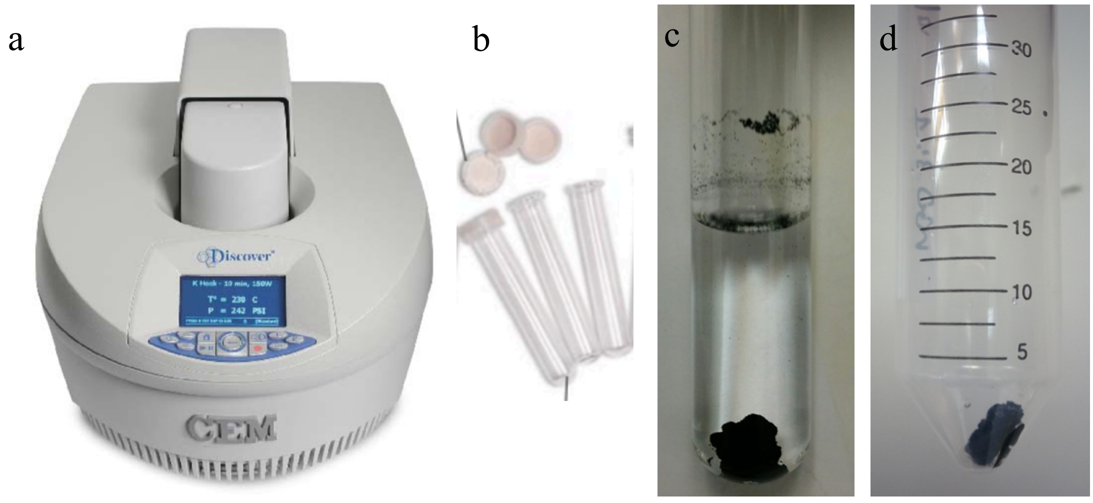

Figure 4.5: a) Microwave reactor b) 10 mL reaction vessel with snap-on caps and hydrogel obtained with MW-assisted hydrothermal treatment b) after reaction d) after transfer in the tube (*images a and b from www.cem.com*)

Pressure and temperature are indirectly controlled by the output power: to lower or raise the temperature or the pression, the MW power can be reduced or increased. The reduction reaction was carried out at 180°C for 1h and no stirring (Xiang, Q. et al., 2011, Li, L. et al., 2012), with a heating ramp of 5 min, limiting the power at a maximum of 200W (recommended value for poor absorbing solvents). The temperature was increased and mantained constant by a variable power between 0 and 200W, sufficient for the desired rapid heating (fig. 4.6). With constant power was impossible to reach the required temperature or to maintain it stable. The pressure limit was set at 200 psi (13,79 bar) for conservative sfety reasons, and the mixture reached the maximum pressure before reaching the target temperature, so the system had to temporary lower automatically the output power to lower the pressure, also released by the venting system, and allow the mixture to increase its temperature.This effect is emphasized at higher powers, so 200 W was the lower value to allow the reaching of the destination temperature rapidly. Despite the high reproducibility ensured by the microwave synthesis, there has been a a different behavior between the same synthesis. The most common behavior can be seen in figure 4.6: the pressure, after an initial constant period of around 10 minutes, generally slowly dimineshed, allowing the power to be constant in a limited range. However, sometimes happened, without any particular reason, correlation or repetitive condition, that the pressure remained constant at the maximum pressure level, oscillating around this value, for most of the reaction and then slightly decreasing during the final period or not decreasing at all, resulting in a discontinuos power administration. This different behaviors never resulted in any kind of difference in the samples. After completion, the vessel was cooled down by an automatical nitrogen jet stream blown on the bottom, and then released from the system at 50°C to be able to be handled.

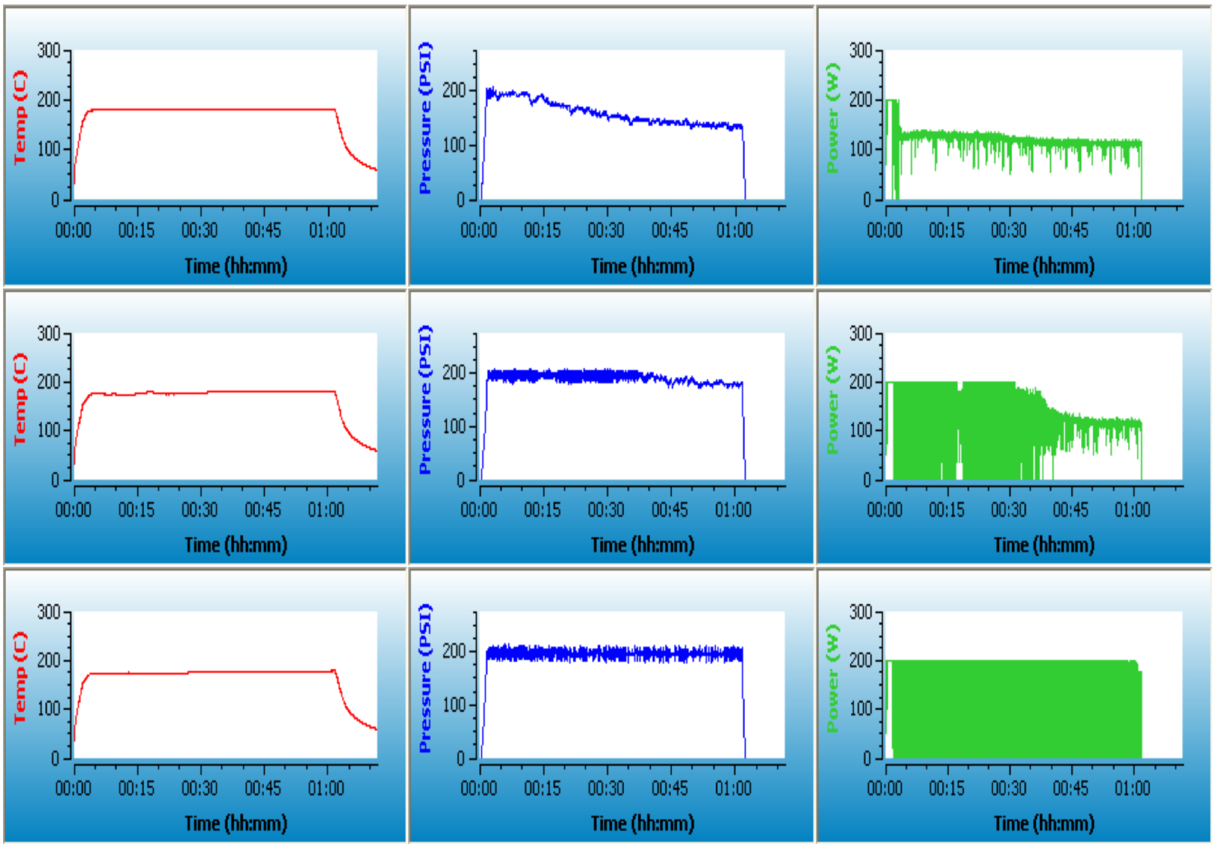

Figure 4.6: Parameters monitoring during reaction: a) decreasing pressure b) constant and then slightly decreasing pressure c) constant pressure during the whole reaction

Lower reaction temperatures were tested, but it took place only the reduction without self-assembly of the 3D network, as confirmed by the black color of the resulting mixture, containing well-dispersed RGO which did not precipitated after long time, and the absence of the hydrogel. Higher powers, and thus higher temperatures, were impossible to reach due to pressure limitations.

The most interesting tool of the MW-assisted synthesis apparatus is the *in-situ* real-time reaction monitoring performed by means of an integrated CCD camera interfaced with the cavity. This feature is useful to understand the macroscopic effects as reaction proceeds, following the changes in the system like colors, viscosity and bubbles formation, and is permitted by the use of the pyrex vessel, tough it lowers the maximum achievable pressure. The possibility of an accurate parameters control and monitoring, together with the ability to see a reaction as it runs, is the main distinction with the conventional hydrothermal synthesis. The camera was positioned outside the instrument wall, overlooking the vessel, illuminated from white light LEDs placed in the bottom, through an access port on the side of the cavity, with the lens protected by a transparent plastic cover in case of vessel failure. Reactions performed were digitally recorded thanks to a connection with the controlling PC.

From the obtained video feed (fig. 4.7) and parameters monitoring was possible to follow up the reaction to understand the macroscopic assembly behavior of the heated GO dispersion. Initially the solution had a dark brown color, which became lighter with the evolving of the reaction. After 20 minutes, the solution slowly turned to a light brown/grey color, and the first flakes of big dimension can be seen on the bottom of the vessel. These flakes did not evolve in the remaining part of the reaction. At the same time was possible to catch a glimpse of the forming hydrogel located below the water level. After 30 minutes the solution had almost completely lost color, big black flakes appeared, moving together the convection fluxes inside the solution. These flake increased in dimension and size and decreased in number during the running reaction, so it could be deduced that the growth took place on more than one seed, and the aggregation was exponential until the flakes, eventually, coalesced between them or with the hydrogel, or joined the precipitate on the bottom. In the last 10 minutes there was almost no evolution in the flakes dimension and movement. When the cooling jet stream began, the flakes from the bottom started to move cahotically, while the hydrogel kept floating like it did during the whole reaction time. At the end of the cooling, the hydrogel fell slowly on the bottom of the vessel, unlike in the conventional HS, where the hydrogel floated at the water surface because of the buoyancy of the gas bubbles containing mainly CO_2 embedded in it (Wu, S. et al., 2016). The flakes on the bottom, once removed the hydrogel, were too few and small to be recovered in a sufficient quantity to be analyzed, expecially to obtain informations about their porosity and morphology, which is supposedly the main difference with the 3D structure.

4.2. Samples preparation for characterization

The freeze-dried aerogels, highly electrostatic, were broken into small pieces with a spatula to expose their interior surfaces to be analyzed with a SEM. The obtained powder was then dispersed and pressed on a piece of conductive carbon tape, which was afterwards gently blown to remove any volatile residue. Part of the powder was then coated with a thin conductive layer (~10 nm, platinum), the remaining was kept as-synthesized and introduced in the microscope without any further coating or treatment. Same process was employed to prepare the GO for the analysis. The samples still retained excessive electrostatic charge to perform a high resolution imaging of the surface, for this reason the powder was mixed with a drop of conductive liquid silver paint (Agar Scientific), let it dry on a piece of silicon wafer, and then coated with platinum. Specific surface analysis requires large amount of sample to analyze (it is required at least an amount of material that provides a minimum specific surface area of 5 m^2/g). The SSA was conservatively hypotized to be around 300 m^2/g, as observed in previous studies (Gigot, A. et al., 2016), so the required minimum mass is 16,6 mg. 20,3 mg of aerogel produced with hydrothermal method and 26,2 mg of material obtained with MW-assisted method were placed inside the testing tubes and connected to the degassing lines. To perform XRD analysis, 3 mg of GO and RGO powder was dispersed in 1 mL of isopropanol, sonicated for 10 minutes and then let it dry at room temperature for 24 hours inside an hollowed cylinder (10 mm diameter) placed on a glass slide. FT-IR samples were prepared with the same procedure, but instead of a glass slide were used potassium bromide windows, because almost transparent to IR radiation, except for GO that was obtained in the form of a free-standing membrane. Raman spectroscopy samples were prepared placing the different powders on a piece of silicon and placing a drop of ethanol on it, which will be almost immediately evaporated. The sample for XPS need to be free from contaminations as much as possible, so the powders were broken inside the tubes with a clean spatula and transferred on a conductive copper tape, placed on a piece of Si wafer, without being pressed. The Si is then turned upside down and gently shaken to remove all the powder not attached on the adhesive surface. The powder was carefully grounded to ensure sufficient diffusion of heat during the thermogravimetical analalysis.

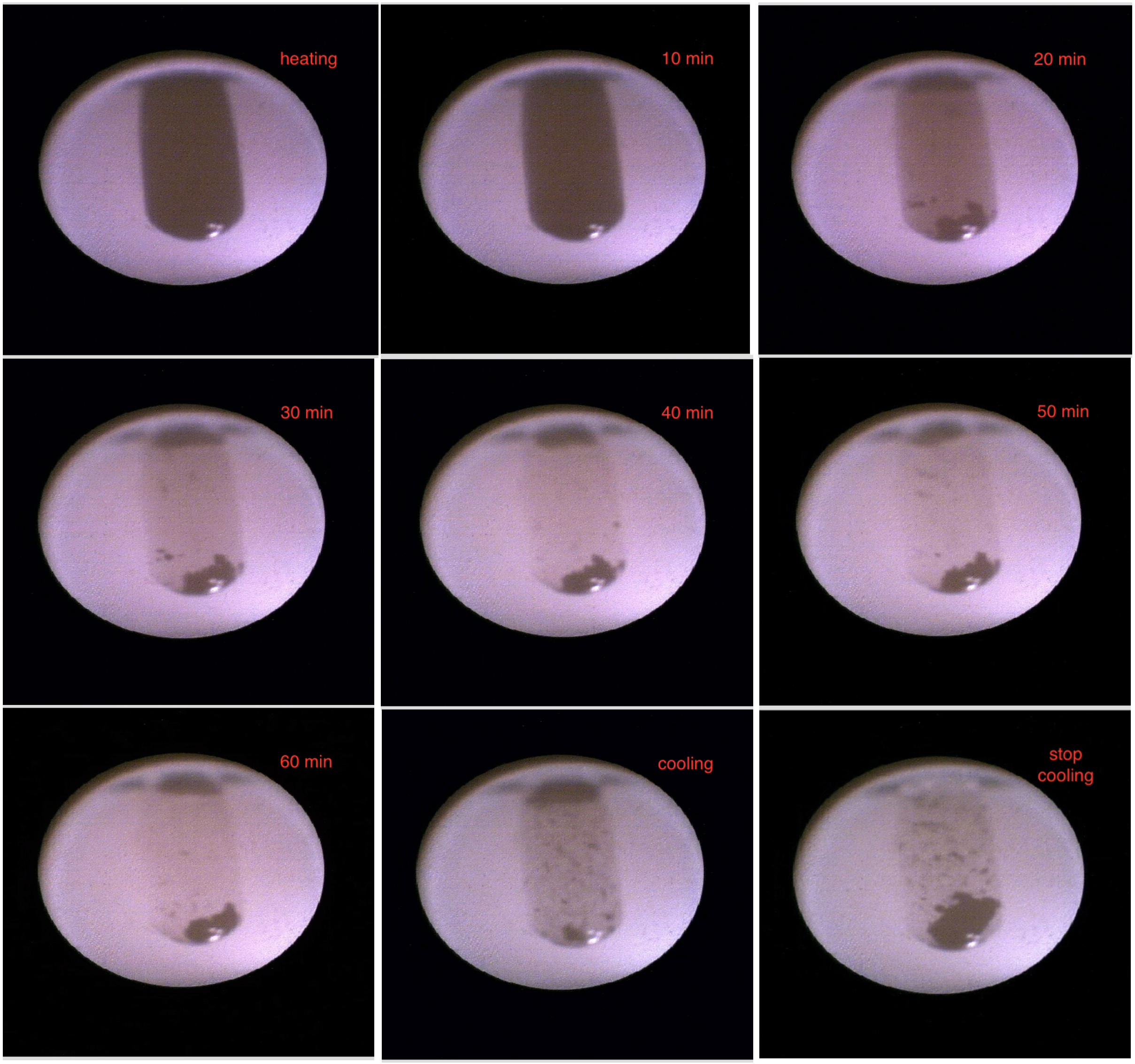

Figure 4.7: Screenshots at different times of the in-situ real time video of the running reaction

4.3. Materials characterization

The successful completion of the reaction could be immediately determined by visual confirmation of the presence of the assembled hydrogel inside the reaction vessel in both synthesis. We also tested mixtures containing only DI water and GO, without any reducing agent. The reduction took place, because, during the process, the brown color of the starting dispersion turned into black at the end of the reaction, which was an instant indication of deoxygenation of GO into RGO, but there was no self-assembly resulting in a hydrogel in neither of both synthesis techniques. Sometimes were obtained gelatinous precipitates containing all the water in HS, while MAHS resulted in a small principle of sol-gel aggregation immersed in a reduced graphene oxide black solution. These results may be imputable to a non sufficient purity of the water, which needs to be ultrapure to act as reducing agent. The self-assembly of the hydrogel in the MW-assisted method is also unabled by the stirring of the mixture, which allows a more homogenoeous heating of the solution but produces a black powder that precipitates at the bottom of the vessel due to the low solubility in superheated water under hydrothermal conditions.

The characterizations performed on pristine graphene oxide go under the label of “GO”, those performed on aerogels obtained by conventional hydrothermal synthesis are “HT-RGO”, while “MW-RGO” are the analysis made on the material produced with microwave-assisted hydrothermal treatment.

4.3.1. Physical characterization

Scanning Electron Microscopy

The morphology and microstructure of the resulting free-standing RGO aerogels were investigated and characterized through scanning electron microscopy observation with a field emission gun-scanning electron microscope, operated at a voltage of 5kV (Zeiss Supra 40 (Germany) for HT-RGO samples and Hitachi S-4700 (Japan) for GO and MW-RGO samples).

HT-RGO (fig. 4.8 left) showed a well-defined and branched 3D network, consisting in a uniform foam-like structure with a hierarchical and interconnected large-scale open pores as previously reported for hydrothermal reductions (Xu, Y. et al., 2010; Gigot, A. et al., 2016) but also for ascorbic acid reduction at room temperature (Zhang, X. et al., 2011). The aerogel was characterized by wrinkled and folded planar regions, due to the randomly oriented and assembled graphene sheets, and a wide size range porosity (diameters varied from nanometers to several micrometers) enclosed in the framework. The scrolled and crumpled graphene with open porosity was characteristic also of MW-RGO sample (fig 4.8 right), which although had a more coarse and irregular structure, compared to the assembled-leaflets architecture obtained by hydrothermal treatment. The curled up RGO flakes derived by the overlapping and coalescing of flexible GO sheets, which formed physical and chemical bindings between them. The rippled and curled texture of both structures were due to the strain introduced during the reaction in the stiff but flexible constituting 2D elements. The violent and drastic reaction induced by the microwave irradiation caused a tight stacking of the sheets, with a more compact aggregation due to the impacts among the flakes that pushed them together, which ended up to be more packed and bigger because of the more extended number of cross-links on the surface extension, with a less porous structure.In the conventional hydrothermal treatment the convective fluxes were more controlled and regulated thanks to the directionality of the heating, from the whole external wall of the autoclave towards the internal mixture. Thanks to these homogenous heating, the self-assembly was more smooth and delicate, giving birth to a fluffy and spongy aerogel. On the contrary, the uniform heating of the whole mixture induced by the microwave irradiation and the simultaneous rapid and firm cooling from the bottom caused a chaotic and disorder convection inside the reaction medium, that determined a turbulent motion of the GO flakes, resulting in a twisted deformation, a face-to-face contact and a more corrugated and less porous structure, comparable with the more compact but still expanded morphology obtained by chemical reduction with hydrazine (Shi, G. et al., 2011). The MW-assisted hydrothermal process resulted in a more crumpled and wrinkled structrure where the nanosheets were stacked and entangled with each other, instead of been randomly but gently connected. This difference in the arrangement was easily recognizable with high-resolution images (fig. 4.9).

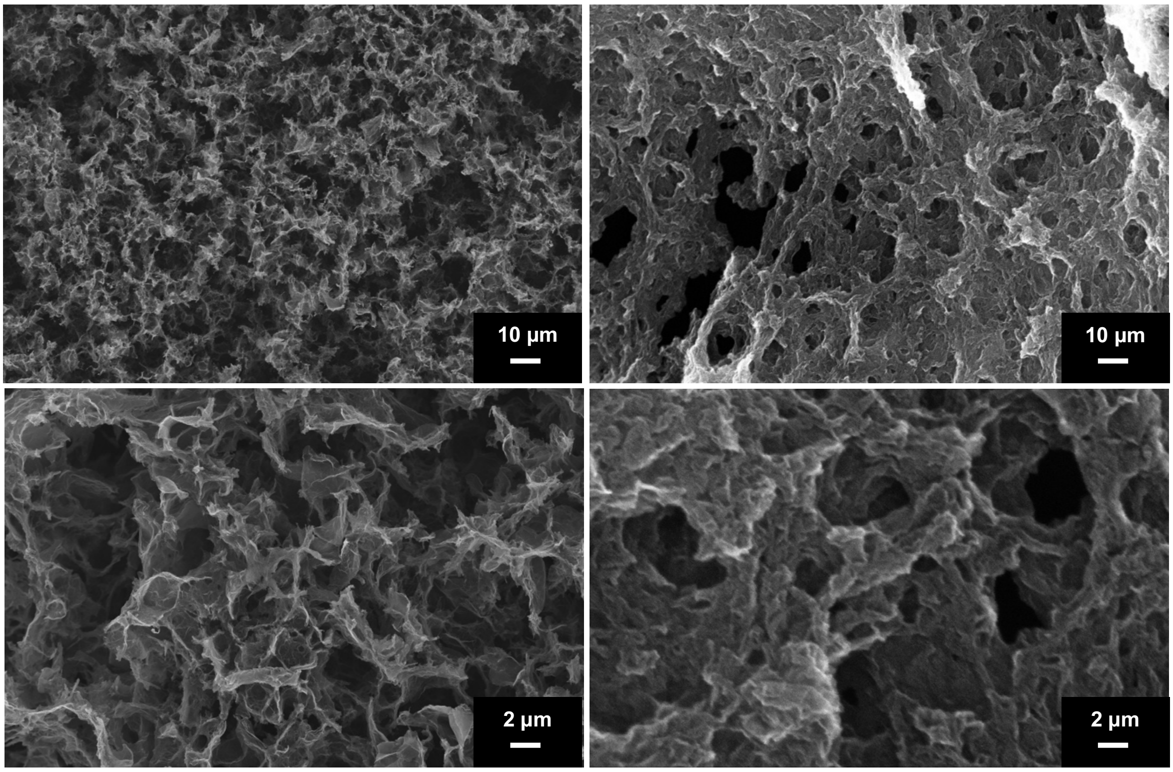

Figure 4.8: Low resolution scanning electron microscope images of HT-RGO (left) and MW-RGO (right)

The pores could be made more fine and ordered increasing the GO concentration in the dispersion or performing a high-temperature annealing (Cheng, Y. et al., 2017). Different drying process would have also had an effect on the aerogel structure, which can be obtained more uniform and ordered with supercritical CO_2 drying, substituting water with acetone or ethanol, instead of a freeze-drying, during which the formation of ice crystals causes a collapse of the finer parts of the network (Zhang X. et al., 2011).

The solid wrinkled pore walls in both sample consist of thin layers of few stacked reduced graphene oxide sheets, which are are almost transparent under the electron irradiation (Zhao, Y. et al., 2012). The restoration of π orbitals developed a reinstatement of the electrical conduction, as can be deduced by the absence of charging during the imaging, contrary to what occurred with non-coated graphene oxide samples (Zhou, Y. et al., 2009).

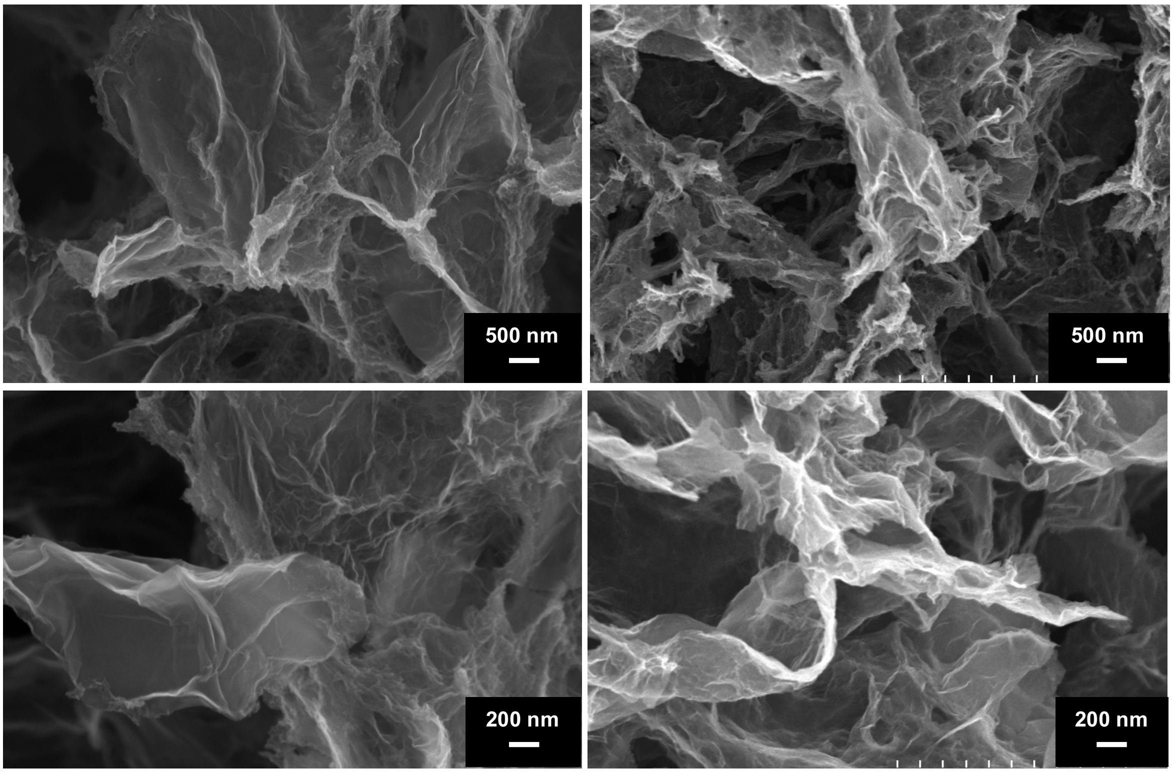

Figure 4.9: High resolution scanning electron microscope images of HT-RGO (left) and MW-RGO (right)

BET Surface Area Analysis

To characterize the exposed surface areas and pores properties and size distribution of the aerogels was used the nitrogen physisorption through N_2 adsorption–desorption experiments carried out at −196 °C (77.3K, temperature of liquid N_2) using a Micromeritics ASAP 2020 gas adsorption and porosimetry system (USA). The samples were degassed, to remove water in the form of moisture or adsorbed species, before adsorption measurements in vacuum at 60°C for 12 hours overnight, at a the pressure less than 5 µmHg. The specific surface area was calculated by the Brunauer-Emmet-Teller (BET) multipoint method using adsorption data from isotherms (fig. 4.10) in the relative pressure (P/P_0) range of 0.05–0.25. Cumulative pore volumes and surface area curves (fig. 4.11) were obtained by applying the Barrett–Joyner–Halenda (BJH) method for N_2 adsorption at –196°C.

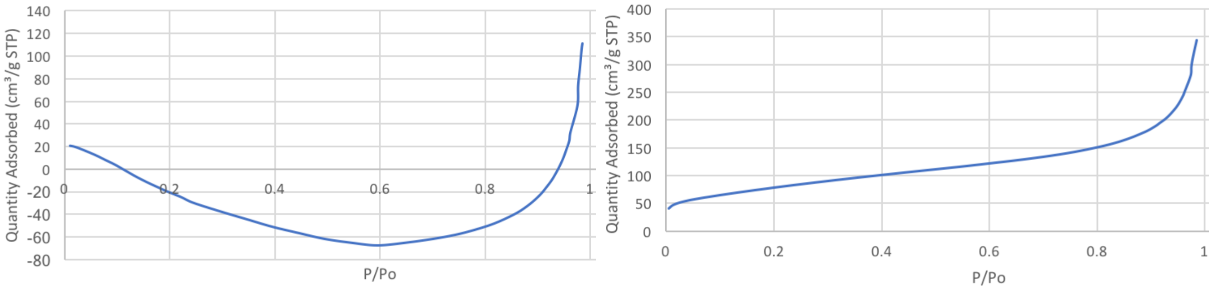

Figure 4.10: Nitrogen adsorption curves for HT-RGO (left) and MW-RGO (right)

The analysis parameters were determined using a predetermined set for porous carbon materials proposed by instrument software. It was probably the wrong setting because it was obtained only the adsorption curve for both sample and, in addition, all the experiments performed on HT-RGO were affected by an unresolved leakage problem, probably due to the volatile nature of the micrometric powder, a not sufficient air tightness of the sealing or a too low temperature during degasing, which made any result collected unusable. The absence of the desorption curve gave no clue on the possible presence of a hysteresis loop, and thus on the shape of the pores. It was supposed to obtain a result like an isotherm tipe IV with an hysteresis loop, characteristic of a mesoporous material with low adsorption energy, obtained with vitamic C reduction (Zhang, X. et al., 2011), or a complex isotherm, composed by a first section, in the low relative pressure region, of isotherm type I, typical of the physisorption on a framework with extremely fine micropores, and a second part at high P/P_0 ratios attributable to a isotherm type II, indicative of the filling of a mesoporous material with high adsorption energy, typical of hydrothermally reduced aerogels (Gigot, A. et al., 2016).

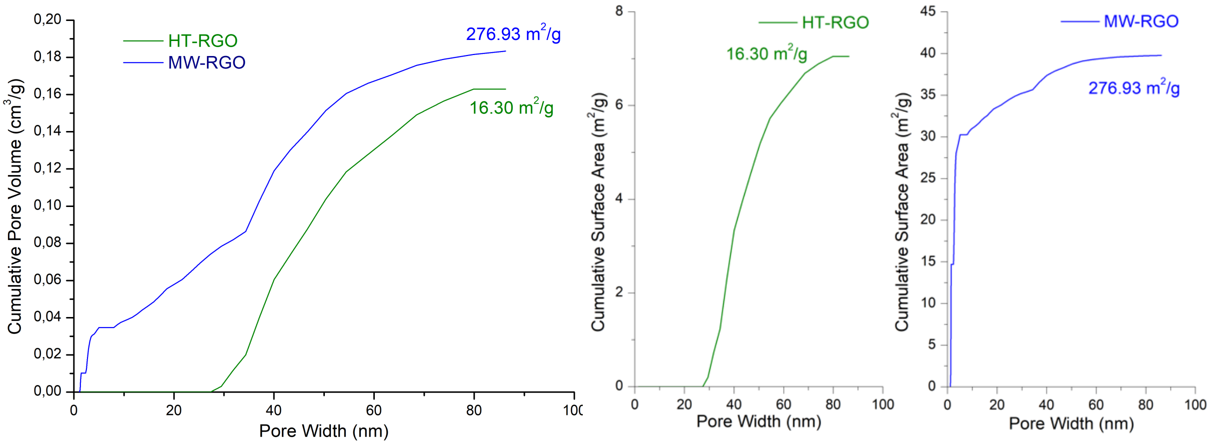

Figure 4.11: Cumulative pore volume (left) and cumulative surface area (right) curves for HT-RGO and MW-RGO obtained with BJH method

The adsorption curve allowed only to determine the SSA of MW-RGO, 276.9 m^2/g, with a good precision, while the result for HT-RGO is not reliable. A N_2 physisorption experiment was previously performed on HT-RGO, produced with different amounts of AA and without it (fig. 4.12), by means of another instrument, Quantachrome Autosorb 1C surface analyzer (USA), and emerged a specific surface area of 510 m^2/g, double of the value obtained for the MW-assisted hydrothermally synthesized aerogel, maybe due to the more violent and drastic reaction, in accordance with the morphology. A double concentration of AA in the mixture, 2mg/mL, would have resulted in a SSA of 335 m^2/g (Gigot, A., 2018). Such extents were extremely lower than defect-free graphene theoretical specific area, 2630 m^2/g, but comparable with fully exfoliated GO, which has a SSA of 278 m^2/g (Kim, H. et al., 2014) which becomes of one order of magnitude lower when aggregated, between 25 and 50 m^2/g (Szabó, T. et al., 2006) or even lower than 10 m^2/g when GO sheets are stacked due vacuum filtration (Lin, D. et al., 2016). While a further reduction has a low positive effect on the SSA, the effect of the introduction of AA in the reacting mixture, as can be seen from fig. 4.13, is strongly dependant on the concentration: 2 mg/mL induce a lower SSA but a more uniform pore structure, while 1mg/mL results in a more extended surface with heterogeneity in the pore sizes. From these results it was derived the amount of ascorbic acid used for MWHS. HT-RGO SSA is lower than hydrothermally reduced RGO with $NaHSO_3$ (603 m^2/g, Cheng, Y. et al., 2017) AA-reduced aerogel at room temperature and dried with supercritical CO_2 (512 m^2/g) while is higher than GO thermally reduced (234.1 m^2/g, Kim, H. et al., 2014), chemically reduced (466 m^2/g, Stankovich, S. et al., 2007) further chemically reduced after hydrothermal treatment (215 m^2/g, Shi, G. et al., 2011), hydrothermally reduced GO with the addition of glucose in the mixture (365 m^2/g), pyrrole (280 m^2/g, Zhao Y. et al., 2012) or boric acid (218 m^2/g Zhou, G. et al., 2016), CNT/RGO hybrid aerogel (435 m^2/g, Sui, Z. et al., 2012), spark-expanded RGO (394 m^2/g, Lin, D. et al., 2016).

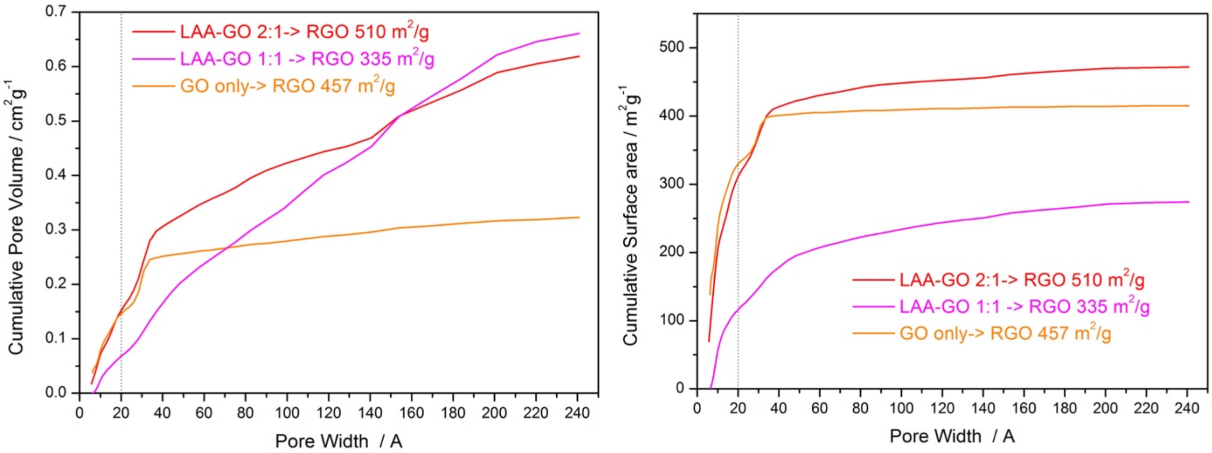

Figure 4.12: Cumulative pore volume (left) and cumulative surface area (right) curves for HT-RGO synthesized with different amounts of ascorbic acid (1:1=1mg/mL; 2:1=2mg/mL), obtained with DFT method

The collection of only the adsorption curve of the isotherm posed a limit on the maximum diameter analyzed, because the BJH method estimated the pores size distribution especially via the desorption data, which were not gathered, but was still possible draw some conclusions coherent with previous results. From the cumulative pore volume curves it was possible deduce that the pore size distribution is hierarchical not bimodal, as confirmed by the evident differences in terms of matrix morphology and porous texture between HT-RGO and MW-RGO aerogels in SEM images. Furthermore, in RGO aerogels obtained only with supercritical water the main contribution to the pore volume was given by pores with a width inferior to 40Å, with around half of the contribution related to micropores (<20Å), while introducing a reducing agent allows to broaden the size distribution (Gigot, A., 2018). In HT-RGO, pores under 40Å are also the main contribution to most of the surface area, while in MW-RGO their share was significantly lower. Pores formation in HT-RGO was induced either by self-assembly and bubbles trapped in the framework, deriving from the liberation of CO_2, main fraction of the reduction products, which could act as templating agent for the connection of the sheets, and their presence determined a higher specific surface area and the buoyancy of the obtained hydrogel on the water's surface. In MW-RGO, the high heating rate induced a drastic reaction which did not consent the entrapment of the bubbles, resulting in a porosity in which the contribution of micropores is almost completely missing. Even if it is not possible make any certain assumption on the distribution of the pores in MW-RGO above 80 nm, the average pore diameter is around 8 nm, which is consistent with the results obtained from other RGO aerogels obtained via microwaves irradiation, even if has half of the SSA obtained with a power four time higher (415m^2/g, Hu, H. et al., 2012).

There is also a strong effect due to the drying mechanism: the freeze-drying induced a shrinkage probably caused by a collapse and breakdown of fine pore walls due to ice crystals growth, which with its volume expansion forced smaller pores to coalesce together, leaving in the structure mainly unordered interconnected meso and larger pores that laid beyond the range accessible to nitrogen adsorption analysis, while a samples dried by supercritical drying would have hypotetically shown a different pore size distribution, because bypasses the destructive differential capillary stresses of sublimation drying replacing the solvent into its supercritical state, suppressing thr surface tension at liquid-solid interface, resulting in a higher efficiency (Zhang, X. et al., 2011; Cheng, Y. et al., 2017).

X-ray Diffraction Spectroscopy

The structural characteristics of the materials under study were assesed through a X-ray powder diffraction analysis performed with a Bruker D8 Discover diffractometer, Germany. The diffraction patterns (fig. 4.13) were collected with monochromatic coppert target with Kα1 wavelength λ=1.54Å, over the angular range between 5° and 75° at a scan rate of 0.01°/s, a step length of 2θ=0.02° and an accelerating voltage of 40 kV and an applied current of 40 mA. The relevant data obtained from the spectra are available in Table 4.1.

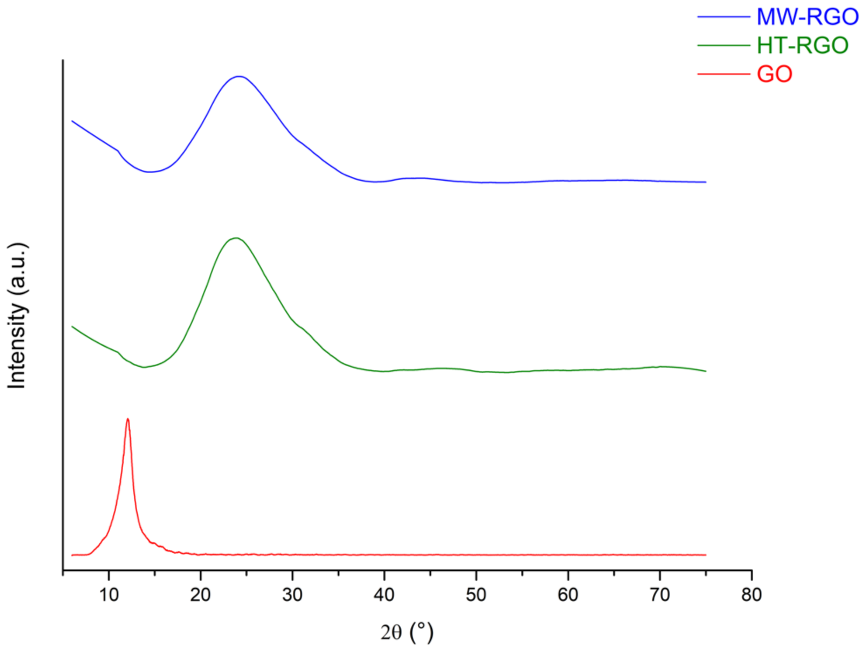

Figure 4.13: X-ray diffraction powder spectra of the samples

GO spectrum showed its characteristic sharp peak at 12.06°, correlated to reflection on (001) graphitic plane of stacked sheets (Jeong, H.K. et al., 2008), without showing any further peak around 26.5°, position of the typical strong peak of graphite, which shifts towards smaller angles with the increase of the oxidation time and/or degree, which means an expansion of the interlayer distance (Jeong, H.K. et al., 2008), indicating that no residual traces of starting material were present in the powder, which is completely oxidized (Marcano, D. et al., 2010). The position of the dominant peak of GO corresponded to an average interlayer *d-spacing* of 7.33Å, calculated with Bragg's diffraction law:

$$d = \frac{n\lambda}{2sin\theta}$$

where the positive integer *n* was assumed equal to 1 and λ was the wavelength of the incident wave. This interlayer distance could be either attributed to a one water molecule-thick layer that presumably formed hydrogen bondings between adjacent sheets (Liu, F. et al., 2012) and to the steric effect of oxygen-containing functional groups (Fu, C. et al., 2013). GO interlayer spacing is proportional to the degree of oxidation (Marcano, D. et al., 2010). The reduced graphene oxide samples, HT-RGO and MW-RGO, showed a pronounced peak centered at

23.85° and 24.18° respectively, due to the reflection on the (002) plane, symptomatic of the restoration of the graphitic structure, which thus confirm that both partial reduction properly occurred, with the formation of RGO (Gigot, A. et al., 2016). The hydrothermal treatments did not remove all the oxygen functionalities on both sides of the plane, which resulted in a lower interaction between the sheets if compared with pristine graphite and in a random interspace (Liu, F. et al., 2012). The average *d-spacing* was 3.73Å for HT-RGO and 3.68Å for MW-RGO: both value were lower than the interlayer distance in the precursor and in samples obtained with not-chemically assisted hydrothermal reaction (3.87Å, Murugan, A. et al., 2010) and slightly larger than the spacing in well-ordered graphite, around 3.36Å (Ganguly, A. et al., 2011), due to the presence of a small amount of oxygen-containing functional groups and other lattice defects (Gao, W. et al., 2009). It is possible restore a highly ordered crystalline structure performing an annealing at very high temperature under slightly reducing atmosphere, which induces a strong deoxygenation, depicted by a shift of the RGO peak back to the position of the peak related to properly arranged graphite (Cheng, Y. et al., 2017). These interlayer spacing were comparable with those resulting from further chemical reduction of the aerogel with hydrazine (Shi, G. et al., 2011) but also with vitamin C (Zhang, X. et al., 2011) which meant that the presence of AA in the mixture avoided the need of an additional treatment. The persistence of these irregularities resulted, besides the predominant peak, in a small peak at 2θ ≈ 11°, characteristic of (001) graphene oxide, and another around ~ 43°, typical of the (101) plane and characteristic of the turbostratic band of disordered stacking in carbon materials (Chang, B. et al., 2012). Both peaks were very weak, could be confused with the backgrond and appeared in both spectra.

Table 4.1: Data from diffraction spectra

Sample	2θ peak position, °	FWHM, °	Interlayer spacing, Å
GO	12.06	2.15	7.33
HT-RGO	23.85	9.10	3.73
MW-RGO	24.18	9.74	3.68
Graphite (ref.)	26.5		3.36

The large FWHM implicated the presence of strains and defects in the framework, with MW-RGO a little narrower and then slightly more graphitic and piled, due to the π-π stacking caused by the face-to-face contact between the nanoleaflets (Zhao Y. et al., 2012). The broadening and shift of the characteristic diffraction peak was due to the poor ordering along the stacking direction, with the sheets stacked only with a short-range order, which implies that the aerogel frameworks were composed mainly from single or only a few piled up layers of RGO. (Muragan, A. et al., 2010)

It was possible calculate the average number of RGO layers in the pore walls by analyzing these peaks through the Lorentzian fitting and Scherrer equation

$$n_L = \frac{\beta\lambda}{FWHMcos\theta}$$

where the parameters ß was assumed equal to 0.91, λ was the wavelength of the incident wave and the Full Width at Half Maximum is expressed in radians. It resulted a number of stacked layers between 2 and 3, which is smaller than the number of stacked sheets deriving from further chemical (4-6 per pore wall) or thermal reduction (1-4 per pore wall), with the lower stacking due to the less drastic reaction (Yang, S., 2011; Shi, G. et al., 2011; Zhao Y. et al., 2012).

4.3.2. Chemical characterization

Thermogravimetric Analysis

Thermogravimetrical analysis was aimed to study the thermal stability and the behaviour of the RGO when heated in an inert environment, to simulate a rapid heating performed in the glovebox. The investigation was performed on a TA TGA Q500 (USA), with the samples contained in Pt crucibles subjected to a heating ramp of 10°C/min between room temperature and 600°C under nitrogen flow of 100 mL/min. The relevant data obtained from the analysis are available in Table 4.2.

Table 4.2: Residual mass percentages at different temperatures

Sample	100 °C	200 °C	250 °C	300 °C	400°C	500 °C	600°C
GO	91.2%	82.3%	56.0%	53.2%	50.1%	46.9%	42.7%
HT-RGO	99.0%	95.9%	93.5%	90.9%	86.7%	80.5%	75.2%
MW-RGO	98.9%	92.9%	90.2%	87.4%	83.1%	79.7%	76.9%

The analysis was carried out at a higher rate than the usual heating ramp used to determine the thermal stability of the material (5°C/min) due to the necessity to reproduced the thermal shock that the material would suffer when put in contact with molten lithium. The high speed heating has an important effect on the stability, because same samples heated at a lower rate showed a higher stability. A more rapid heating regime induces a vigorous release of gas products, resulting in a rapid and large volume expansion and a larger mass loss (Stankovich, S. et al., 2007), especially of GO, whose thermal stability decreases with the increase of the oxidation degree which weakens the Van der Waals interactions between the sheets, distrupting the stacking and promoting the process of weight lossing (Shen, J. et al., 2009).

The reduction to graphene aerogels introduced a higher thermal stability, as can be seen from the thermal gravimetical curves (fig. 4.14), due to the deoxygenation of the material. The rapid weight loss occurred in the initial region below below 100°C is related to drying or desorption of loosely bound physisorbed water, which is around 9% of the mass of GO, while only 1% of the mass of both reduced materials, but also to the direct decarboxylation of edges, which occured at temperatures as low as 70 °C (Hu, K. et al., 2013). A drastic mass loss in the GO took place between 150°C–300°C (~35%) and was associated to the decomposition of thermally labile oxygen groups, such as epoxy, lactone, carboxyl and hydroxyl groups, while in the next part the loss is ascribe to the decomposition of more stable oxygen-containing functionalities present in the lattice, such as phenol, carbonyl and quinone (Chang, B. et al., 2012).

The abrupt mass drop around 200 °C, characteristic of unreduced graphene oxide, disappeared after reduction,with both samples that showed a slow and steady mass decrease over the whole temperature range, indicative of the removal of the most of the oxygen moieties during hydrothermal treatments, but not the most stable. The tolerance to higher temperatures is introduced not only in inert environment, but also to oxidation in air (Cheng, Y. et al., 2017). The aerogels are thermally stable up to 200°C with less than 8% wt of loss, and at 250°C, temperature of interest, the weight loss is less than 10%, with the conventional HS that produced a sligtly more stable framework than MAHS up to 535°C. After 500°C, the uniform weight loss in all samples could be ascribed to high temperature pyrolysis of the carbon skeleton, similar to the linear dependence without any step of graphite (Shen, J. et al., 2011). Chemical reduction showed a higher thermal stability (Fernandez-Merino, M.J. et al., 2010), due to the more energetic deoxygenation, with less than 5% of loss at 200°C (Zhu, C. et al., 2010). The minor stability is due to the low concentration of reducing agent in the mixture, whose mechanism is predominant on the hydrothermal reduction, giving results comparable with a reduction carried out under alkaline conditions (Fan, X. et al., 2008) even with the addition of a reducing agent (Shen, J. et al., 2011). The predominance of the mechanism is also shown by the derivative curve of the TGA plots related to the RGO aerogels, whose showed the same matching peaks as the DTG obtained by the thermogravimetrical analysis of graphene oxide reduced by means of ascorbic acid at 95°C, which is almost as efficient as hydrazine to remove the labile oxygen moieties, but not sufficient to remove the most stable (Fernández-Merino, M.J. et al., 2010). The drying mechanism had also an important role to determine the stability, because it was demonstrated that freeze-dried aerogels have a higher thermal stability than those where the water was remove with supercritical drying (Zhang, X. et al., 2011).

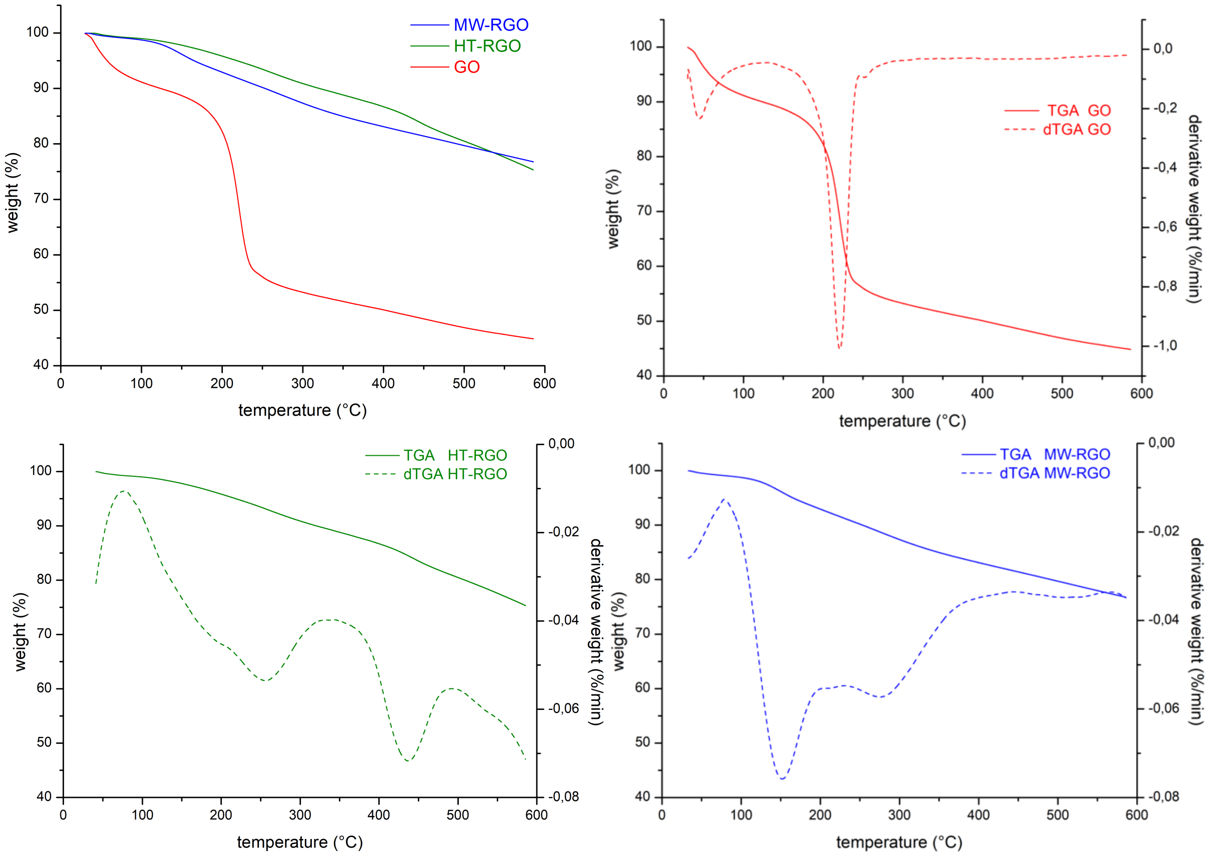

Figure 4.14: Comparison among the different materials thermal gravimetric curves and between integral and differential curves of each sample

It is possible restore a highly ordered crystalline structure performing an annealing at very high temperature under slightly reducing atomsphere, which induces a strong deoxygenation, which would result in an almost unchanged TGA plot, characterized by a negligible or even no loss during heating in inert environment, like pristine graphite (Gao, W. et al., 2009).

Raman Spectroscopy

Raman spectroscopy is the main characterization technique for graphene-like materials, because the phonons scattering, sensitive to changes in the electronic structure, it is able to provide information on crystalline size, number of stacked layers, network disorder and evolution in the density and type of structural defectivness of the lattice, degree of hybridization and the extent of chemical modification (Ganguly, A. et al., 2011). The spectra (fig. 4.15) were collected at room temperature in a range of Raman shifts between 1000 and 4000 cm^{-1} with a resolution of 1 cm^{-1}, using a Thermo-Fisher DXR Micro-Raman Microscope (USA) with a diode laser source λ=532nm (2.33 eV), with low laser power to avoid laser-induced local heating. The spot of the laser, 500nm, was localized on the sample by means of a microscope in backscattering light collection Baseline due to photoluminesce automatically subtracted by the system software after a background acquisition. The relevant data obtained from the spectra are available in Table 4.3.

Table 4.3: Data from Raman spectra

Sample	D peak, cm^{-1}	G peak, cm^{-1}	D/G intensity ratio
GO	1353	1594	0.77
HT-RGO	1351	1591	1.02
MW-RGO	1352	1593	0.92

Defect-free graphene, mechanically exfoliated from highly oriente graphite, shows only the G band in its Raman spectrum, while there is no presence of D peak in defect-free graphene because it is indicative of disorder, distorsions and defects in the lattice (Casiraghi, C., 2011), while rises and become more prominent in functionalized graphitic materials like graphene oxide, whose sheets are characterized by a surface delimitated by edges, the main defective area (Kanyoor, A. et al., 2012). In GO the defects are not proper lattice irregularities, bu the electronic structure is modified by the presence of edges and heteroatom moieties connected to a mostly hexagonal structure of the plane. The relative ratio between the intensity if D peak and G peak (I_D/I_G or D/G ratio) is an indication of the level defectiveness of the framework, and graphite usually has a ratio lower than 0.2 (Gao, W. et al., 2009). The increase in the ratio from GO to RGO and RGO was indicative of the reduction and was due to significant structural changes induced by HP-HT harsh conditions during the hydrothermal process. MW-RGO had a lower ratio than HT-RGO, and this meant an inferior introduction of irregularities in the lattice, because of the more rapid dehydration and cahotic motion, with probable less reactions among the functional groups. A ratio D/G~1 is typical of graphene synthetized by thermal or hydrothermal reduction, but is also lower of the ratio obtained if the reduction is performed by means of a chemical reducing agent like hydrazine, Id/Ig=1.44, so the hydrothermal route was more effective than chemical way to repair the sp^2 network. The treatment removed the oxygen-containing functional group but introduced imperfections like vacancies and sp^3-hybridated carbon atoms. The D/G ratio increases with the increase of reaction time (Sheng, K. et al., 2011) and decreases with the rise of the hydrothermal treatment temperature to control the extent of conversion, suggesting a higher ability to recover aromatic structures by repairing defects (Zhou, Y. et al., 2009; Mungse, H. et al., 2014).

The D band derived from double resonant breathing mode of κ-point scattered phonons of the A_{1g} mode due to the disappearance of transational simmetry caused by the presence of defects in the lattice and edges made of carbon atoms with dangling bonds where the band is particularly Raman-active. G peak arised from the first-order inelastic scattering involving the double degenerated LO and iTO phonon mode due to the E_{2g} symmetry at the Brillouin zone center, corresponding to the in-plane vibration of sp^2-bonded carbon atoms (Pimenta, M. et al., 2007; Gigot, A. et al., 2016). The presence of the G band in the spectra is and indication of the predominance of sp^2 carbons in the network, while sp^3 and sp hybridation would show their characteristic peaks at 1333 cm^{-1} and in the range 1850–2100 cm^{-1}, respectively (Pimenta, M. et al., 2007). The Raman shift of the G band in GO, broadened and blue-shifted to higher wavenumbers due to the presence of isolated double bonds with higher resonance frequencies than graphite G peak (1577 cm^{-1}) (Zhu, C. et al., 2010), changes as function of the oxidation degree, because its position increases with a decreasing number of stacked layers (Shen, J. et al., 2009). The reduction induced a decrease in average size of the in plane-sp^2 domains and a more disordered structure, increasing the number of edge defect atoms with a sp^3 hybridation (Stankovich, S. et al., 2007).

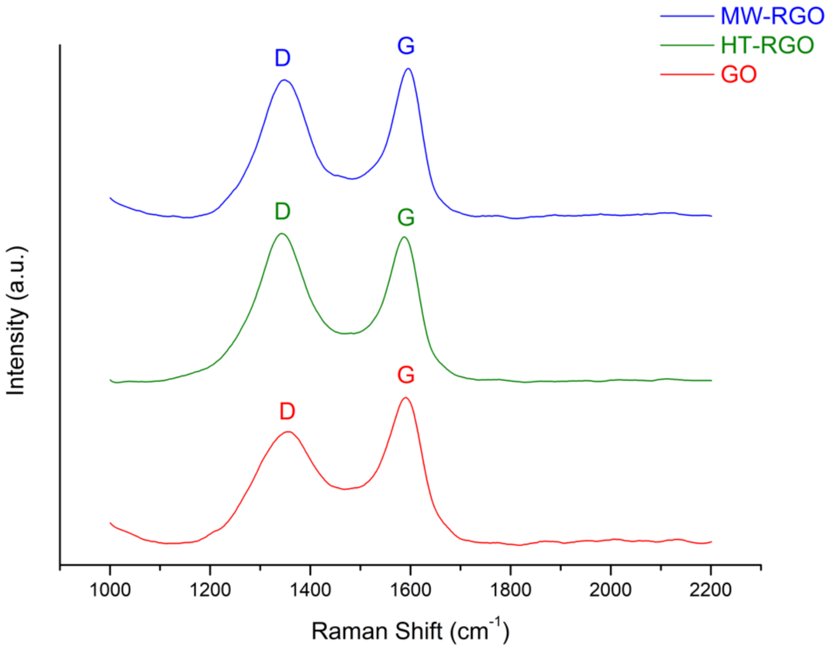

Figure 4.15: Raman scattering spectroscopy spectra of the samples

There was a neglible change in the full width at half maximum of the G band, and the unbroadened peak meant that the D peak was generated from edges rather than structural defects (Shen, J. et al., 2011). Furthermore, the D band for the aerogel obtained with the microwave assisted method was slightly wider that the hydrothermally-obtained material, which meant that the violent heating caused a fragmentation along the reactive sites and yields new graphitic domains, which led to a higher number but smaller in size connected sheets compared to GO before reduction, constituting a more discontinuous structure with stacking faults which exposed less external edges if compared to HS aerogel, as demonstrated by the weaker D peak intensity (Shen J. et al., 2009; 2011).

In the spectra there was no evidence of the D' peak at around 1620 cm^{-1}, due to phonons scattering caused by defects confinement (Ganguly, A. et al., 2011), which should form a shoulder overlapped on the side of G peak, so it can be considered negligible if compared with D band. The value Id/Ig~1 is also typical of the low density defect regime, due to the partial oxidation and defined by a ratio $I_D/I_{D'}>7$, which is characterized mainly by sp^3-carbon type defect regime, consisting in oxygen atoms bonded to the surface or carbon atoms with a different hybridization, while D/D'<7 is indicative of a relatively high state of defectiveness in graphene, predominantly composed by vacancy type defects which have a strong effect in scattering phenomena (Zandiatashbar, A. et al., 2014).

Moreover, the two-dimensional (2D, also called G') peak (~2750 cm^{-1}), usually form a broad band with the D + G combination mode (~2950 cm^{-1}), but was weakened and broadened due to increasing disorder and amorphization caused by the oxidation and reduction processes experienced by the materials (Sui, Z. et al., 2012, Zandiatashbar, A. et al., 2014). This peak was insignificant and indistinct from the background, for this reason their region is not displayed. The G' band is the second-order overtone of the D band which originates from a double resonance Raman scattering process involving two iTO phonons at the κ-point, and is usually visible in highly ordered graphene and crystalline graphite (Kudin, K. et al., 2007; Casiraghi C., 2011). 2D peak position, shape and wideness is highly sensitive to the numbers of stacked sheets, so it is used to discriminate between few-layer and monolayer graphene (Pimenta, M.A. et al., 2007).

The absence of the characteristic peaks can be attributed to the excitation laser energy value, because position and intensity of the bands related to the defects are strongly dependant on the laser source wavelength (Pimenta, M. et al., 2007, Zhan, D. et al., 2011).

In the low defect density regime is possible calculate an average distance between sp defects L_d through the formula, derived with a same wavelength laser (Zandiatashbar, A. et al., 2014):

$$\mathrm{L}_d = \sqrt{\frac{C}{\mathrm{I}_D/\mathrm{I}_G}}$$

where the parameter C is assumed equal to 102 nm^2. It resuled an average distance around 11.5 for GO, 10 nm for HT-RGO and 10.5 nm for MW-RGO.

It can be also calculated the average crystallite size L_a in the materials, which also has a strong effect on the intensity of the peaks D and D' (Pimenta, M. et al., 2007):

$$\mathrm{L}_a = 2.4\mathrm{x}10^{-10}\lambda^4\frac{\mathrm{I}_G}{\mathrm{I}_D}$$

where λ is the laser source wavelength, and resulted a size of 25 nm for GO, 21 nm for MW-RGO and 19 nm for HT-RGO.

It is possible restore a highly ordered crystalline structure performing an annealing at very high temperature under vacuum or slightly reducing atomsphere, or else a microwave irradiation under inert atmosphere, which induces a strong deoxygenation, which would result in a slightly reduced D/G ratio and a back-shifted G peak closer to graphte peak than GO, indicating a partial recovery of the irregularites in the lattice after the further elimination of oxygen moieties, obtaining a less defective hexagonal network like unoxidized pristine graphite, but with residual strains due to the forced removal of oxygen from the surface (Ganguly, A. et al., 2011; Hu, H. et al., 2013).

Fourier Transform Infrared Spectroscopy

The infrared spectroscopy is a chemical structure characterization technique to study the functional groups evolution after reaction through their bonding vibration triggered by a specific IR frequency absorption. FTIR spectra (fig. 4.16), represented in transmission, were recorded on a Thermo-Nicolet Nexus 670 (USA).

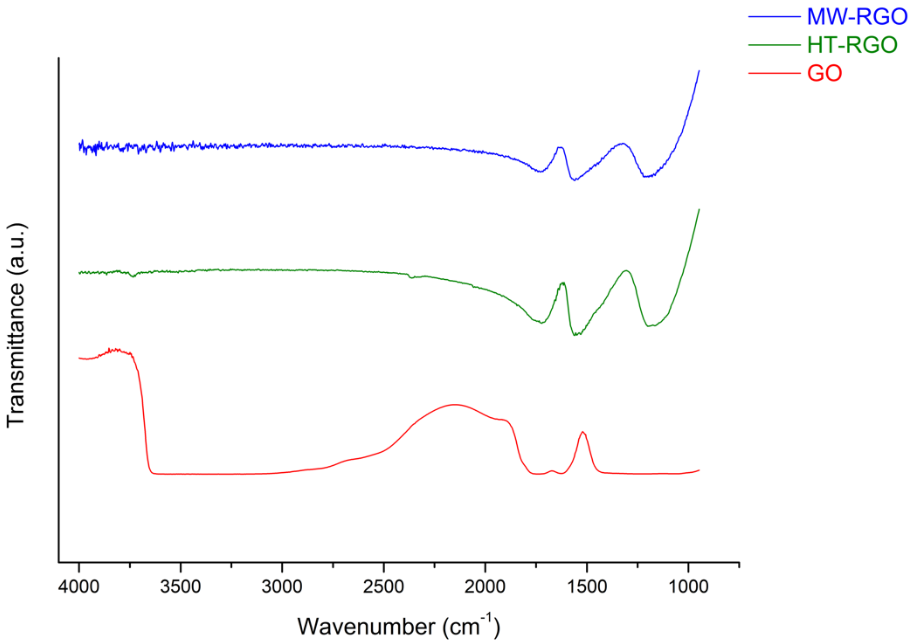

Figure 4.16: FT-IR absorption spectroscopy spectra of the samples

Infrared spectrum of defect-free graphene and dry non-exfoliated graphite show no relevant peaks, indication of the absence of any heteroatom in the lattice or functional group bounded to the surface. The oxidation and resultant exfoliation is a chemical functionalization that introduces IR-active species in the sp^2-hybridized structure, like carbonyls and carboxyls arranged on the basal plane and on the edges edges, which can also change the hybrization of the bonded carbon atom to sp^3, such as hydroxyls and epoxies located on the top and bottom of the surfaces (Tucureanu, V. et al., 2016).

Before reduction, graphene oxide showed a broad band from 3650 to 2350 cm^{-1}, corresponding to an overlapping of the stretching mode of hydroxyl and phenolic groups and to the hydrogen bonds formed between them and between the layers (3600 cm^{-1}), a band centered at 3450 cm^{-1} due to physisorbed water, in accordance to TGA results, a wide band related to the O–H in carboxyls and including dangling CH_3 or CH_2 groups; a peak at 1740 cm^{-1}, ascribable to C=O stretching in carbonyl and carboxyl groups, another peak, at 1620 cm^{-1}, corresponding to O–H bending in hydroxyls and adsorbed water, is partially superimposed on the previous one and overlapped with the band originating from in-plane vibrations of the unoxidized sp^2-hybridized skeletal C=C aromatic ring in the network. The wide band in the fingerprint region from 1500 to 900 cm^{-1} was due to the overlapping of C=C stretching vibration at 1450 cm^{-1} with several peaks attributable to different oxygen-containing functional groups, like bending mode of O–H (1410 cm^{-1}) and characteristic peaks of C–O bond at 1350 cm^{-1} and 1230 cm^{-1}, C–O from epoxies (1150 cm^{-1}), carbonyls (1080 cm^{-1}) and carboxyls (1030 cm^{-1}). The GO structural complexity do not allow to evaluate any peak below 900 cm^{-1}, not displayed in the spectrum (Marcano, D. et al., 2007; Tucureanu, V. et al., 2016).

Upon reduction, only three features remained in the spectrum of both HT-RGO and MW-RGO: an asymmetrical peak at 1740 cm^{-1}, deriving from C=O in carbonyls and esthers groups embedded in the network surface, another asymmetrical band at 1560 cm^{-1}, related to restored carbon double bonds constituting the aromatic ring, which is shifted shift towards lower wavenumbers from the position in GO spectrum due to the removal of oxygen moieties from the framework, because the vibration frequencies depend on bond strength with neighboring atoms (Lin, D. et al., 2016), and a symmetrical band centered at 1160 cm^{-1} due to C–O–C bond in ehters groups (Hu, K. et al., 2016) (epoxy are thermally unstable). The characteristic absorption bands of oxidized groups decreased dramatically, indication of a deep deoxygenation, with a main removal of functional groups located at the edges, and the restoration of conjugated π-orbitals. The reduction is denoted especially by the disappearance of the broad band between 2500 cm^{-1} and 3600 cm^{-1} is related to the removal of the very labile hydroxyl groups, while the peaks of the other more thermally and chemically stable oxygen-containing surface functional groups were retained, indication of a non complete reduction process. The absence of peaks at 2950 cm^{-1} and 2850 cm^{-1}, related to methyl and methylene groups respectively, it is a symptom of their absence in the structure due to the intra-sheet condensation of dangling functional groups on the surface, or an inter-sheet reaction with a subsequent cross-link with the elimination of a small molecule (Bagri, A. et al., 2010).

The results are consistent, as well with lithium-sparked RGO (Lin, D. et al., 2016), with spectra collected from GO hydrothermally reduced with superheated water at 200°C for 12 hours (Mungse, H. et al., 2014) and chemically reduced with ascorbic acid in heated medium (Fernández-Merino, M.J. et al., 2010). It should be noted that a not sufficient reaction time would have left residual peaks related to oxidized species (Mungse, H. et al., 2014), just like a reduction with vitamin C at room temperature (Zhang, J. et al., 2011). This means that the oxygen moieties removal mechanism was the same in both treatments, and is a combination between the effect introduced by the addition of vitamin C in the mixture, which can be supposed to be predominant in accordance with previous results, but is enhanched by the superheating of the water, which also cooperates in the reduction, as can be deduced by the absence of a peak centered at ~2800 cm^{-1}, related to a C-H bonds stretching vibration, typical of low temperature chemical reductions (Tucureanu, V. et al., 2016).

X-ray Photoelectron Spectroscopy

The X-ray photoelectron emission spectroscopy is the most reliable to prove the succesful deoxygenation of the GO sheets and determine analytically the reduction degree. The analysis was carried out at room temperature under UHV conditions by means of a PHI Quantera II (USA), equipped with monochromatic Al Kα (1486.6 eV) X-ray source with a 200 μm beam size, set at 49 W and a pass energy of 187.95 eV with a 1.6 eV/step for survey scan and 29.35 eV with a 0.25 eV/step for the high-resolution scan. Were collected data from three different point on each sample in case of compositional inhomogeneities.The relevant data obtained from the survey spectra (fig. 4.17) are available in Table 4.4.

The average C/O ratio obtained for the starting material, 1.9, is lower than the usual ratio obtained preparing the GO for itself, around 2.5 (Xu, Y. et al., 2010), which means that the commercial GO powder is more oxidized. From technical datasheet, the C/O ratio, probably measured right after production, should be around ~1, this means that the employed powder was slightly reduced, presumably by humidity during storage period. The results from the spectra showed that the oxygen-containing functional groups groups were partly removed:

HT-RGO had an average reduction degree of 5.9, more than three times larger than the starting material, and a little higher than MW-RGO, 5.3, Without the assistance of any reducing agent, using only superheated water, the C/O with same starting material would have been 4.38 (Gigot, A. et al., 2016). If the starting material was less oxidized (C/O=2.7), the obtained reduction degree would have been comparable (C/O=5.3; Xu, Y. et al., 2010). In conventional hydrothermal treatment, C/O ratio increases with increasing reaction time (Xu, Y. et al., 2010) and rising temperature (Mungse, H. et al., 2014), but, from the results we can deduce that we could reach a similar reduction degree obtained with a 12 hours reaction reducing the time to one hour by introducing microwave-induced heating, with the same amount of reducing agent in the mixture.

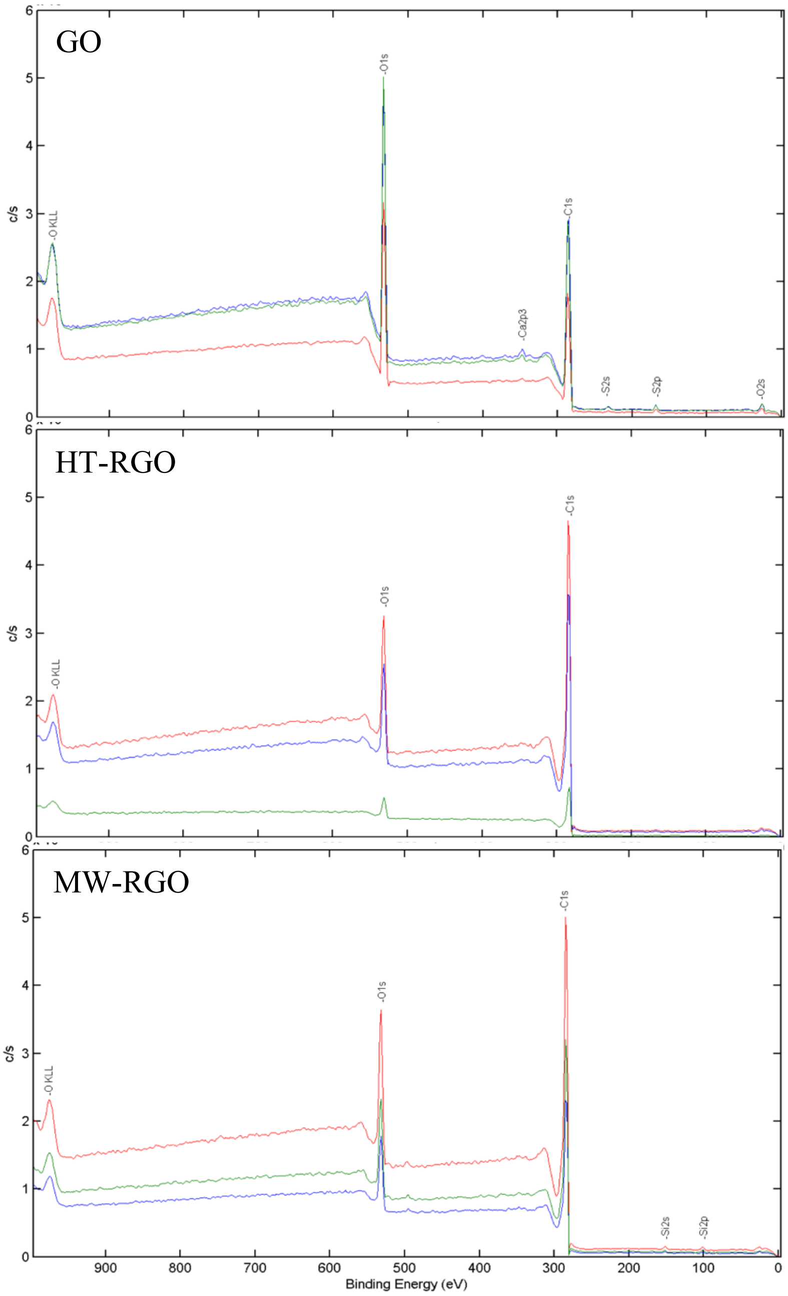

Figure 4.17: X-ray photoemission spectroscopy survey spectra of the samples

Wide scan showed S and Si contamination due to the presence of those chemicals on the workbench during preparation of the samples for the analysis. A double concentration of vitamin C in the solution treated with conventional hydrothermal treatment would have given a higher C/O ratio, 7.5 (Gigot, A., 2018).The resulting reduction degrees are both very lower than graphite ratio, around 13 (Gao, W. et al., 2009), but comparable with GO reduced with ascorbic acid at room temperature and freeze-dried (C/O=5.79), but lower if dried with supercritical method (C/O=6.41, Zhang, X. et al., 2011), higher than chemical reductions with EDA (C/O= 2.3; Hu H. et al., 2013), pyrogallol, ammonia and sodium borohydride (C/O= 5.56, 5, 3.33 respectively, Fernández-Merino, M.J. et al., 2010) and thermal reduction at low temperature (C/O=3.14; Jeong, H. et al., 2008) but lower than reductions performed with hydrazine, C/O 6.0 but with the presence of a high concentration of nitrogen in the framework, which influences the ratio, or hydroiodic acid, C/O=6.7 (Shen, J. et al., 2011), and thermal reduction at high temperature in slightly reducing environment (C/O>10 at 600°C, Ha, S. et al., 2013) or further thermal annealing (C/O>20, Cheng, Y. et al., 2017) or MW-assisted annealing (C/O=23; Hu H. et al., 2013). Furthermore, the obtained C/O ratio is close to that obtained with lithium sparked RGO (C/O=6.64, Lin, D. et al., 2016).

Table 4.4: Relative atomic concentration from XPS survey

Sample	C1s	O1s	C/O	Sample	C1s	O1s	C/O	Sample	C1s	O1s	C/O
GO	64.7	35.3	1.83	HT-RGO	85.4	14.6	5.85	MW-RGO	84.5	15.5	5.45
	66.0	34.0	1.94		85.8	14.2	6.04		84.2	15.8	5.33
	64.4	35.6	1.81		85.5	14.5	5.90		84.1	15.9	5.29

The high-resolution spectra (fig. 4.18) could have been deconvoluted in overlapped gaussian components to calculate the changes in the relative percentage of functional groups in the RGO, dividing the area under the curve related to the respective characteristic bond by the whole spectrum area. The deconvolution of C1s spectra would have composed of several curves: one at 284.8 eV, attributed to sp^2-hybridized double bonded carbons (C=C) in non-oxygenated aromatic ring, while the others are related to sp^3-hybridized carbon atoms: 285.5 eV corresponding to hydroxyl and phenolic (C–OH) groups and also possibly to C-C bonds in defected structures, another at 286.3 eV, related to C–O–C bonds, typical of epoxies, esthers and alkoxies, a third one associated to carbonyl and quinone (C=O) groups at 288.0 eV and a last one at 289.2 eV, relative to carboxyls (O=C–OH) groups (Ganguly, A. et al., 2011, Fernández-Merino, M.J. et al., 2010).

The spectrum of the hydrothermally treated aerogels exhibits deconvoluted peaks associated to the same functionalities as the starting GO, but the intensities of the signals related to oxygen moieties are much weaker but retained, reflecting an effective but insuffficent reduction to RGO. The decrease in intensity mainly involved peaks related to thermally labile functional groups, like carboxyl, hydroxyl and epoxy, in accordance with the mechanism proposed in literature (Hu, K. et al., 2016), with the retainment of the aromatic ring signal, due to the deoxygenation that induces regeneration of the conjugated bonds, and residual peaks related to more stable functionalities during hydrothermal treatment, like esthers an carbonyls, resulting in a higher thermal stability, confirmed by previous thermal analysis.

Reduced graphene oxide spectra also showed a broadened tail associated to the remarkable $\pi \rightarrow \pi^*$ shake-up satellite peak at around 291 eV, typical of aromatic systems like graphitic materials, characterized by delocalization of electrons in π orbitals.This feature, typical of few-layer graphite materials, is caused by electronic interband transition stimulated by the

C1s electron photoemitted due to X-ray irradiation from the core. The presence of this signal means a few layers stacking order in both materials, as confirmed by XRD results, even if characterized by a high defect density in the honeycomb lattice (Gigot, A. et al., 2016; Mungse, H. et al., 2014).

From O1s high-resolution spectrum could be possible a deconvolution in three peaks, one at 531.1 eV, relative to C=O bond, another one attribute to C–OH at 532.0 eV and a last one at 533.4 eV, ascribable to C–O–C bond (Ganguly, A. et al., 2010). The peak of the hydroxyls is predominant in GO but after reduction is decreased, confirming the selective removal of C–OH groups, while the peak related to the characteristic bond of esthers, deriving from the dehydration of hydroxyls groups, slightly prevails on the C=O signal, bond of ketons deriving from condensation of carboxyl groups. This result is due to an interlayer cross-linking between GO flakes during assembly and an intrasheet binding subsequent to bending of the flexible building blocks during deoxygenation.

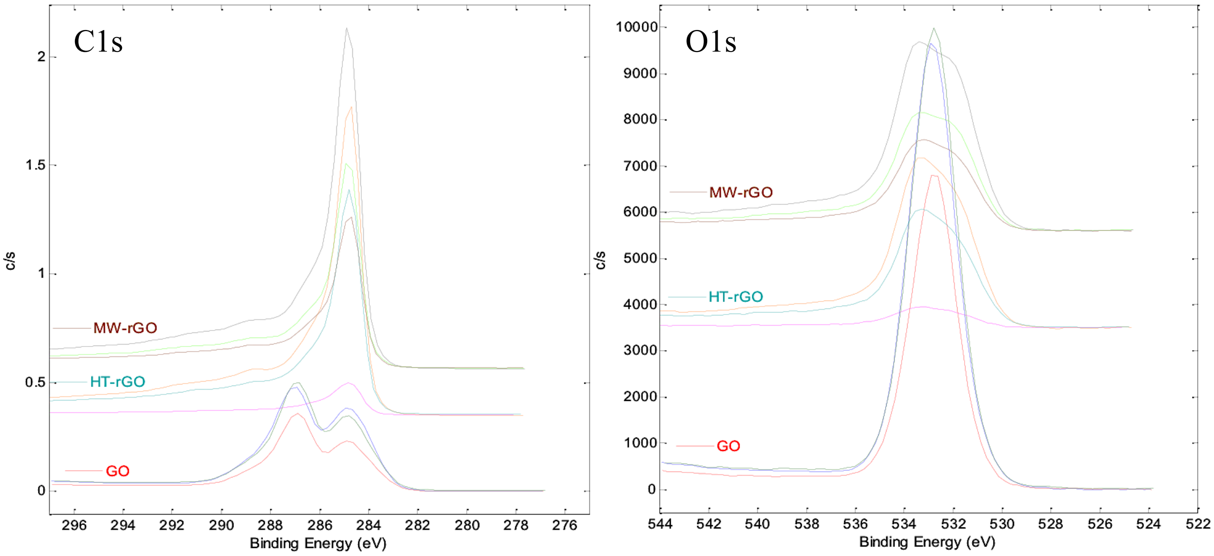

Figure 4.18: High-resolution X-ray photoemission spectra of C1s and O1s

5. Batteries assembly and characterization

5.1. *Protective layer fabrication and device assembly*

The main goal was to introduce inside the cell a free-standing protective layer produced in a fast and easy method to place on the metallic lithium surface, without the need of dispersing the material in NMP with additives and then coat a current collector (Cheng, X. et al., 2015). Free-standing anodes were obtained by vacuum filtration of water dispersed-GO by using a Whatman aluminum oxide membrane as filter (diameter of ~47 mm and pore size of ~0.2 μm) to get a packed layer that could be peeled off and dried. The further reduction to RGO was performed with a thermal heating at high temperature in inert environment (Mukherjee, R. et al., 2014) or with a spark reaction induced by contact with molten lithium (Lin, D. et al., 2016). Both the resulting membranes show expanded GO flakes achieved by the rapid gas formation, although they involve tools and methods hardly scalable for large productions. Liu and colleagues proposed to thermally treat in air an aerogel of unreduced graphene oxide after the freeze-dried procedure and then press it to obtain a paper-like membrane. The lithiation of the electrode was performed by electrodeposition of lithium inside the anode, requiring a sacrificial cell containing a lithium metal counter electrode (Liu, F. et al., 2012). We tried to prepare a self-standing anode starting from hydrothermally reduced graphene oxide to reduce the number of steps required to the whole process. First of all, we tried to prepare a binder-free membrane to fully and effectively exploit the inner porosity of the material: the RGO was dispersed in isopropanol (IPA) and then the mixture was sonicated for 1 minute. The dispersion was then settle down on a flat surface substrate, to promote the precipitation. The excess of solvent was removed and the residual was let to evaporate at room temperature overnight. The obtained mossy material was slightly pressed covering a glass slide with a detaching layer made of polyethylene. Several different substrates, such as glass, stainless steel and aluminum foil were used as flat substrates, but it was very difficult to peel off of the material as one free-standing sheet because it was too fragile for its lack the lack of binding force between the flakes.

The free-standing membrane was then fabricated with a dry method typical of Li-ion batteries (Claus D., 2011): the powder was mechanically crushed in a mortar with a pester and adding a 5% wt of PTFE powder as binder. The mixture was ground until all the binder could not be seen. Usually, when performed with graphite powder, the mixture form a uniform and flexible layer with a shiny surface, but RGO does not have a strong affinity with ultra-hydrophobic PTFE as graphite, so the grinding produced a coarsely aggregated powder. The powder was poured in a modular die, useful to take it out without any risk of chipping or damaging it. The die was composed of a bottom flat surface, a top layer with a 12 mm diameter circular hole and a punch with the same diameter of the hole (fig. 5.1a). The die was then pressed with a compression machine applying a constant pressure of 5 tons for 30 second. This pressure was the lowest useful to induce a good compactness of the membrane, while lower pressure resulted in a poorly aggregated mixture. The powder without the addition of the small amount of binder did not result in continuous film after pressing. To facilitate the removal of the assembled membrane, the die was disassembled and a piece of Celgard® was placed on the surface of the punch as detaching layer, from where the membrane can be easily peeled-off with tweezers after lifting one side from the Celgard®. After the layer was detached, the surface of the sample showed an irregular and coarse surface (fig. 5.1b), resulting from the aggregation of the powders, easily recognizable after pressing, while the opposite face, pressed onto the steel bottom of the die, resulted flat and shiny. The membranes, with a diameter of 12 mm and a mass of 12±1 mg including the binder, were dried in vacuum at 70 °C for 24 h to remove any residual moisture of volatile contaminant (i.e. IPA) and any undesired side-reactions during assembly of the cells.

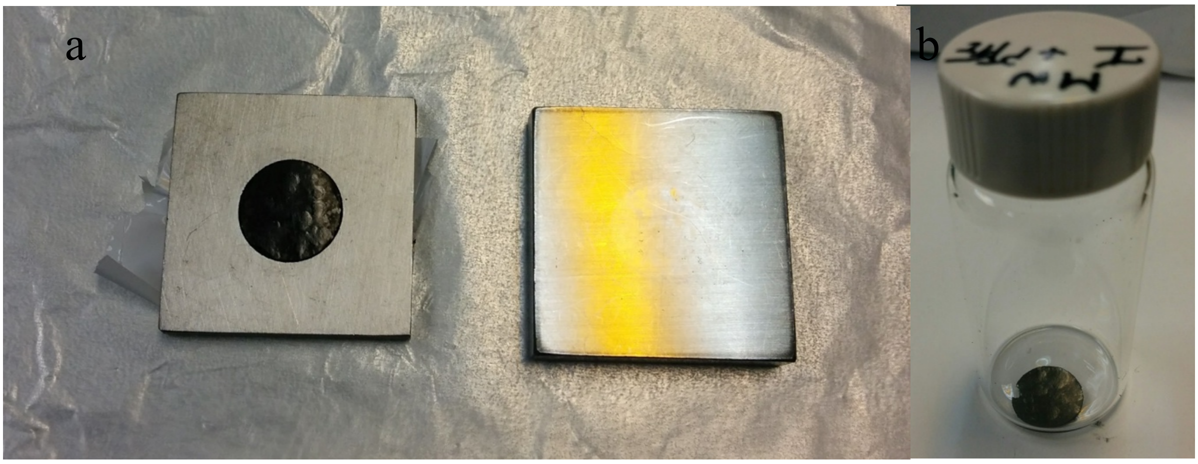

Figure 5.1: Free-standing RGO membrane a) still inside the die and b) inside a 20 mL vial after vacuum drying

One side of the membranes was cut, mounted on a 10° inclined sample holder and coated with platinum for SEM imaging to study the obtained morphology and measure the thickness (fig 5.2). The differences in the morphology due to the different production method disappeared, because the mechanical grinding and then pressing crushed the fine structures, leaving a micrometric coarse morphology with a slightly uneven surface. From the cross section images it could be seen the stacking of the powder grains due to the pressure. The average thickness, mesured on different regions of the samples, were between 60 and 70 μm for HT-RGO samples and between 80 and 90 μm for MW-RGO. This difference was due to the intrinsic difficulty to weight the same amount of material for every layer, due to the volatility and the not high accuracy of the measure.

To study the effective lithium dendrite suppression in lithium metal anode and the subsequent lifespan improvement during, Li stripping/plating processes, the membrane were introduced into CR-2032 type coin cell in a symmetric cell configuration (fig. 5.3) inside an argon-filled glove-box (MBraun MB220B modular) with both oxygen and water content less than 1 p.p.m. Two 7 mm discs obtained from fresh lithium foil were placed inside the positive cap and on a stainless-steel spacer, respectively, and heated for 1 minute at 250°C. After, the membrane was placed on molten lithium for 5 minutes, to let the lithium enter inside the structure and ensure a good adherence between the two layer. During contact it could be seen a deformation in the center of the membrane, forming a depression in correspondence of the lithium diameter, indication of an interaction between RGO, PTFE and lithium. It wasn't introduced a second spacer due to problems during the closing of the cell, because of the membranes thickness. The electrodes were then cooled down and assembled, using a 19 mm disc obtained from a Toray film as separator and 100μL of electrolyte, which contained 1M lithium hexafluorophosphate ($LiPF_6$) in a mixture of ethylene carbonate (EC) and dimethyl carbonate (DMC) 1:1 in volume ratio. The reference lithium symmetric cell was prepared in the same way and with the same electrolyte but without the inserted membranes. The electrolyte and lithium metal foil were purchased from Sigma Aldrich, the separator from Toray.

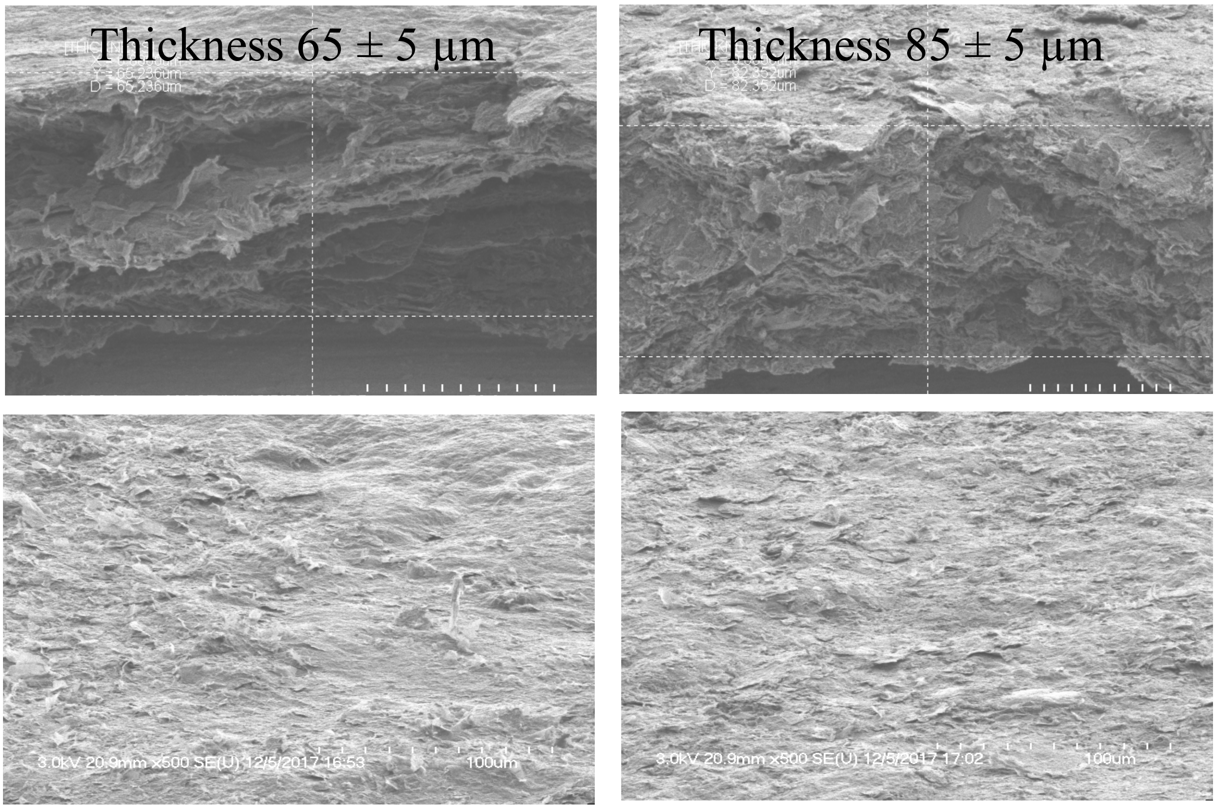

Figure 5.2: SEM images in cross section (top) and planar (bottom) view of membranes made with HT-RGO (left) and MW-RGO (right)

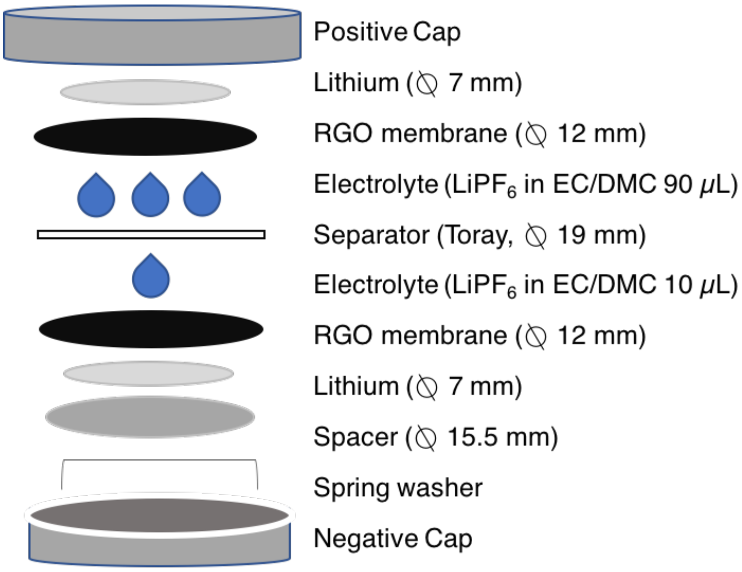

Figure 5.3: Schematic in exploded view scheme of the assembled CR2032 coin cells

5.2. *Electrochemical characterization*

The different reduction degree in the materials deriving from the different synthesis technique could result in a hypothetical difference in conductivity in the aerogels. The conductivity was tested instead directly on the membrane via two-probe method between two copper foils and connected to a multimeter, using Ohm's second law:

$$\sigma = \frac{1}{R}\frac{L}{S}$$

Resulted for HT-RGO an average conductivity of 0.042 ± 0.005 S/m and for MW-RGO an average conductivity of 0.022 S/m ± 0.005 S/m, which means that the introduction of PTFE makes the conductivity fall of 4 orders of magnitude from the supposed as prepared aerogels conductivity (Xu, Y. et al., 2010).

5.2.1. Cyclic Chronopotentiometry

Galvanostatic cycling with potential limitation was used to evaluate the electrochemical stability window of the materials imposing a constant current upon the cell and studying the variations in the voltage, which indicates the changes in electrode processes occurring at its interface. The analysis was performed with a MACCOR Series 4000 Multifunction battery test system (USA) at 1mA/cm^2 for 700 cycles, with a half cycle time of 1 hour, delivering a capacity of 1mAh/cm^2, in a potential cut off window of ± 1V.

From the cycling profile (fig 5.4) it can be seen that the reference cell with bare lithium went through a surface modification at each cycle with variable impedance until a voltage drop due to SEI formation and an increase in the current density induced by dendrites and active surface extension decrease, outlined by an abrupt drop at ~190 hours after a gradual increase in the potential gap. Between 70 and 120 hours the showed an irregularly fluctuating voltage profile (fig. 5.5) fading from a peaking behavior, related to a transition in the kinetic at the solid-electrolyte interphase during stripping and plating due to the formation of dendrites nuclei on the surface, to an arcing profile reaching a plateau at the end of the half cycle, characteristic of a mass transport effect due to the tortuous diffusion pathway in the amassed dead lithium layer to deposit on the active surface. The increase in the overpotential is due to electrolyte degradation and depletion that leads to SEI formation and thickening, with subsequent dead lithium build-up and continuous accumulation after the detaching of dendrites from the surface (Chen, K.-H. et al., 2017). The cells containing the RGO membrane did not show any evidence of dendrite-induced failure for long-term cycling, because maintained the stability of the electrodes acting as additional interface between Li metal and electrolyte without completely hindering the ionic conduction, mechanically inhibiting dendrite growth not being able to be pierced by them, but their potential gap was higher than the initial overpotential in symmetric Li/Li and increased over time. It is possible, due to conductivity and affinity of the layer to the lithium, that the metallic nucleation takes place on the surface of the RGO, but this hypothesis cannot be backed with SEM images because the layer broke down once opened the cells after cycling. The voltage gaps are excessive if compared to other solution, which narrowed the overvoltage to ±0.2 V with low hysteresis (Liang, Z. et al., 2016; Lin, D. et al., 2016; Liu, Y. et al., 2016). The high overpotential is due to kinetic hindrances in the system, like ion transport in the electrolyte and charge transfer resistance at the electrode/electrolyte interphase (Bieker, G. et al., 2015), but especially to the tortuous lithium ions diffusion pathway induced by the presence of the membranes and their thicknesses, which is around three order of magnitude higher than native SEI thickness, that affects concentration gradients, resulting in a lower effective diffusion depth (Chen, K.-H. et al., 2017). After an initial instability, until 20th cycle, due to the accommodation of the lithium surface under the membrane, both samples had a much more stable cycling, and then stable plating and stripping process (Wang, B. & Guo, Y., 2010), when the reference cell started to show cycle irregularities. The voltage profile showed immediately the arcing, another symptom of the tortuous diffusion, which, during the half cycle, was characterized by an uncomplete plateau formation, indication of an insufficient either time either rate that would provide a greater concentration gradients of Li ions, and this was reflected in a more pronounced arc every cycle and a slow increasing overpotential, almost 100% after 250 cycles, due to the limited diffusion in the protective layer. The difference between the electrodes might be due to a slightly different thickness and material mass loading in the electrodes, because for a thin electrode, kinetic resistance dominates the internal resistance, and the evolution of the overpotential is expected to be different for thicker electrodes, with a higher tortuosity (Mistry, A., et al., 2017). The large and irregular overpotentials are also mainly due to the fast, continuous and irregular growth of SEI on the surface of the membranes over time, with a different rate on each electrode, due to their intrinsic difference (Xu, K., 2014).

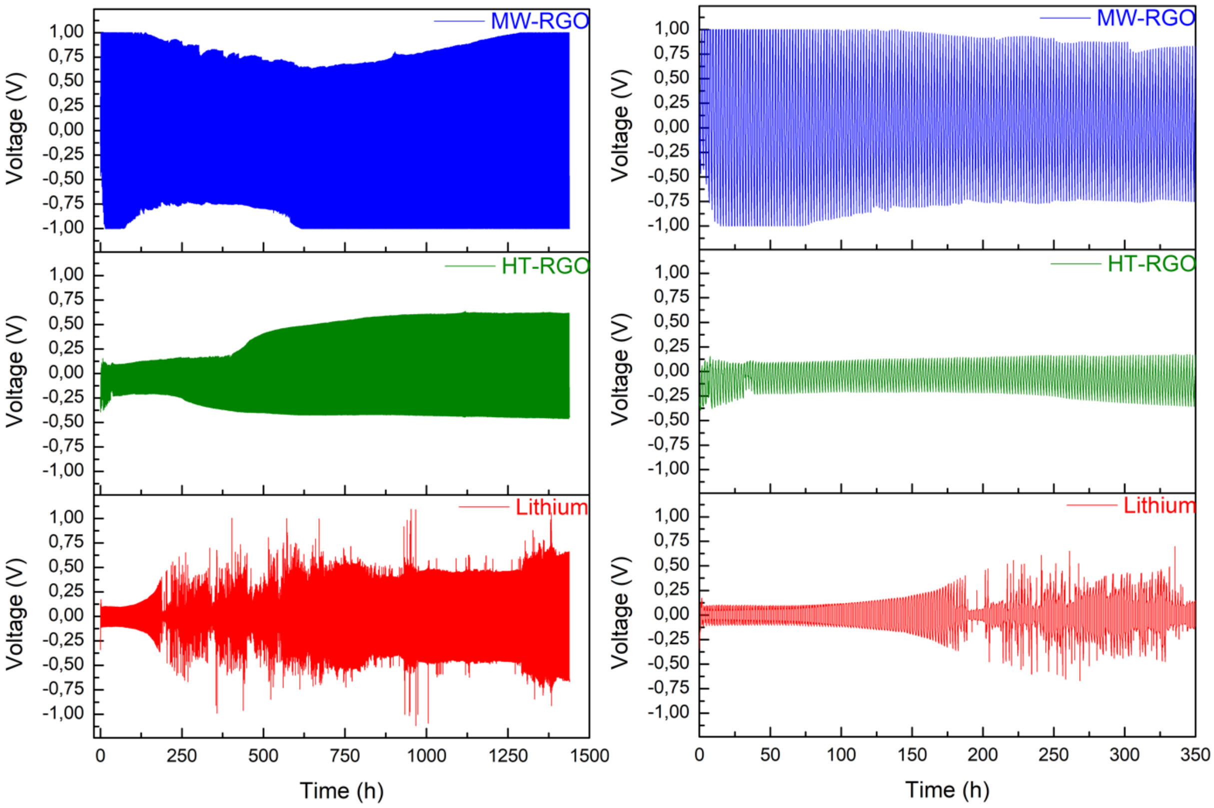

Figure 5.4: Galvanostatic long-term cycling voltage profiles of symmetric bare Li/Li and Li-RGO/RGO-Li cells until end of test (a) and until 350 hours (b)

MW-RGO showed a peculiarity in addition to the extremely high voltage gap, presumably due to the higher thickness of the membrane, around 85µm, with a difference of around 10µm with HT-RGO, which is comparable with the electrode thickness proposed in other works (Liu F. et al., 2012), which means that both membranes had an excessive thickness, but over 80 µm it is disruptive The voltage profile showed a necking, with a first decrease followed by an increase, which is a characteristic sign for dendrite formation and growth during cycling under the membrane in early stage and SEI breaking, formation and accumulation later, making the surface rougher and leading to a reduced effective current density (Liu, Y. et al., 2016). The reduction in the overpotential is also due to the lithium ion easier crossing of the membrane after accommodation of the surface under it, while the further increase is due to the thickening of the SEI probably on the top layer of the RGO.

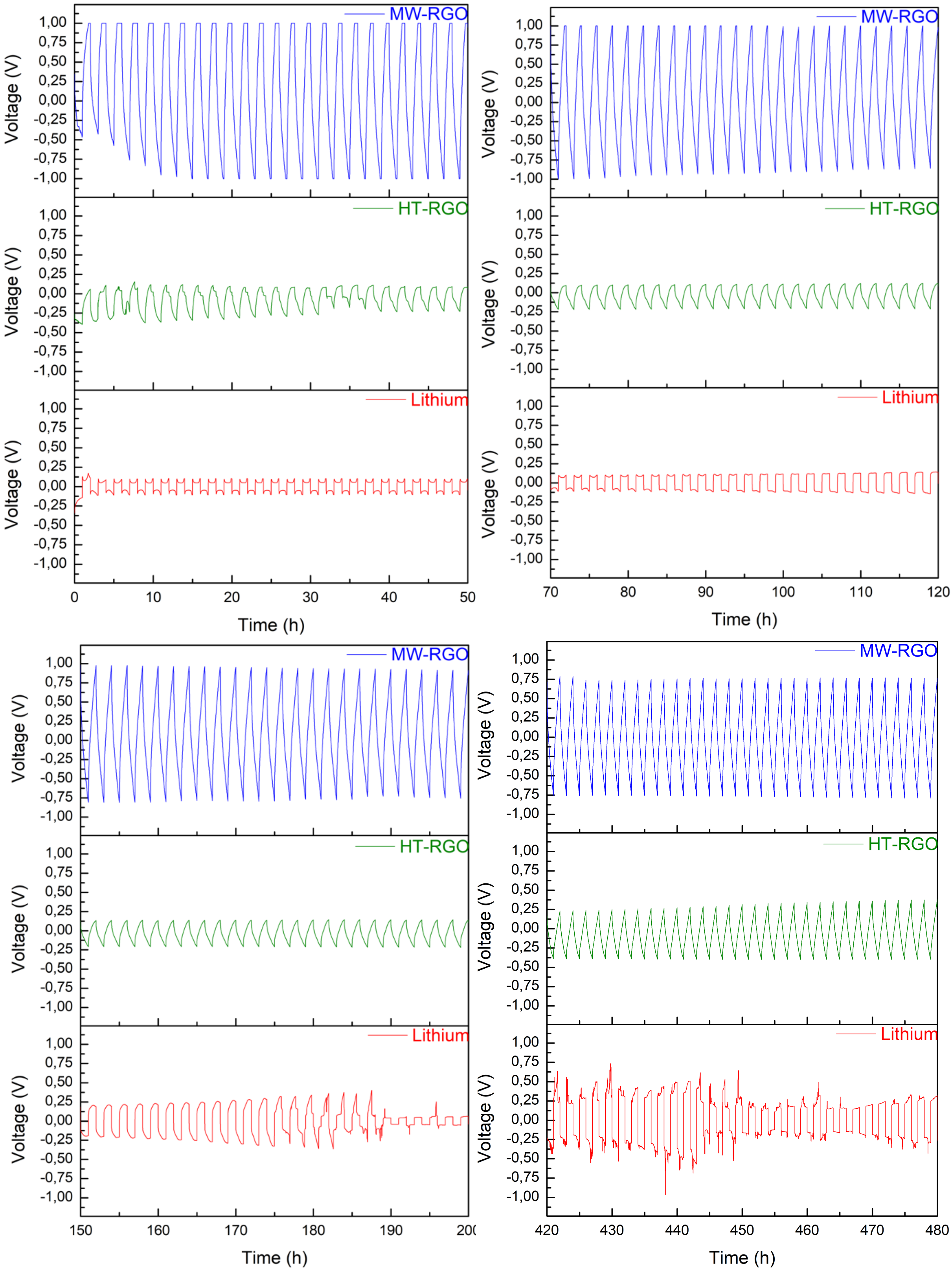

Figure 5.5: Detailed galvanostatic cycling voltage profiles between different cycles

5.2.2. Electrochemical impedance spectroscopy

Electrochemical impedance spectroscopy (EIS) further explains the growth of SEI during the galvanostatic cycling by virtue of the measurements of the changes in the electrical impedance of the symmetric cells during a frequency swipe. The EIS was performed in the galvanostatic mode (GEIS), with a small alternate current signal superimposed to a direct current i_{DC}=0mA, that defines an open circuit voltage (OCV) measure with a BioLogic multi-potentiostats/galvanostats/EIS VPS-300 (USA) over a wide range of frequency, from 0.1 Hz to 1 MHz. The EIS was used to get informations about the irregular and fast growth of SEI and to support the interpretation of the overpotentials by measuring the development of the electrode surface resistance during lithium stripping/plating processes.

The complex impedance can be simplified to get a physical interpretation representing cell with a model equivalent circuit consisting of impedance elements in series (fig. 5.6), composed by elements related to different aspect of the electrode/electrolyte interface.

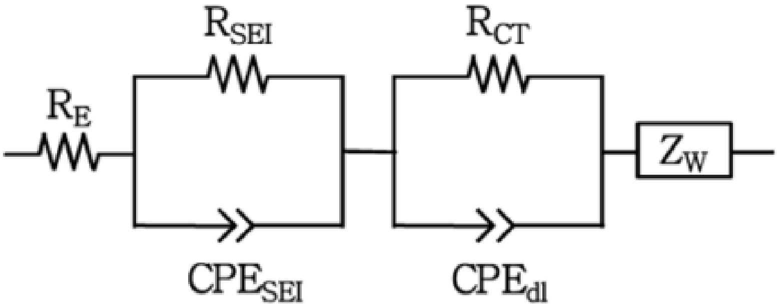

Figure 5.6: Equivalent circuit of the electrode surface in the symmetric cells (*from Shin, W. et al., 2015*)

R_E is the internal resistance of the electrolyte solution and separator, R_{SEI} and CPE_{SEI} are resistance and capacitance related to the migration of Li^+ ions through SEI surface film layer, C_{dl} is the double layer capacitance between electrolyte and electrode, which accounts for inhomogeneity, roughness and porosity of the electrode surface, R_{CT} is the resistance related to the charge transfer between electrolyte and electrode through the membrane, CPE_{dl} is the capacitance of the electric double layer and Z_W is the Warburg impedance, determined by the finite diffusion layer thickness of lithium between active material and electrolyte (De Vries, H. al., 2015).

The obtained Nyquist plots (fig. 5.7) have the typical shape of those obtained by the spectroscopy of batteries containing a carbon intercalated electrode (Xu, K., 2014) could be divided in three domains: a low frequencies region, related to a bulk solid-state diffusion in the membrane, and expressed by the Warburg impedance, a mid-range frequencies zone, ascribable to the surface resistances, like charge-transfer on the membrane, and then the ionic migration in the electrolyte at high frequencies (Bieker, G. et al., 2015). At higher frequencies than the charge transfer can be sometimes identified another region related to the presence of an insulating layer, the SEI, whose grain boundaries induce resistive and capacitive properties, which together the RGO membrane contribution, originates the semi-circles denoted by the presence of the capacitance in the equivalent circuit. (Barai, A. et al., 2015). The most relevant data resulting from the fitting of the obtained Nyquist plots are available in table 5.1.

Reference Li symmetric cell showed an extremely large interfacial resistance before cycling, which originates from the native oxide on the foil (Lin, D. et al., 2016). The increase in the series resistance due to the electrolyte depletion and exhaustion caused by reactions with metallic lithium and subsequent dead lithium accumulation during cycling. The charge transfer and SEI resistance decreased because of the formation of dendrites, onto which the lithium deposition is promoted, their detachment from the surface and the cracking of the forming SEI caused by electrode volume and surface continuous variation (Chen, K. et al., 2017). At the same time, during cycling there is a reduction in the resistances determined by surface phenomena (R_{SEI} and R_{CT}), explained by a large increase in the surface area of the lithium anode caused by not flat lithium morphology and dendrites growth after continuous deposition (nonuniform lithium ions stripping/plating experienced by hostless metallic anode) resulting in a poor Li ion transport (Bieker, G. et al., 2015; Liang, Z. et al., 2016).

Table 5.1: Resistances of the equivalent circuits

	Reference Li			**HT-RGO**			**MW-RGO**		
	R_E (Ω)	**R_{CT} (Ω)**	**R_{SEI} (Ω)**	**R_E (Ω)**	**R_{CT} (Ω)**	**R_{SEI} (Ω)**	**R_E (Ω)**	**R_{CT} (Ω)**	**R_{SEI} (Ω)**
Cycle 0	1	291	360	27	61	0	6	210	0
Cycle 1	2	61	112	25	75	0	6	195	0
Cycle 10	2	28	58	24	53	0	5	164	0
Cycle 50	5	22	37	23	104	0	3	68	41
Cycle 100	10	15	25	22	129	0	3	117	57
Cycle 200	16	4	7	21	217	292	3	423	808

RGO containing cells showed a decrease in the electrolyte resistance and SEI resistance due to the infiltration of the electrolyte inside the bulk of the membranes, but had a considerably larger charge transfer resistance compared to the bare Li counterpart. Both RGO samples showed pronounced Warburg diffusion contributions in the low frequencies. An increase in interfacial resistances (R_{SEI} and R_{ct}) is related to both growth of the resistive surface layer on the electrodes and deterioration of the interfacial contacts (Shin, W. et al., 2015). The plots for MW-RGO, after 50 cycles, and HT-RGO, after 200 cycles, can be deconvoluted in two overlapped symmetric semicircles, indication of the rapid growth of a SEI layer, which was not present initially. This result is related to the membranes thicknesses, and means that before short circuit of the reference cell, the cell with thinner layer did not show any relevant SEI formation, while the thicker membrane experienced a faster and early growth of the insulating layer, in accordance with the galvanostatic cycling results. The retarded SEI growth it is an indication of the prevention of dangerous dendrite growth for longer time than the Li foil used as bare metal anode.

The internal resistance of the cells is mainly determined by surface phenomena induced resistances, which are higher than electrolyte intrinsic resistance, independently by the presence of the membranes in the systems. Thus, it can be assumed that the increasing overpotential of lithium deposition and dissolution processes is determined by the nature and the thickening of the SEI and the processes at the lithium/electrolyte interface for bare lithium and lithium/membrane and membrane electrolyte interfaces for protected cells (Bieker, G. et al., 2015).

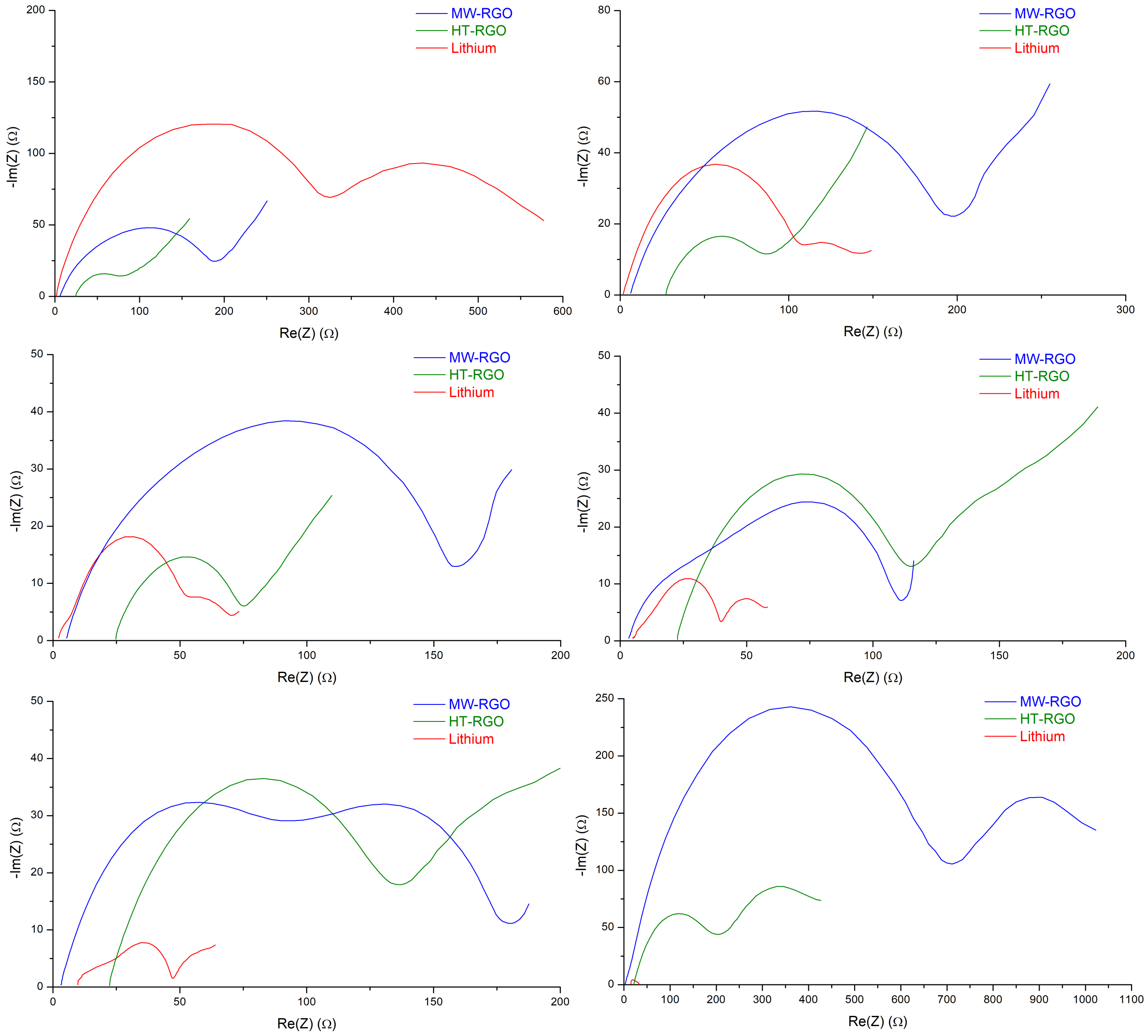

Figure 5.7: Nyquist plots of the symmetric cells (a) before galvanostatic cycling (b) after 1 cycle (c) after 10 cycles (d) after 50 cycles (e) after 100 cycles (f) after 200 cycles

6. Conclusion and future works

Due to its unique properties, reduced graphene oxide is the most suited and promising material to provide an effective improvement in lithium metal anodes safety and reliability, and more in general to high power density energy systems, in order to greatly increase their performances for a future widespread use, especially in the transportation field.

The introduction of ascorbic acid in the reacting mixture allow to control an easy and environmental-friendly synthesis with a green reducing agent introduced in a harmless solvent such as de-ionized water. Without addition, the control of the reaction is less fine because it is made by means of temperature and time variations, which are stochastic and not easily reproducible, while the addition of vitamin C in known concentrations allow to tune with high precision the morphology and the reduction degree. Furthermore, the presence of vitamin C in the system ensures the success of the reduction reaction and self-assembly of the hydrogel without introducing any heteroatom in the framework, except carbon, oxygen and hydrogen, suppressing all the random fluctuations that can affect the achievement of the near-critical state of water, such as an excessive residual amount of dissolved salts in the deionized water. When the reductions were performed with both treatments using only superheated water, most of the time the process failed, resulting in an unsuccessful assembly of the hydrogel, producing only a dispersion of RGO in water. The addition of ascorbic acid always resulted in a well-assembled hydrogel, first indication without need of further characterization that there was a predominance of the chemical mechanism. The addition of reducing agent allows a controlled reduction in absolute terms, but also in relative terms compared to the oxidation degree of the starting material, making easier the achievement of reproducible results and materials, even extending the process on an industrial scale.

The aerogels obtained with the different production methods were morphologically different but chemically grossly similar. The conventional hydrothermal process resulted in a more homogenous morphology characterized by micropores and a very high specific surface area, which was halved in the material obtained by microwave-assisted hydrothermal treatment, distinguished by a more coarse and irregular structure with the absence of microporosity, due to the rapid bulk heating without a preferential direction that induced a chaotic motion in the dispersion. The chemical characterizations showed that the obtained aerogels were characterized by a close extent of removal of oxygen-containing functional groups, resulting in a change of hybridization from the oxidized carbon atoms tetragonal sp^3 to the typical aromatic planar sp^2, is comparable between the two synthesis techniques, with a difference in the relative carbon percentage of less than 2%. This means that it is possible speeding up the reaction reducing the required time from 12 hours to 1 hour and still obtaining the same chemical properties, thanks to the deoxygenation controlled by the presence of the reducing agent. Ascorbic acid reactivity is enhanced by the high temperature due to the hydrothermal condition, close to the ascorbic acid melting point, in combination with a more fast, controllable and reliable technique as the microwave heating.

The main drawbacks of the MW-assisted technique are the small batches of material produced every run and the limited pressure attainable mainly related to the specific reactor used, because the single-mode reactor is intended to be used mainly for small-scale synthesis for research purpose, while there are bigger devices purposely designed for MW-assisted hydrothermal synthesis, also at higher pressures and temperatures thanks to the use of Teflon autoclaves.

However, the two materials showed widely different electrochemical properties, but realistically it could not be imputed neither to the morphological difference, removed by the grinding and pressing of the material, which destroyed the porosity, or the relatively small chemical difference. The main responsible for the different performances was the excessive thickness of the membranes introduced as protective layer, which effectively suppressed the dendrites but introduced limitation on the performances due to the irregularly increasing internal voltage gap. The thickness of the introduced membrane is excessive both in terms of lithium diffusion and macroscopic properties, because induce an excessive internal resistance and a physical hindrance on the closing of the coin cell, because constitute around the 6% of the total coin cell thickness.

The encouraging results obtained during the research and outlined in this thesis pave the way for a wide number of possibilities for further investigations to go deeper in the knowledge of the mechanisms underlying the self-assembly of RGO aerogels and to improve and refine the facile fabrication of the membranes.

A more systematic study should be performed to evaluate the effect of all the variables and the parameters in the process. Starting from the oxidation of highly ordered pyrolytic graphite (HOPG) with different methods and oxidations degree, should be study the effect of different GO and vitamin C concentrations in the mixture, the impact of different temperatures, reaction times, heating rates and stirring speed on the obtained materials chemistry and morphology, in addition to the evaluation of the effective necessity of attaining the self–assembly. Furthermore, a comparison between the characteristics and electrochemical behavior of only hydrothermally reduced GO, chemically reduced GO with ascorbic acid and the combination of both mechanisms can be done to define which treatment is the most suitable to provide the best performances to the system. Another interesting analysis would be the introduction of heteroatoms and transition metal oxides and halides in the material obtained by means of vitamin C mediated reduction of precursors

The assembly mechanism and the reaction evolution are only indirectly proposed in literature, studying the differences between the starting and the resulting materials. An *in-situ* monitoring of the evolving hydrothermal reaction taking place in a transparent vessel would lead to a better understanding of the reduction reaction. The camera integrated in the MW reactor can be replaced by a micro-raman microscope, an UV-visible spectroscope or a mid-IR spectroscope to follow the evolution in the reaction vessel during the reaction occurrence, to follow up in real-time changes in bondings, microstructure and functional groups concentration. The peculiar design of the reactor also allows to introduce a gas collecting system to analyze the produced gaseous species during the whole reaction through a gs chromatography or a mass spectroscopy of the species. These *in-situ* and real-time characterizations, together with the possibility of a fine and immediate control in the system parameters, would highly contribute to the determination of the reaction pathway, mechanism and kinetic with an immediate access to all the required quantitative and qualitative informations, without the need of interrupting the process to analyze the evolving sample, guaranteeing the absence of any change related to the quenching.

To reduce the electrochemical instability the thickness of the membranes should be reduced, or at least one of these membranes should be tested as separator, maybe inserting inside a common commercial separator as Celgard or Toray with on both sides pressed powder. The membranes, after pressing, could be introduced in a calender system, to get a thinner and uniform thickness and a flat and regular surface, to avoid any effect related to the irregularity.

Another important result would be the development of a binder free method to produce the protective layer exploiting the obtained fine structure, such as a precipitation of sonicated RGO powder on a carbon paper as substrate.

The membrane was introduced on the anode after melting of the lithium to promote the adhesion, so the opening of the cell after cycling would allow the study of the interaction between membrane and lithium. An energy dispersive spectroscopy and a SEM imaging on the surface and cross section of the membranes is useful to study an eventual reaction between Teflon or RGO and lithium and to analyzed how the lithium has evolved under and inside the protective layer, and if the RGO has acted as host material. It could also be accomplished a comparison between the membrane placed on non-melted lithium, infused metal lithium and electrodeposited lithium to see which method is the most suited for a protective layer produced in this specific way.

The last step in the chomprehensive study, after the definition of most suitable chemical and physical properties of the material and the appropriate design of the membrane fabrication and implementation process, would be the testing of the layer in a full working cell against conventional Li-ion batteries cathodes, such as LFP, LCO or LTO, or in a Li-air battery and in a Li-S battery, with the advantage of using a material produced in the same way for the air electrode, the sulfur retaining electrode and the anode protective layer, using the same equipment and only modifying the reagents concentrations.

Bibliography

Adelhelm, P. et al., 2015. From lithium to sodium: Cell chemistry of room temperature sodium-air and sodium-sulfur batteries. *Beilstein Journal of Nanotechnology*, 6(1), pp.1016–1055.

Aetukuri, N.B. et al., 2015. Flexible Ion-Conducting Composite Membranes for Lithium Batteries. *Advanced Energy Materials*, 5(14), pp.1500265–1500271.

Akiya, N. & Savage, P.E., 2002. Roles of water for chemical reactions in high-temperature water. *Chemical Reviews*, 102(8), pp.2725–2750.

Alam, S., et al., 2016. Synthesis of graphene. *International Nano Letters*, 6(2), pp.65–83.

Arakawa, M. et al., 1993. Lithium electrode cycleability and morphology dependence on current density. *Journal of Power Sources*, 43(1), pp.27–35.

Araujo, P.T., et al., 2012. Defects and impurities in graphene-like materials. *Materials Today*, 15(3), pp.98–109.

Aurbach, D. et al., 2002. A short review of failure mechanisms of lithium metal and lithiated graphite anodes in liquid electrolyte solutions. *Solid State Ionics*, 148(3–4), pp.405–416.

Aurbach, D. et al., 2016. Advances in understanding mechanisms underpinning lithium–air batteries. *Nature Energy*, 1(9), p.16128.

Bagri, A. et al., 2010. Structural evolution during the reduction of chemically derived graphene oxide. *Nature Chemistry*, 2(7), pp.581–587.

Barai, A. et al., 2015. A study on the impact of lithium-ion cell relaxation on electrochemical impedance spectroscopy. *Journal of Power Sources*, 280, pp.74–80

Bieker, G., et al., 2015. Electrochemical in situ investigations of SEI and dendrite formation on the lithium metal anode. *Physical Chemistry Chemical Physics*, 17(14), pp.8670–8679.

Bowman, M.D., et al., 2008. Watching microwave-promoted chemistry: reaction monitoring using a digital camera interfaced with a scientific microwave apparatus. *Tetrahedron Letters*, 49(1), pp.195–198.

Bruce, P.G. et al., 2011. Li–O_2 and Li–S batteries with high energy storage. *Nature Materials*, 11(2), pp.172–182.

Brunner, G., 2009. Near critical and supercritical water. Part I. Hydrolytic and hydrothermal processes. *Journal of Supercritical Fluids*, 47(3), pp.373–381.

Cao W., 2012, *The Development and Application of Microwave Heating*, InTech, Rijeka, Croatia

Casiraghi, C., 2011. Raman intensity of graphene. *Physica Status Solidi (B) Basic Research*, 248(11), pp.2593–2597.

Chabot, V. et al., 2014. A review of graphene and graphene oxide sponge: material synthesis and applications to energy and the environment. *Energy & Environmental Science*, 7(5), p.1564.

Chang, B.Y.S. et al., 2012. Facile hydrothermal preparation of titanium dioxide decorated reduced graphene oxide nanocomposite. *International Journal of Nanomedicine*, 7(June), pp.3379–3387.

Chen, K.-H. et al., 2017. Dead lithium: mass transport effects on voltage, capacity, and failure of lithium metal anodes. *Journal of Materials Chemistry A*, 5(23), pp.11671–11681.

Chen, W., et al., 2010. Preparation of graphene by the rapid and mild thermal reduction of graphene oxide induced by microwaves. *Carbon*, 48(4), pp.1146–1152.

Cheng, X. et al., 2015. Dual-Phase Lithium Metal Anode Containing a Polysulfide-Induced Solid Electrolyte Interphase and Nanostructured Graphene Framework for Lithium À Sulfur Batteries. *ACS Nano*, 9(6), pp.6373–6382.

Cheng, X.B. et al., 2015. A review of solid electrolyte interphases on lithium metal anode. *Advanced Science*, 3(3), pp.1–20.

Cheng, Y. et al., 2017. Enhanced mechanical, thermal, and electric properties of graphene aerogels via supercritical ethanol drying and high-Temperature thermal reduction. *Scientific Reports*, 7(1), pp.1–11.

Choi, B.G. et al., 2010. Microwave-assisted synthesis of highly water-soluble graphene towards electrical DNA sensor. *Nanoscale*, 2(12), p.2692.

Claus D. & Besenhard J. O., 2011, *Handbook of Battery Materials – Second Edition*, Wiley-VCH Verlag & Co. KGaA, Weinheim, Germany

Cohen, Y.S., et al., 2000. Micromorphological Studies of Lithium Electrodes in Alkyl Carbonate Solutions Using in Situ Atomic Force Microscopy. *Journal of Physical Chemistry B*, 104(51), pp.12282–12291.

Dai, L. et al., 2015. Metal-Free Catalysts for Oxygen Reduction Reaction. *Chemical Reviews*, 115(11), pp.4823–4892.

De Vries, H. al., 2015. Increasing the cycle life of lithium ion cells by partial state of charge cycling. *Microelectronics Reliability*, 55(11), pp.2247–2253.

Dimiev, A.M., Alemany, L.B. & Tour, J.M., 2012. Graphene Oxide. Origin of Acidity, Its Instability in Water, and a New Dynamic Structural Model. *ACS Nano*, 7(1), pp.576–588.

Ding, F. et al., 2013. Dendrite-Free Lithium Deposition via Self-Healing Electrostatic Shield Mechanism. *Journal of the American Chemical Society*, 135(11), pp.4450–4456.

Dong, Y. et al., 2017. Graphene: a promising 2D material for electrochemical energy storage. *Science Bulletin*, 62(10), pp.724–740.

Dresselhaus, M.S. et al., 2010. Defect characterization in graphene and carbon nanotubes using Raman spectroscopy. *Philosophical Transactions of the Royal Society A: Mathematical, Physical and Engineering Sciences*, 368(1932), pp.5355–5377.

Dreyer, D.R. et al., 2009. The chemistry of graphene oxide. *Chemical Society Reviews*, 39(1), pp.228–240.

Dreyer, D.R., et al., 2014. Harnessing the chemistry of graphene oxide. *Chemical Society Reviews*, 43(15), pp.5288–5292.

Dua, V. et al., 2010. All-organic vapor sensor using inkjet-printed reduced graphene oxide. *Angewandte Chemie - International Edition*, 49(12), pp.2154–2157.

El-Kady, M.F. et al., 2012. Laser scribing of high-performance and flexible graphene-based electrochemical capacitors. *Science*, 335(6074), pp.1326–1330.

Fernández-Merino, M.J. et al., 2010. Vitamin C is an ideal substitute for hydrazine in the reduction of graphene oxide suspensions. *Journal of Physical Chemistry C*, 114(14), pp.6426–6432.

Fu, C. et al., 2013. Evaluation and Characterization of Reduced Graphene Oxide Nanosheets as Anode Materials for Lithium-Ion Batteries. *International Journal of Electrochemical Science*, 8, pp.6269–6280.

Ganguly, A. et al., 2011. Probing the Thermal Deoxygenation of Graphene Oxide using High Resolution In Situ X-Ray based Spectroscopies. *The Journal of Physical Chemistry*, pp.17009–17019.

Gao, W. et al., 2009. New insights into the structure and reduction of graphite oxide. *Nature Chemistry*, 1(5), pp.403–408.

Giardi, R. et al., 2015. One-pot synthesis of graphene-molybdenum oxide hybrids and their application to supercapacitor electrodes. *Applied Materials Today*, 1(1), pp.27–32.

Gigot, A. et al., 2016. Mixed 1T-2H Phase MoS2/Reduced Graphene Oxide as Active Electrode for Enhanced Supercapacitive Performance. *ACS Applied Materials and Interfaces*, 8(48), pp.32842–32852.

Gigot, A., 2018, Graphene-based Supercapacitors, Ph.D. Thesis, Politecnico di Torino

Goldstein, A.P. et al., 2014. Simultaneous sheet cross-linking and deoxygenation in the graphene oxide sol-gel transition. *Journal of Physical Chemistry C*, 118(49), pp.28855–28860.

Grande, L. et al., 2015. The lithium/air battery: Still an emerging system or a practical reality? *Advanced Materials*, 27(5), pp.784–800.

Han, S. et al., 2014. Porous graphene materials for advanced electrochemical energy storage and conversion devices. *Advanced Materials*, 26(6), pp.849–864.

Hassoun, J. & Scrosati, B., 2010. A high-performance polymer tin sulfur lithium ion battery. *Angewandte Chemie - International Edition*, 49(13), pp.2371–2374.

Hassoun, J. et al., 2012. A metal-free, lithium-ion oxygen battery: A step forward to safety in lithium-air batteries. *Nano Letters*, 12(11), pp.5775–5779.

Hu, C. & Dai, L., 2016. Carbon-Based Metal-Free Catalysts for Electrocatalysis beyond the ORR. *Angewandte Chemie - International Edition*, 55(39), pp.11736–11758.

Hu, H. et al., 2012. The role of microwave absorption on formation of graphene from graphite oxide. *Carbon*, 50(9), pp.3267–3273.

Hu, H. et al., 2013. Ultralight and Highly Compressible Graphene Aerogels. *Advanced Materials*, 25(15), pp.2219–2223.

Hu, K. et al., 2016. Understanding Hydrothermally Reduced Graphene Oxide Hydrogels: From Reaction Products to Hydrogel Properties. *Chemistry of Materials*, 28(6), pp.1756–1768.

Jeong, H.K. et al., 2008. Evidence of graphitic AB stacking order of graphite oxides. *Journal of the American Chemical Society*, 130(4), pp.1362–1366.

Ji, C.C. et al., 2013. Self-assembly of three-dimensional interconnected graphene-based aerogels and its application in supercapacitors. *Journal of Colloid and Interface Science*, 407, pp.416–424.

Ji, X., et al., 2009. A highly ordered nanostructured carbon-sulphur cathode for lithium-sulphur batteries. *Nature Materials*, 8(6), pp.500–506.

Jiang, L. & Fan, Z., 2014. Design of advanced porous graphene materials: from graphene nanomesh to 3D architectures. *Nanoscale*, 6(4), pp.1922–1945.

Kaniyoor, A. & Ramaprabhu, S., 2012. A Raman spectroscopic investigation of graphite oxide derived graphene. *AIP Advances*, 2(3).

Kappe O., Dallinger D. and Murphree S., 2009, *Practical Microwave Synthesis for Organic Chemists – Strategies, Instruments, and Protocols*, Wiley-VCH Verlag GmbH & Co. KGaA, Weinheim, Germany

Kudin, K.N. et al., 2007. Raman Spectra of Graphite Oxide and Functionalized Graphene Sheets. *Nano Letters*, 8(1), pp.36–41.

Lang, J. et al., 2017. High performance lithium metal anode: Progress and prospects. *Energy Storage Materials*, 7(12), pp.115–129.

Li, J.L. et al., 2014. MoS_2-reduced graphene oxide composites synthesized via a microwave-assisted method for visible-light photocatalytic degradation of methylene blue. *Rsc Advances*, 4(19), pp.9647–9651.

Li, L. et al., 2012. Rapid microwave-assisted synthesis of Mn_3O_4–graphene nanocomposite and its lithium storage properties. *Journal of Materials Chemistry*, 22(8), p.3600.

Li, Y. et al., 2016. Recent Advances in Non-Aqueous Electrolyte for Rechargeable Li–O_2 Batteries. *Advanced Energy Materials*, 6(18), pp.1–26.

Liang, Z. et al., 2016. Composite lithium metal anode by melt infusion of lithium into a 3D conducting scaffold with lithiophilic coating. *Proceedings of the National Academy of Sciences*, 113(11), pp.2862–2867.

Lin, D. et al., 2016. Layered reduced graphene oxide with nanoscale interlayer gaps as a stable host for lithium metal anodes. *Nature Nanotechnology*, 11(7), pp.626–632.

Lin, D., et al., 2017. Reviving the lithium metal anode for high-energy batteries. *Nature Nanotechnology*, 12(3), pp.194–206.

Liu, C.-L. et al., 2012. Microwave-assisted hydrothermal synthesis of Mn_3O_4/reduced graphene oxide composites for high power supercapacitors. *Journal of Power Sources*, 217, pp.184–192.

Liu, F. et al., 2012. Folded structured graphene paper for high performance electrode materials. *Advanced Materials*, 24(8), pp.1089–1094.

Liu, Y. et al., 2016. Lithium-coated polymeric matrix as a minimum volume-change and dendrite-free lithium metal anode. *Nature Communications*, 7, p.10992.

Long, J., et al., 2011. Microwave-assisted rapid synthesis of water-soluble graphene. *Journal of Materials Chemistry*, 21(28), p.10421.

Lv, T. et al., 2011. Enhanced photocatalytic degradation of methylene blue by ZnO-reduced graphene oxide composite synthesized via microwave-assisted reaction. *Journal of Alloys and Compounds*, 509(41), pp.10086–10091.

Lv, W. et al., 2016. Graphene-based materials for electrochemical energy storage devices: Opportunities and challenges. *Energy Storage Materials*, 2, pp.107–138.

Mahmood, N. et al., 2014. Graphene-based nanocomposites for energy storage and conversion in lithium batteries, supercapacitors and fuel cells. *Journal of Materials Chemistry A*, 2(1), pp.15–32.

Manthiram, A. et al., 2015. Lithium-Sulfur Batteries: Progress and Prospects. *Advanced Materials*, 27(12), pp.1980–2006.

Mao, S., et al., 2015. Three-dimensional graphene-based composites for energy applications. *Nanoscale*, 7(16), pp.6924–6943.

Marcano, D.C. et al., 2010. Improved Synthesis of Graphene Oxide. *ACS Nano*, 4(8), pp.4806–4814.

Mistry, A., Smith, K. & Mukherjee, P.P., 2017. Secondary Phase Stochastics in Lithium-ion Battery Electrodes. *ACS Applied Materials & Interfaces*, 10(7), pp.6317–6326.

Monroe, C. & Newman, J., 2003. Dendrite Growth in Lithium/Polymer Systems. *Journal of The Electrochemical Society*, 150(10), p.A1377–A1384

Monroe, C. & Newman, J., 2004. The Effect of Interfacial Deformation on Electrodeposition Kinetics. *Journal of The Electrochemical Society*, 151(6), pp.880–886.

Monroe, C. & Newman, J., 2005. The Impact of Elastic Deformation on Deposition Kinetics at Lithium/Polymer Interfaces. *Journal of the Electrochemical Society*, 152(2), pp.A396–A404.

Mukherjee, R. et al., 2014. Defect-induced plating of lithium metal within porous graphene networks. *Nature Communications*, 5(3710), pp.1–10.

Mungse, H.P. et al., 2014. Hydrothermal deoxygenation of graphene oxide in sub- and supercritical water. *RSC Advances*, 4(43), p.22589.

Murugan, A.V., et al., 2010. Rapid, facile microwave-solvothermal synthesis of graphene nanosheets and their polyaniline nanocomposites for energy storage. *Chemistry of Materials*, 22(8), p.2692.

Niu, Z. et al., 2012. A leavening strategy to prepare reduced graphene oxide foams. *Advanced Materials*, 24(30), pp.4144–4150.

Odziemkowski, M. & Irish, D.E., 1993. An Electrochemical Study of the Reactivity at the Lithium Electrolyte / Bare Lithium Metal Interface. *Journal of The Electrochemical Society*, 140(6), pp.1546–1555.

Orsini, F. et al., 1998. In situ Scanning Electron Microscopy (SEM) observation of interfaces within plastic lithium batteries. *Journal of Power Sources*, 76(1), pp.19–29.

Padbury, R. & Zhang, X., 2011. Lithium–oxygen batteries—Limiting factors that affect performance. *Journal of Power Sources*, 196(10), pp.4436–4444

Paredes, J.I., et al., 2008. Graphene Oxide Dispersions in Organic Solvents. *Langmuir*, 24(19), pp.10560–10564.

Park, S. et al., 2009. Reduced Graphene Oxide in a Wide Variety of Organic Solvents. *Nano Letters*, 9(4), pp.1593–1597.

Park, S.-H. et al., 2011. Solid-state microwave irradiation synthesis of high quality graphene nanosheets under hydrogen containing atmosphere. *Journal of Materials Chemistry*, 21(3), pp.680–686.

Peled, E., 1979. The Electrochemical Behavior of Alkali and Alkaline Earth Metals in Nonaqueous Battery Systems- The Solid Electrolyte Interphase Model. *Journal of The Electrochemical Society*, 126(12), pp.2047–2051.

Peled, E., 1997. Advanced Model for Solid Electrolyte Interphase Electrodes in Liquid and Polymer Electrolytes. *Journal of The Electrochemical Society*, 144(8), pp.L208–L210.

Pimenta, M.A. et al., 2007. Studying disorder in graphite-based systems by Raman spectroscopy. *Phys. Chem. Chem. Phys.*, 9(11), pp.1276–1290.

Qin, W. et al., 2015. MoS_2-reduced graphene oxide composites via microwave assisted synthesis for sodium ion battery anode with improved capacity and cycling performance. *Electrochimica Acta*, 153, pp.55–61.

Reddy T. B. & Linden D., 2014, *Linden's Handbook of Batteries – Fourth Edition*, The McGraw-Hill Companies, Inc., New York, US

Seh, Z.W. et al., 2013. Sulphur-TiO 2 yolk-shell nanoarchitecture with internal void space for long-cycle lithium-sulphur batteries. *Nature Communications*, 4.

Shao, Y. et al., 2010. Facile and controllable electrochemical reduction of graphene oxide and its applications. *Journal of Materials Chemistry*, 20(4), pp.743–748.

Shao, Y. et al., 2013. Making Li-air batteries rechargeable: Material challenges. *Advanced Functional Materials*, 23(8), pp.987–1004.

Shen, J. et al., 2011. One step hydrothermal synthesis of TiO_2-reduced graphene oxide sheets. *Journal of Materials Chemistry*, 21(10), p.3415.

Shi, G. & Zhang, L., 2011. Preparation of Highly Conductive Graphene Hydrogels for Fabricating Supercapacitors with High Rate Capability Preparation of Highly Conductive Graphene Hydrogels for Fabricating Supercapacitors with High Rate Capability. *Journal of Physical Chemistry C*, 115(34), pp.17206–17212.

Shin, W.K., et al., 2015. Effective Suppression of Dendritic Lithium Growth Using an Ultrathin Coating of Nitrogen and Sulfur Codoped Graphene Nanosheets on Polymer Separator for Lithium Metal Batteries. *ACS Applied Materials and Interfaces*, 7(42), pp.23700–23707.

Song, M.K. et al., 2011. Nanostructured electrodes for lithium-ion and lithium-air batteries: The latest developments, challenges, and perspectives. *Materials Science and Engineering R: Reports*, 72(11), pp.203–252.

Stankovich, S. et al., 2007. Synthesis of graphene-based nanosheets via chemical reduction of exfoliated graphite oxide. *Carbon*, 45(7), pp.1558–1565.

Sui, Z. et al., 2012. Green synthesis of carbon nanotube–graphene hybrid aerogels and their use as versatile agents for water purification. *Journal of Materials Chemistry*, 22(V), pp.8767–8771.

Tang, Z. et al., 2010. Noble-metal-promoted three-dimensional macroassembly of single-layered graphene oxide. *Angewandte Chemie - International Edition*, 49(27), pp.4603–4607.

Thomas, H.R. et al., 2013. Deoxygenation of graphene oxide: Reduction or cleaning? *Chemistry of Materials*, 25(18), pp.3580–3588.

Ţucureanu, V., et al., 2016. FTIR Spectroscopy for Carbon Family Study. *Critical Reviews in Analytical Chemistry*, 46(6), pp.502–520.

Vermisoglou, E.C. et al., 2015. Non-activated high surface area expanded graphite oxide for supercapacitors. *Applied Surface Science*, 358, pp.110–121.

Wakeland, S. et al., 2010. Production of graphene from graphite oxide using urea as expansion-reduction agent. *Carbon*, 48(12), pp.3463–3470.

Wang, B. & Guo, Y., 2010. Synthesis of CuO / graphene nanocomposite as a high-performance anode material for lithium- ion batteries. *Journal of Materials Chemistry*, 20(11), pp.10661–10664.

Wang, J., et al., 2013. Challenges and opportunities of nanostructured materials for aprotic rechargeable lithium-air batteries. *Nano Energy*, 2(4), pp.443–467.

Wang, Y. et al., 2014. Microwave-assisted hydrothermal synthesis of graphene based Au–TiO_2 photocatalysts for efficient visible-light hydrogen production. *Journal of Materials Chemistry A*, 2(11), pp.3847–3855.

Wang, Z.-L. et al., 2013. Oxygen electrocatalysts in metal-air batteries: from aqueous to nonaqueous electrolytes. *Chemical Society reviews*, 43, p. 7746-7786 .

Wang, Z.L. et al., 2012. Graphene oxide gel-derived, free-standing, hierarchically porous carbon for high-capacity and high-rate rechargeable Li-O_2 batteries. *Advanced Functional Materials*, 22(17), pp.3699–3705.

Wild, M. et al., 2015. Lithium sulfur batteries, a mechanistic review. *Energy Environmental Science*, 8(12), pp.3477–3494.

Williford, R.E. & Zhang, J.G., 2009. Air electrode design for sustained high power operation of Li/air batteries. *Journal of Power Sources*, 194(2), pp.1164–1170.

Wu, S., et al., 2016. Removal of mercury and fluoride from aqueous solutions by three-dimensional reduced-graphene oxide aerogel. *Research on Chemical Intermediates*, 42(5), pp.4513–4530.

Xiang, Q. et al., 2011. Enhanced photocatalytic H_2-production activity of graphene-modified titania nanosheets. *Nanoscale*, 3(9), p.3670.

Xiao, J. et al., 2011. Hierarchically porous graphene as a lithium-air battery electrode. *Nano Letters*, 11(11), pp.5071–5078.

Xin, S. et al., 2017. Progress of rechargeable lithium metal batteries based on conversion reactions. *National Science Review*, 4(1), pp.54–70.

Xu R., Pang W., Huo Q., 2011, *Modern Inorganic Synthetic Chemistry*, Elsevier B.V., Amsterdam, The Netherlands

Xu, C. et al., 2015. Sulfur/three-dimensional graphene composite for high performance lithium-sulfur batteries. *Journal of Power Sources*, 275, pp.22–25.

Xu, K., 2014. Electrolytes and Interphases in Li-Ion Batteries and Beyond. *Chemical Reviews*, 114(23), pp.11503–11618.

Xu, W. et al., 2014. Lithium metal anodes for rechargeable batteries. *Energy Environmental Science*, 7(2), pp.513–537.

Xu, Y. et al., 2010. Self-assembled Graphene Hydrogel via a One-Step Hydrothermal Process. *ACS nano*, 4(7), pp.4324–4330.

Yan, K. et al., 2014. Ultrathin Two-Dimensional Atomic Crystals as Stable Interfacial Layer for Improvement of Lithium Metal Anode. *Nano Letters*, 14(10), pp.6016–6022.

Yang, J. et al., 2014. Rapid and controllable synthesis of nitrogen doped reduced graphene oxide using microwave-assisted hydrothermal reaction for high power-density supercapacitors. *Carbon*, 73, pp.106–113.

Yao, Q. et al., 2017. 3D assembly based on 2D structure of Cellulose Nanofibril/Graphene Oxide Hybrid Aerogel for Adsorptive Removal of Antibiotics in Water. *Scientific Reports*, 7(December 2016), pp.1–13.

Yin, Y.X. et al., 2013. Lithium-sulfur batteries: Electrochemistry, materials, and prospects. *Angewandte Chemie - International Edition*, 52(50), pp.13186–13200.

Yoshimatsu, I., 1988. Lithium Electrode Morphology during Cycling in Lithium Cells. *Journal of The Electrochemical Society*, 135(10), p.2422.

Yu, M. et al., 2015. Graphene materials for lithium – sulfur batteries. *Energy Storage Materials*, 1, pp.51–73.

Zandiatashbar, A. et al., 2014. Effect of defects on the intrinsic strength and stiffness of graphene. *Nature Communications*, 5(3186), pp.1–9.

Zhan, D. et al., 2011. Electronic structure of graphite oxide and thermally reduced graphite oxide. *Carbon*, 49(4), pp.1362–1366.

Zhang, C. et al., 2017. Carbon enables the practical use of lithium metal in a battery. *Carbon*, 123, pp.744–755.

Zhang, J. et al., 2010. Reduction of graphene oxide via L-ascorbic acid. *Chem. Commun.*, 46(7), pp.1112–1114.

Zhang, K. et al., 2016. Recent Developments of the Lithium Metal Anode for Rechargeable Non-Aqueous Batteries. *Advanced Energy Materials*, 6(20), pp.1600811–1600825.

Zhang, R. et al., 2017. Lithiophilic Sites in Doped Graphene Guide Uniform Lithium Nucleation for Dendrite-Free Lithium Metal Anodes. *Angewandte Chemie - International Edition*, 56(27), pp.7764–7768.

Zhang, X. et al., 2011. Mechanically strong and highly conductive graphene aerogel and its use as electrodes for electrochemical power sources. *Journal of Materials Chemistry*, 21(18), pp.6494–6497.

Zhao, J. et al., 2017. Air-stable and freestanding lithium alloy/graphene foil as an alternative to lithium metal anodes. *Nature Nanotechnology*, (7), pp.1–8.

Zhao, Y. et al., 2012. A versatile, ultralight, nitrogen-doped graphene framework. *Angewandte Chemie - International Edition*, 51(45), pp.11371–11375.

Zheng, G. et al., 2013. Amphiphilic Surface Modification of Hollow Carbon Nano fibers for Improved Cycle Life of Lithium Sulfur Batteries. *Nano Letters*, 13(3), pp.1265–1270.

Zheng, G. et al., 2014. Interconnected hollow carbon nanospheres for stable lithium metal anodes. *Nature Nanotechnology*, 9(8), pp.618–623.

Zheng, J.P. et al., 2011. The Theoretical Energy Densities of Dual-Electrolytes Rechargeable Li-Air and Li-Air Flow Batteries. *Journal of The Electrochemical Society*, 158(1), p.A43.

Zhou, G. et al., 2016. High-performance lithium-sulfur batteries with a self-supported, 3D Li2S-doped graphene aerogel cathodes. *Advanced Energy Materials*, 6(2), pp.1–9.

Zhou, Y. et al., 2009. Hydrothermal dehydration for the “green” reduction of exfoliated graphene oxide to graphene and demonstration of tunable optical limiting properties. *Chemistry of Materials*, 21(13), pp.2950–2956.

Zhu, C. et al., 2010. Reducing sugar: New functional molecules for the green synthesis of graphene nanosheets. *ACS Nano*, 4(4), pp.2429–2437.

Zhu, Z. et al., 2016. Anion-redox nanolithia cathodes for Li-ion batteries. *Nature Energy*, 1(8), pp.16111–16118.

Zong, M. et al., 2014. One-pot hydrothermal synthesis of RGO/$CoFe_2O_4$ composite and its excellent microwave absorption properties. *Materials Letters*, 114, pp.52–55

Zoski C. G., 2007, *Handbook of Electrochemistry*, Elsevier B.V., Amsterdam, The Netherlands